Numerical and Experimental Fuel Flow Analysis of Small Engine Carburetor Idle Circuits

by

Terry L. Hendricks

A thesis submitted in partial fulfillment of
the requirements for the degree of

Master of Science
(Mechanical Engineering)

at the

UNIVERSITY OF WISCONSIN-MADISON

2007

Abstract

Small engine carburetors have been used for over 100 years and their continual development has produced a mechanical device that although simple in principle is difficult to control in practice. This study aims to develop a mathematical model of the air and fuel delivery process that occurs in the idle path that can predict the air-to-fuel ratio in small engines.

A one-dimensional model was created that incorporates single phase air and fuel flow effects using an electrical circuit analog. The model incorporates dynamic fuel flow effects due to inertia, and was coupled to the engine airflow via input data provided by commercial engine simulation software. The methodology developed for the idle path creates a foundation on which to build a transition system and the boundary conditions that control it. A simplified model of the main path circuit was also created that incorporates single phase inertial effects and was used to provide boundary conditions to the idle path model. Finally, a dynamic sensitivity analysis of the idle path was conducted to analyze which elements of the idle path control the fuel flow response.

The second part of this study addressed the results of the sensitivity analysis. The idle discharge metering orifice has the largest effect on the air-to-fuel ratio delivered to the engine by the idle path. An experiment was created to characterize two-phase orifices representative of the idle discharge metering orifice. The data produces an empirical correlation that can be used to predict the pressure loss across the metering orifice. The correlation displays results that are inconsistent with the homogeneous assumption and highlights the need for further research in this area.

Acknowledgements

First, a special thanks goes out to Andrea Toldt for her understanding, patience, and care throughout this time consuming and difficult process. She is the definition of true love, and her unending encouragement and faith in my abilities have allowed me to pursue and accomplish the most challenging of tasks. I appreciate everything she has done for me, and without her my life would be empty indeed.

I would also like to thank Professor Tim Shedd for his help and advice during the more difficult phases of this project. His advice on research and on life has been invaluable. A special thanks also goes out to Professors Greg Nellis and Jaal Ghandhi for their assistance in the numerical model and the experimental design, respectively.

The decision to pursue a graduate education could not have been made without the eternal support of my family. My parents, Tony and Cindy, deserve a very special thanks for their continual support. I know their dream is to see each one of their children go further in life than they could have thought possible, and to that end, I hope I have made them proud. I would also like to thank my brother and sister, Troy and Natalie, for their support during this process. Finally, special thanks goes to Kurt Roblek for all of the countless discussions on life and the pursuit of happiness.

Last, but certainly not least, I want to thank all of my friends in the Engine Research Center and the Solar Energy Laboratory. You have made my time here fun and enjoyable. Without you, I never would have made it.

This work was funded by the Wisconsin Small Engine Consortium.

Table of Contents

Abstract i

Table of Contents iii

List of Tables vi

List of Figures vii

Nomenclature xii

1. Introduction 1

1.1 Emissions..... 1
1.2 Air-to-Fuel Ratio Control and Design..... 4
1.3 Research Objectives..... 7
1.4 Outline..... 7

2. Literature Review 9

2.1 Engine Airflow Process Description..... 9
2.1.1 Air Filter/ Inlet System Losses..... 10
2.1.2 Venturi Flow Losses..... 11
2.1.3 Pressure Losses at the Throttle Plate/ Blade..... 13
2.1.4 Intake Runner Pressure Losses..... 18
2.2 Unsteady Gas Flow Effects in the Intake System..... 21
2.2.1 Volumetric Efficiency..... 22
2.2.2 Ram Effect..... 22
2.2.3 Wave Tuning..... 24
2.3 Airflow Modeling Techniques..... 26
2.3.1 The Quasi-Steady Method..... 27
2.3.2 The Filling and Emptying Method..... 29
2.3.3 Finite Element Method or Wave Action Method (WAVE)..... 30
2.4 Carburetor Fuel Flow Process Description..... 32
2.4.1 High Speed Operation of the Main Path System..... 33
2.4.2 Low Speed Operation of the Idle Path..... 36
2.4.3 Transition from Low Speed to High Speed Operation..... 38
2.5 Fuel Flow Models..... 40
2.5.1 Steady State Models..... 40
2.5.2 Pulsation Effects during Actual Carburetor Operation..... 45
2.5.3 Quasi-Steady State Fuel Flow Models..... 48

2.5.4 Unsteady Fuel Flow Models..... 49
2.6 Two-Phase Flow Models in Tubes and Orifices..... 53
2.6.1 Two-Phase Flow in Tubes..... 53
2.6.2 Two-Phase Flow through Metering Orifices..... 55
2.7 Multiphase Transport Effects..... 56
2.8 Summary of Literature Review..... 57

3. Carburetor Model 59

3.1 Electrical Analog Description of the Idle Path..... 59
3.2 Idle Path Model Structure..... 63
3.3 Calculation of the Fluid Element Characteristics..... 66
3.3.1 Single Phase Air Section..... 66
3.3.2 Single Phase Fuel Section..... 70
3.3.3 Two-Phase Section..... 72
3.4 Calculation of the State Variable Derivatives..... 75
3.5 Integration of the State Variable over the System Timestep..... 78
3.6 Nominal Results for the Briggs & Stratton Intek Engine..... 80
3.7 Boundary Conditions for Idle and Transition Path Circuit..... 82
3.7.1 Solving for the Pressure at Transition System Discharge Holes. 82
3.7.2 Calculation of the Main Jet Pressure Using a Simplified Main Path Model..... 88
3.8 Parametric Study of the Briggs & Stratton Intek Engine..... 103
3.8.1 Sensitivity Analysis..... 103
3.8.2 Inertial Effects in the Single Phase Fuel Region..... 105
3.8.3 Two-Phase Flow Correlations..... 107
3.8.4 Two-Phase Flow Expansion Loss Models..... 111

4. Characterization of the Expansion Loss at the Two-Phase Idle Discharge Metering Orifice 114

4.1 Experimental Setup..... 114
4.1.1 Description of Mineral Spirits Loop..... 116
4.1.2 Description of Air Flow Loop and Bubble Flow Meter..... 116
4.1.3 Two-Phase Test Section and Exhaust System..... 118
4.2 Data Acquisition..... 121
4.3 Test Pieces and Flow Conditions..... 122
4.4 Experimental Uncertainty Analysis..... 123
4.4.1 Bubble Flow Meter Uncertainty..... 124
4.4.2 Pressure Transducer Uncertainty..... 124
4.4.3 Liquid Flow Rate Uncertainty..... 125
4.4.4 Orifice Plate Diameter Uncertainty..... 126
4.5 Experimental Results..... 128
4.6 Data Correlation and Analysis..... 133
4.7 Correlation Application to Idle Path Model..... 136

5. Conclusions and Recommendations for Future Research 139

5.1 Idle Path Model..... 139
5.1.1 Transition System Fundamentals..... 140
5.1.2 Main Path Model..... 141
5.2 Experimental Characterization of Two-Phase Metering Orifices..... 141
5.3 Recommendations for Future Work..... 142

Appendix A: Idle Path Model 144

A.1 BSI_Geometry.m..... 144
A.2 GtoR.m..... 144
A.3 Stder.m..... 147
A.4 Idlepath.m..... 148
A.5 Runidlepath.m..... 149

Appendix B: Briggs & Stratton Engine Geometry 150

B.1 Nominal Engine Specifications Needed to Run GT-Power..... 150

Appendix C: SIMPLE Main Path Model 151

C.1 Nikki_Geometry.m..... 151
C.2 GtoRmain.m..... 151
C.3 Stder_main.m..... 155
C.4 Mainpath.m..... 157
C.5 Runmainpath.m..... 158
C.6 Reynolds_Fric.m..... 159
C.7 Throttle_Area.m..... 159
C.8 Comp_Press.m..... 160
C.9 Discharge_Coeff.m..... 160

Bibliography 161

List of Tables

2.1 Vortex shedding frequencies for different throttle angles. Reproduced from Alsemgeest et al. [8]..... 15

2.2 Characteristics of the three models typically used to compute the air flow through an engine, from Chung [19]..... 27

3.1 BSI characteristics for carburetor idle path studied..... 63

3.2 Variable definitions for main path model in Figure 3.12..... 90

4.1 Fluids property comparison for Gasoline and Mineral Spirits..... 115

List of Figures

1.1 CO emissions as a percentage of total CO emissions as a function of year; industrial, on-road, non-road, and miscellaneous sources not including power generation sources are included. Taken from US National Emissions Index [3]..... 2

1.2 CO emissions as a percentage of total CO emissions since 1970 for lawn and garden equipment..... 3

1.3 Variation of HC, CO, and NOx concentration in the exhaust of a conventional spark-ignition engine with varying *AFR* at constant engine speed [5]..... 5

1.4 Normalized power produced as a function of *AFR* for a generic engine at a given operating condition..... 6

2.1 Air intake flow path just after intake valve opening (IVO) with the piston descending from top dead center (TDC). Air pressure falls from stagnation conditions (P_o) to cylinder pressure (P_{cyl}) along the intake path due to various losses..... 10

2.2 Representative Venturi showing inlet obstacles and the fuel tube..... 11

2.3 Results from CFD study by Arias et al showing a.) Static pressure and b.) Mach number..... 12

2.4 Flow separation in the presence of an adverse pressure gradient..... 13

2.5 Velocity vector plot of flow past a throttle plate with a record of *u*, *v*, and *w* velocity components as a function of iteration number, which can be viewed as a time scale. Reproduced from Alsemgeest et al. [8]..... 14

2.6 Air mass flow rate for varying throttle angles as a function of manifold pressure bounded by limits for differing engine speeds. Reproduced from Pursiful et al. [10]..... 16

2.7 Variables in the equation used to find the throttle plate area..... 18

2.8 Pressure loss sources in a generic SI engine intake runner. Adapted from Superflow Flowbench 600 Instruction Manual [15]..... 19

2.9 Flow regimes present in typical inlet valve flow and their effect of discharge coefficients, from Heywood [2.1]..... 20

2.10 Induction inertial ram cylinder charging for a given engine. Adapted from Heisler [17]..... 23

2.11 Volumetric efficiency for a single cylinder engine with varying runner lengths. Created by the author..... 25

2.12 Representative example of the predictive capabilities of WAVE action techniques for predicting pressure profiles in operating engines. Formula 1 intake manifold operating at 13,000 RPM. Taken from [23]..... 31

2.13 Significant features of a modern small engine carburetor..... 33

2.14 Significant features of a typical idle path found in small engine carburetors during low speed operation..... 37

2.15 Transition system typically employed in small engine carburetors during two different throttle conditions..... 38

2.16 Predicted and experimental results for airflow and fuel economy in 289 in^3 engine with a 2-BBL downdraught carburetor. Reproduced from Harrington and Bolt [11]..... 41

2.17 Geometric details used by Shinoda et al. [28] in their transition region metering analysis, and results obtained from steady state analysis over entire operating range..... 42

2.18 (a) Carburetor model under consideration, (b) bypass port cases examined, and (c) forms of bypass port studied. Reproduced from Furuyama [30]..... 44

2.19 Predicted and experimental results gathered by Moss [33]. Pulsation factor is a term used to describe the amplitude of the pressure wave in the intake manifold. Mixture richening factor prescribes the additional amount of fuel delivered in terms of a factor..... 46

2.20 Comparison of fuel flow models implemented by Arias [41]. EES-qss represents the quasi-steady model, EES-dyn defines the results of the dynamic fuel flow model, and Fortran (GT-Power) represents a dynamic model coupled to GT-Power..... 51

2.21 Flow patterns and flow regime map for different conditions. Reproduced from Oya [44,45]..... 54

2.22 Pressure drop predicted by correlation developed versus measured pressure drop. From Arias [41]..... 55

3.1 Idle path geometry of the Briggs & Stratton Intek carburetor..... 60

3.2 Electrical analogy of the current idle path with fluid flows and boundary conditions indicated..... 61

3.3 Alternative idle path configuration displaying a simple transition system.... 62

3.4 Structure of the idle path model..... 64

3.5 Schematic of idle path configuration with intermediate values..... 75

3.6 Venturi, manifold, and fuel well pressures for a Briggs & Stratton Intek Engine carburetor operating at a 3° throttle angle and 1800 [rev/min]. Note choking at the throttle plate occurs around 52000 Pa..... 81

3.7 Fuel and air-bleed flow as a function of crank angle for a Briggs & Stratton Intek Engine carburetor at a 3^{o} throttle angle and 1800 [rev/min]... 82

3.8 Terminology associated with transition system boundary conditions and depiction of current flow directions at pictured throttle angle..... 83

3.9 Throttle flow area as a function of throttle angle for the Briggs & Stratton Intek Engine carburetor..... 85

3.10 Experimentally determined discharge coefficient as a function of throttle angle for a generic throttle plate as taken from Harrington [11]..... 86

3.11 Throttle pressure as a function of crank angle for varying throttle angle, calculated in MatLab with data for air flow rate taken from GT-Power at 1800 [rev/min] with a BSI carburetor..... 87

3.12 Electric analog descriptions of main path from Arias and presented simplified main path circuit..... 89

3.13 Emulsion tube model for main path approximation showing the situation under which air flow does not enter the emulsion tube..... 94

3.14 Emulsion tube model showing one set of holes uncovered..... 96

3.15 Air flow through two sets of emulsion tube holes as represented in the Arias model and in the newly proposed model..... 97

3.16 Model representation when three sets of emulsion tube holes are uncovered 97

3.17 Fuel Flow prediction between the SIMPLE main path model created in MATLAB and the Arias (DYN) model created by Arias [41] in EES..... 99

3.18 Comparison of four different fuel flow models used to predict fuel flow in the main path circuit..... 100

3.19 Predictions of main jet pressure with simple MATLAB main path model and EES model created by Arias for a Nikki carburetor at 900 RPM and WOT conditions..... 102

3.20 The relative sensitivity (ε_k) for each input parameter (k) contained in the `geometry` file shown in Table 3.1 simulated under dynamic conditions. Note that the sensitivity axis is a logarithmic scale..... 104

3.21 The effect of the inertia on the single-phase fuel region. Notice the overall increase in the fuel flow associated with going from the quasi-steady model, labeled (QSS), to the high speed condition..... 106

3.22 Integrated air-to-fuel ratios for Figure 3.21, showing that the A/F ratio is essentially unaffected by the inertia as given by the sensitivity analysis parameters L_{fi} and D_{fi}. There is a negligible fuel-enrichment associated with the inertia in this configuration of the idle path..... 107

3.23 Two-phase flow frictional pressure drop correlations applied to two-phase zone in idle path for L_{tpl}= 0.01 mm. Correlations described by Collier and Thome [59]..... 109

3.24 Fuel flow response variations due to two-phase frictional pressure drop model specified for an artificially long path length, L_{tpl}= 50.0 mm..... 110

3.25 Integrated *AFR* for different two-phase flow correlations implemented in the carburetor idle path..... 111

3.26 Two-phase expansion loss models as implemented in the idle path code. Not shown is the result when the expansion loss coefficient is set equal to zero..... 112

4.1 Schematic of experimental setup for characterization of orifice loss measurement..... 115

4.2 Close-up of components used in air flow measurement. Note the mixing tee and the soap and water container are not depicted in the general loop schematic in Figure 4.1..... 117

4.3 Cross section of modular two-phase test section with flow visualization capabilities used in orifice pressure loss characterization..... 119

4.4 Test data for two-phase flow conditions compared with recorded pressure drop for single phase air flow only..... 129

4.5 Measured pressure drop as a function of liquid flow rate for constant air flow rates with orifice sizes (a) 0.53 mm, (b) 0.92 mm, (c) 1.19 mm, (d) 1.41 mm, and (e) 1.60 mm. Orifice diameter is also identified in the upper right hand corner of each plot..... 130

4.6 Kinetic energy of two-phase mixture for all orifice plates tested as a function of measured pressure drop..... 132

4.7 Plot of measured pressure drop versus pressure drop predicted by homogeneous mixture kinetic energy combined with a form of the Lockhart-Martinelli two-phase multiplier (Δp_{corr})..... 134

4.8 Pressure drop predicted by two-phase correlation versus experimental data for small two-phase metering orifices..... 135

4.9 Comparison of fuel flow rates predicted with experimentally derived correlation and the baseline configuration tested. The throttle angle was set at 5^{o} and the engine speed was simulated at 900 RPM..... 136

4.10 Comparison of implemented correlation with baseline configuration for varying throttle angle. Note combustion quality will degrade significantly for *AFR* over approximately 20; this indicates that the idle path system has effectively turned off..... 137

Nomenclature

Symbols

A	area or coefficient matrix
AFR	integrated air-to-fuel ratio
b	matrix of constants
BDC	bottom dead center
C	constant
C_d	discharge coefficient
CCM	unit equal to cm^3/min
d	throttle shaft diameter
D	diameter
DYN	dynamic model
f	friction factor
g	gravity
h	height or hole
In	inertia
IVC	intake valve closing
k	roughness
K	constant
KE	kinetic energy
l	connecting rod length
L	length or lower half of matrix
m	mass
$\dot{m}$	mass flow
n	number of holes
N	number of substeps in numerical model
P	pressure
QSS	quasi-steady state model
r	crank throw
$read$	reading from sensor
R	resistance of an element or universal gas constant
$Range$	sensor voltage range
RPM	engine speed
SG	specific gravity
$SIMPLE$	proposed simplified main path model
t	time
T	temperature
TDC	top dead center
u	velocity
U	upper half of matrix
v	velocity
V	volume

Volt	voltage
WOT	wide open throttle conditions
x	distance or position
X	matrix of unknown variables
Y	inverted matrix or variable to be minimized

Greek Symbols

α	void fraction
χ	vapor quality
δ	uncertainty
Δp	pressure differential
Δt	timestep
ε	sensitivity
γ	ratio of specific heats
η	efficiency
ρ	density
Φ	compressibility factor
μ	dynamic viscosity
σ	surface tension
θ	throttle angle

Subscripts

a	air
actual	measured quantity
ap	air path
ap,o	air path orifice
aj	after the air-bleed orifice in the main path
bowl	in the float bowl
corr	correlation
cyl	cylinder
d	displacement
dev	developing
engine	of the engine
ent	entrance
et	emulsion tube
f	fuel
fb,b	at the bottom of the float bowl
fi	fuel in the idle path
fm	fuel in the main path
fw	fuel well
h	height
h1	at the first set of emulsion tube holes
h2	at the second set of emulsion tube holes

h3	at the third set of emulsion tube holes
i	index (1,2,3...)
i,1	first fictitious junction in idle path
i,2	second fictitious junction in idle path
in	inlet
KE	kinetic energy
LM	Lockhart-Martinelli parameter
man	manifold
min	mineral spirits
mix	two-phase mixture
mj	after the main jet
o	stagnation conditions or designated starting point
sp	single phase fuel section
st	surface tension
t	throat
th	throttle
tt	correlation parameter
th1	at the nozzle formed by the throttle plate
tp1	first or only two-phase section
tp2	second two-phase section
tp3	third two-phase section
tp,o	two-phase discharge orifice in idle path
tube	emulsion tube
up,v	static conditions upstream of the venturi
vol	volumetric
vt	venturi throat

Mathematical Symbols

$\frac{\partial(\ )}{\partial x}$	partial differential equation with respect to position
$\frac{\partial(\ )}{\partial t}$	partial differential equation with respect to time
$\frac{D(\ )}{Dt}$	total derivative

Chapter 1

Introduction and Research Motivation

Small engines are defined as non-road utility engines with a power rating of less than or equal to 50 horsepower [1]. Small engine sales of approximately 20 million units annually are reported in the United States by the largest manufacturers of small engines [2]. The uses of small engines include, but are not limited, to lawn mowers, generators, leaf blowers, personal watercraft, etc. Small engines can be adapted to a variety of applications and this has led to a tremendous growth in their sales over the past quarter of a century. At the same time, their widespread use has created an ultra-competitive industry that is driven by constraints such as cost, weight, packaging, and fuel-efficiency.

In the small engine industry, concerns related to cost and manufacturing have prevented the widespread integration of the same advanced engine technologies that are currently employed and mandated by the major automobile manufacturers and the Environmental Protection Agency (EPA), respectively. These advanced technologies include electronic fuel injection, catalytic treatment of exhaust gases, turbo charging, etc. These technologies improve performance and/or reduce emissions from on-road automobiles. However, in the small engine industry, the carburetor remains the long term fuel delivery solution due in large part to cost constraints that are inherent to this market.

1.1 Emissions

It is important to consider the annual sales of small engines in the United States in order to assess their impact on the environment. Fig. 1.1 outlines the increasing contribution of non-road carbon monoxide (CO) emissions to the total US National Emissions Index [3]. CO

emissions can be viewed as incompletely oxidized hydrocarbons, i.e. unburnt fuel. Small engines are a sub-category of the non-road emissions category.

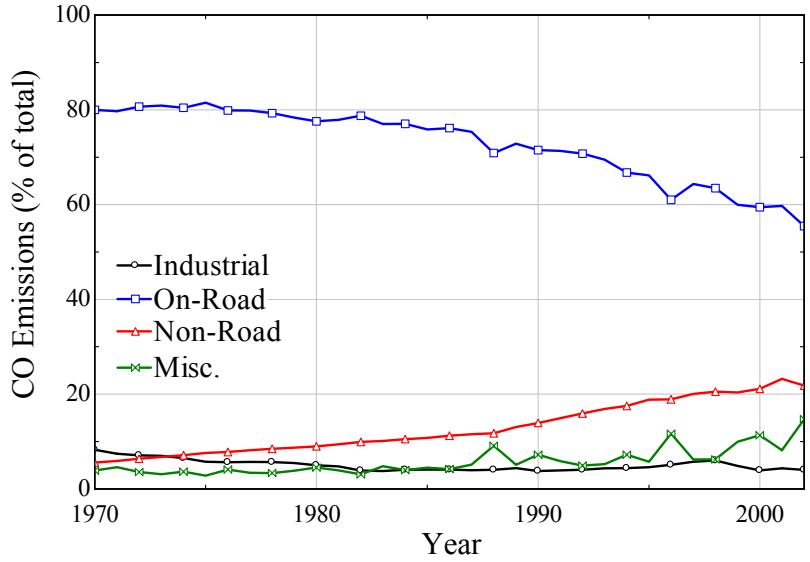

Figure 1.1: CO emissions as a percentage of total CO emissions as a function of year; industrial, on-road, non-road, and miscellaneous sources not including power generation sources are included. Taken from US National Emissions Index [3]

Industrial sources include such things as chemical processing plants, metal processing plants, petroleum production facilities, etc. On-road sources include heavy duty diesel engine transportation and light duty passenger cars. Non-road sources include recreational, farm, and lawn and garden sources. Notice from Fig. 1.1 that since 1970, non-road CO emissions have been steadily rising and represent more than 20% of the total national emissions index in 2002. This rise has occurred in spite of a marked overall decrease in the % total CO emissions for on-road (primarily automotive) sources, a relatively steady CO output from the industrial sector, and a small rise in miscellaneous sources which includes sub-categories such as forest fires.

In the non-road category, lawn and garden CO sources can also be examined in more detail. This segment is displayed in Fig. 1.2 and clearly shows a rapid rise in CO emissions, indicating a large growth over the past quarter century. This assumes that the number of units is increasing and that the rate of emissions is constant for a particular unit and not increasing.

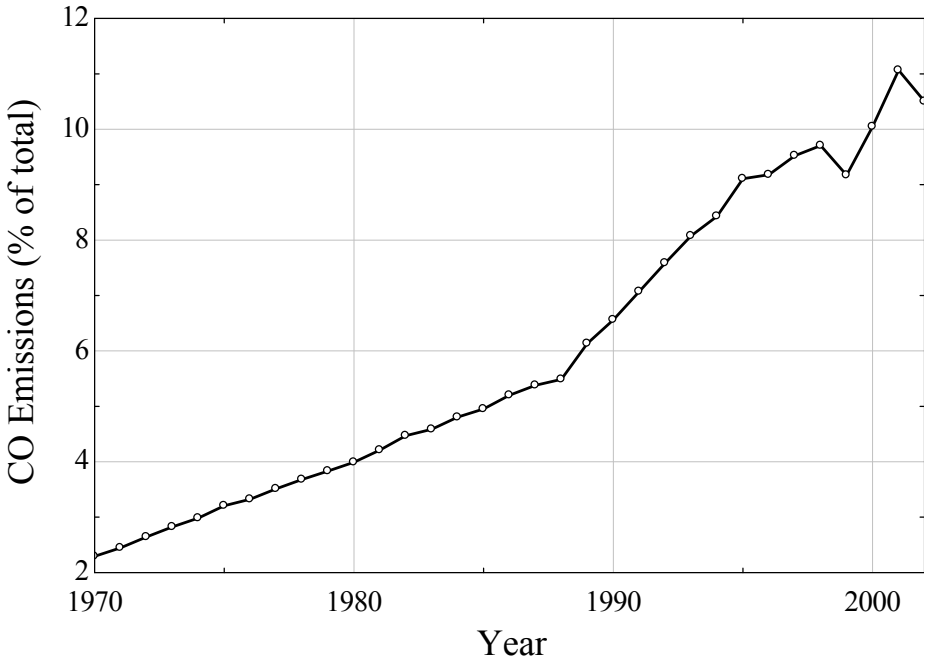

Figure 1.2: CO emissions as a percentage of total CO emissions since 1970 for lawn and garden equipment.

The emission of carbon monoxide is viewed as a health risk; in response to the rise in CO emissions, the EPA has released increasingly stringent regulations and methods to help reduce this pollutant. The EPA has tried to recognize the role that cost plays in the industry and has worked with manufacturers in order to develop ways to reduce CO emissions with currently available and practical technologies. In a preliminary study [4], the EPA recognized the need for an advanced carburetor with improved control of the air-to-fuel ratio (*AFR*) mixture as one of several, conventional technologies for the reduction of CO emissions; other technologies include improved combustion chamber design, lean burn operation, three-way catalysts, etc.

The *AFR* mixture control focuses on a critical parameter, the Air-to-Fuel ratio (*AFR*), which is defined as:

$$AFR = \frac{m_{air}}{m_{fuel}} \tag{1.1}$$

Where m_{air} is the mass of air and m_{fuel} is the mass of fuel delivered by a fuel metering device. As stated previously, for small engines the fuel metering device of choice is a carburetor. The stoichiometric value of the *AFR* is approximately 14.7 for spark-ignition (SI) engines and generally a given engine will produce maximum power when it is fed with a fuel-air mixture that has an *AFR* of approximately 12.5.

1.2 Air-to-Fuel Ratio Control and Design

To understand the need for proper *AFR* control, we can examine the effect that *AFR* has on emissions and power production. When the *AFR* is varied for a particular engine, the resulting exhaust gas constituent concentrations tend to change as shown in Fig. 1.3.

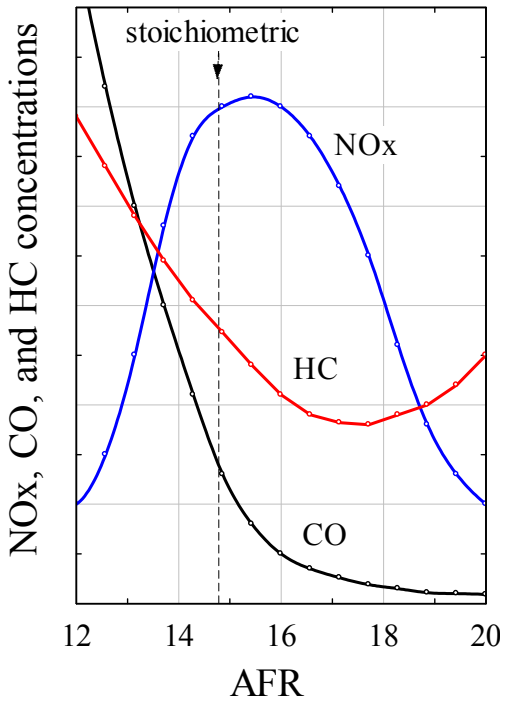

Figure 1.3: Variation of HC, CO, and NOx concentration in the exhaust of a conventional spark-ignition engine with varying *AFR* at constant engine speed [5].

Figure 1.3 shows that the air-to-fuel ratio directly impacts the concentration of the three major pollutants. Leaner mixtures (i.e., mixtures with higher *AFR*) tend to result in lower emissions up to the point where the combustion quality starts to degrade; very high values of *AFR* will result in an increase in the amount of hydrocarbon (HC) in the exhaust due to misfires. Richer mixtures (i.e., lower *AFR*) tend to provide greater combustion stability at the cost of increased CO and HC concentrations. Near stoichiometric conditions, the peak combustion chamber temperatures reach a maximum value which results in maximum NOx production. In summary, Fig. 1.4 shows that emissions control is related directly to the control of the *AFR* that is delivered to the engine.

Figure 1.4 illustrates the qualitative variation in the power produced by the engine as a function of *AFR*; note that the curve is normalized against the peak maximum power produced at the optimal *AFR*.

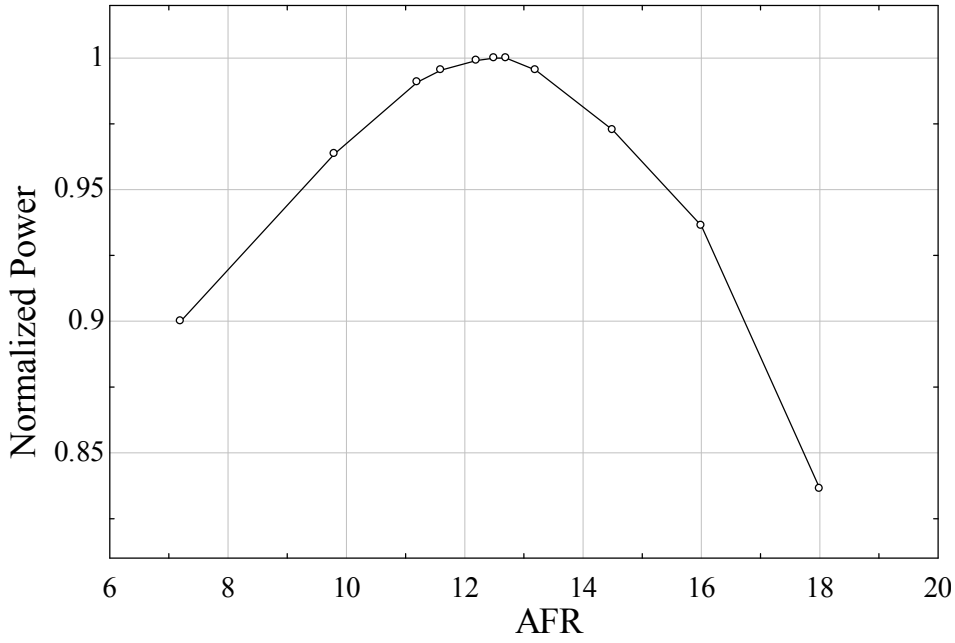

Figure 1.14: Normalized power produced as a function of *AFR* for a generic engine at a given operating condition.

As *AFR* increases, the power rises until a maximum is reached at an *AFR* of around 12.5. Near the stoichiometric value of *AFR*, the power decreases as excess air is added (i.e., as the mixture becomes leaner, power production falls off sharply). Figure 1.4 shows that control of the *AFR* dictates engine performance as well as emission.

During the design and development of a small engine, the *AFR* must be carefully controlled so that the engine produces the desired power and emissions are controlled; currently, a disconnect exists between the engine and carburetor designers. An engine designer requires knowledge of the *AFR* for a prescribed engine before making performance and emissions predictions and, conversely, a carburetor manufacturer needs information about engine performance before a prediction can be made about the *AFR* that should be delivered to an engine.

To summarize, the *AFR* controls both the performance and emissions characteristics of an engine. The development of a predictive model that can be used to understand and design carburetors in order to control the *AFR* is important to the small engine industry and may allow future emissions standards to be met economically while maintaining performance requirements.

1.3 Research Objectives

Understanding that emissions regulations are producing more stringent controls on design and manufacturing in the small engine industry, research objectives for the current study can be defined.

The first research objective to be completed is the creation of a theoretical model to predict fuel flow in a small engine carburetor. Based on previous work performed by Arias [2], this work will concentrate on modeling fuel flow during engine operation under low load and engine speed.

The second research objective was identified during work on the first objective. This objective seeks to further analyze two-phase flow effects in the carburetor. More specifically, it examines the process of fuel and air mixture discharge into the engine. The results of this segment were incorporated into the theoretical model developed above.

1.4 Outline

The remainder of this work is subdivided into 4 chapters. Chapter 2 presents a literature review on engine airflow, carburetor fuel flow during high and low speed, and two-phase effects. The conclusions of this capture indicate opportunities pursued in the next two chapters.

Chapter 3 presents a numerical model which predicts fuel flow from the idle circuit of a small engine carburetor. The model incorporates dynamic fuel flow effects into a model representing a

typical idle path found in a small engine carburetor. Also in this chapter, a parametric study identifies the idle discharge port as the parameter which exerts the most control on the fuel flow delivered.

An experiment performed to further characterize the flow of fuel and air through the idle discharge port is presented in Chapter 4. The chapter includes a detailed presentation of the experimental setup, the analysis of the results, and the presentation of a new correlation to characterize losses at the idle discharge port.

Chapter 5 summarizes the work performed, presents conclusions of the research, and makes recommendations for future work to be performed.

Chapter 2

Literature Review

Section 1.2 provides an introduction and highlights the importance of the air fuel ratio (*AFR*) on the emissions and performance of internal combustion engines. In order to place this work in the context of the needs of the small engine community and prior work in this area, a review of the current literature is included in Sections 2.1-2.7. This literature review will address the current state of the art with regards to *AFR* prediction and carburetor design. This requires a general review and understanding of engine design and performance; specifically, engine airflow will be examined and then the carburetor fuel delivery process will be detailed.

2.1 Engine Airflow Process Description

In a conventional four-stroke engine, when the intake valve opens, the piston is traveling from the top of its stroke (referred to as top dead center, TDC), to the bottom of the cylinder (referred to as bottom dead center, BDC). The increase in cylinder volume associated with this motion decreases the local cylinder pressure and induces fresh air to travel down the intake path and into the cylinder. This process is detailed in Figure 2.1. In the next few sections, the steady/ quasi-steady pressure losses in each part of the intake system will be examined in greater detail.

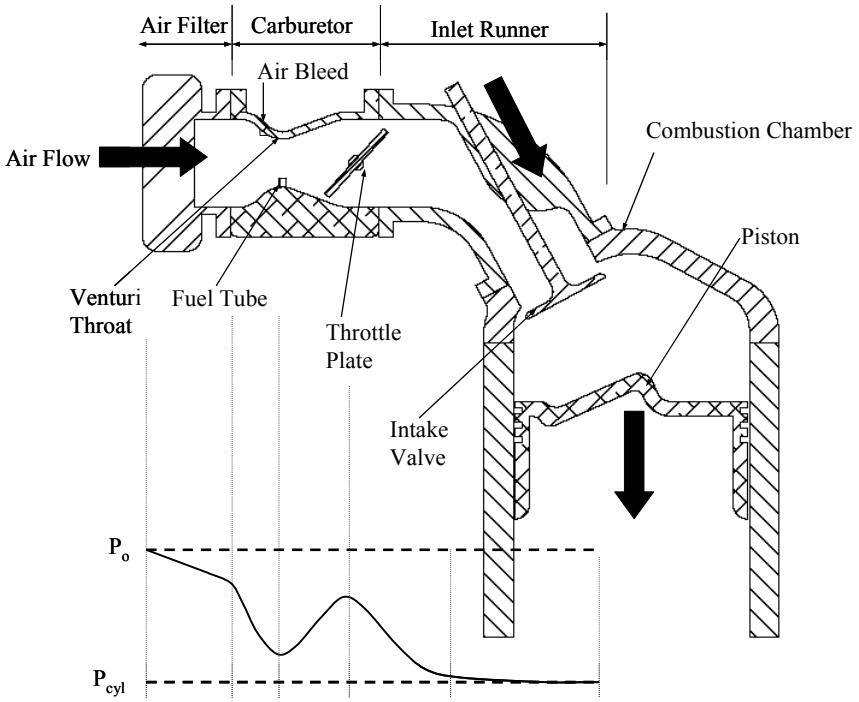

Figure 2.1: Air intake flow path just after intake valve opening (IVO) with the piston descending from top dead center (TDC). Air pressure falls from stagnation conditions (P_o) to cylinder pressure (P_{cyl}) along the intake path due to various losses.

2.1.1 Air Filter/ Inlet System Losses

Several flow obstructions are encountered along the path that leads to the cylinder, and these conspire to decrease the delivered airflow rate from the ideal value given by the cylinder displacement. Starting at the intake inlet, pressure loss occurs due to the restriction associated with the air filter and the geometry of the inlet itself. According to Heywood [5] and others, it is typical to represent the pressure loss of the filtration and inlet system as:

$$\Delta p_{in} = \xi_{in} \rho u_j^2 \tag{2.1}$$

where ξ_{in} is a resistance coefficient, ρ is the air density, u is the inlet velocity, and Δp_{in} is the pressure loss due to the restriction. Along this branch of the intake system, heating or cooling of the intake air may also occur that can decrease or increase the air density,

respectively. Next, upon entering the inlet of the carburetor, the airflow will encounter obstacles in the flow path that may also slightly restrict and disrupt airflow. Arias and Shedd [6] showed that the inlet obstacles do not create a noticeable effect on the flow field. This is a consequence of the favorable pressure gradient that keeps the boundary layer attached, thus preventing separation and significant pressure losses are avoided in the carburetor until the air flow reaches the fuel tube. Figure 2.2 shows a representative carburetor Venturi with inlet obstacles (e.g. air bleeds) and a fuel tube protruding into the flow field.

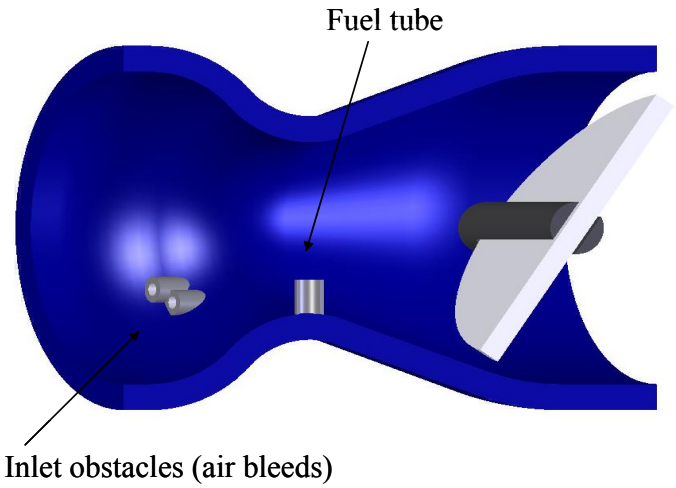

Figure 2.2: Representative Venturi showing inlet obstacles and the fuel tube

2.1.2 Venturi Flow Losses

As the flow starts to accelerate in the throat of the venturi (due to the converging geometry), a negligible quantity of air enters the air bleed systems of the carburetor where it mixes with fuel in the emulsion tube; this process will be discussed more completely in Section 2.4.1. The acceleration of the air flow results in a substantial decrease in the static pressure. Figure 2.3 shows some computational fluid dynamic predictions obtained by Arias and Shedd for a representative Venturi geometry. Notice

that the static pressure remains relatively constant in the converging portion of inlet, however, when the flow field encounters the fuel tube, the pressure rises at the stagnation region that forms at the leading edge of the fuel tube and a large wake forms behind the fuel tube. This is shown clearly in Figure 2.3(b).

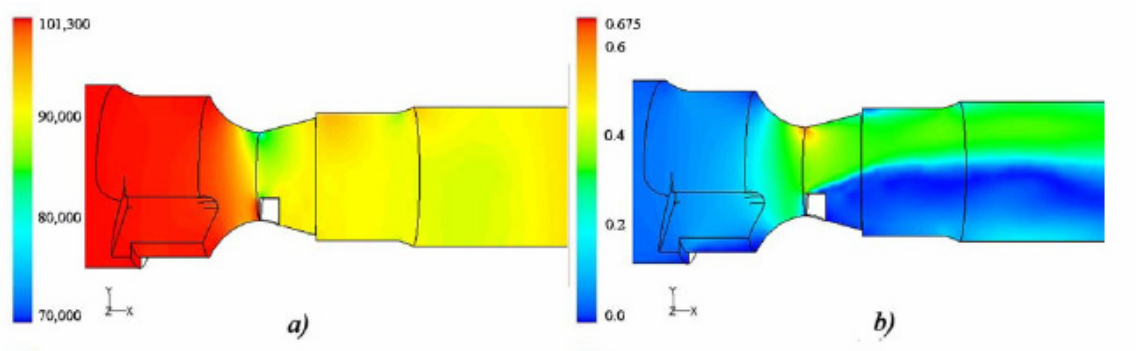

Figure 2.3: Results from CFD study by Arias et al showing a.) Static pressure and b.) Mach number.

If the viscous shear terms are ignored in this short converging region, the decrease in pressure can be calculated using the Euler equation for compressible inviscid flow as provided by White [7].

$$\rho \frac{Dv_i}{Dt} + \frac{\partial P}{\partial x_i} = 0 \tag{2.2}$$

where the term $\frac{Dv_i}{Dt}$ represents the convective acceleration along each principal direction of the flow and $\frac{\partial P}{\partial x_i}$ represents the pressure gradient.

The solution of the equation (2.2) as written is a formidable task, but if the channel is treated as one-dimensional, and the assumption is made that the flow is isentropic, then according to Heywood [5], the pressure at the throat of the venturi can be expressed as:

$$\dot{m}_{actual} = C_d A_t [2\rho_o (p_o - p_t)]^{1/2} \Phi \tag{2.3}$$

$$\Phi = \left\{ \frac{[\gamma/(\gamma-1)][(p_t/p_o)^{1/2} - (p_t/p_o)^{(\gamma+1)/\gamma}]}{1-(p_t/p_o)} \right\}^{1/2} \tag{2.4}$$

where $\dot{m}_{actual}$ represents the actual mass flow rate through the device, C_d represents the discharge coefficient of the venturi, A_t represents the flow area at the throat, and γ stands for the ratio of specific heats (assumed to be 1.4, which is consistent with air). The subscripts *o* and *t* are associated with stagnation and throat conditions respectively, and finally Φ represents the compressibility factor of the airflow.

Downstream of the venturi throat and fuel tube is a diverging channel, which serves to decelerate the flow and recover pressure that was used to drive fuel flow in the venturi throat. In this region, an adverse pressure gradient exists and thus separated flow is likely to occur at the locations shown in Figure 2.3.

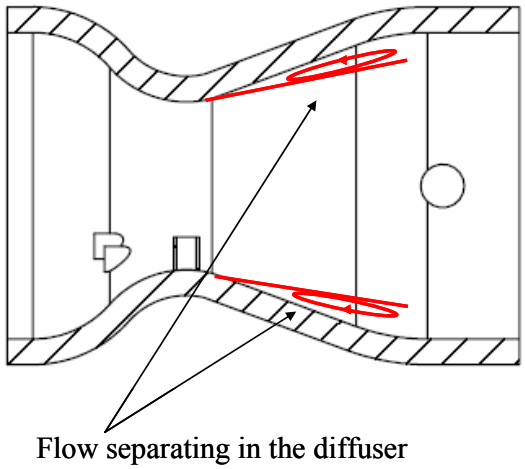

Figure 2.4: Flow separation in the presence of an adverse pressure gradient

2.1.3 Pressure Losses at the Throttle Plate/Blade

Until the throttle plate, the total pressure loss in the system is minimal. The throttle blade is the main control system for the engine and governs the airflow delivered. At wide open throttle conditions (WOT), the pressure loss due to the restriction of the throttle plate is minimal (the throttle plate is oriented so that it is parallel to the flow), but at all other angles the throttle plate imposes a significant restriction to airflow. At these conditions, the airflow around the throttle plate forms a highly three-dimensional, unsteady, pulsating flow as reported by Alsemgeest et al. [8] and reproduced in Figure 2.5. Figures 2.5a and 2.5b, produced by computational fluid dynamic simulations, illustrate a velocity vector plot of the flow field at a throttle angle of 47^{o} with a plot of the *u*, *v*, and *w* velocity components versus time for the same conditions directly behind the throttle. The figure indicates a solution that has large vorticular structures shedding from the backside of the throttle blade at characteristic frequencies that increase as a function of throttle angle, as summarized in Table 2.1.

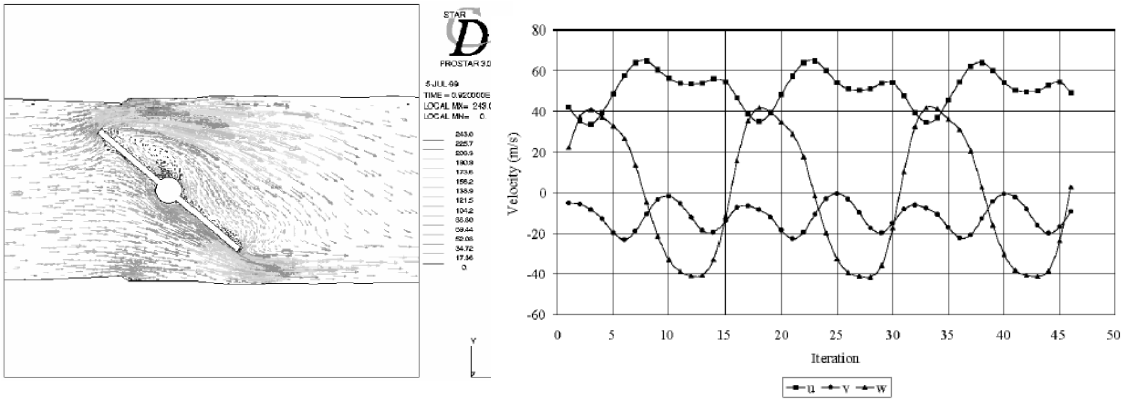

Figure 2.5: Velocity vector plot of flow past a throttle plate with a record of *u*, *v*, and *w* velocity components as a function of iteration number, which can be viewed as a time scale. Reproduced from Alsemgeest et al. [8]

Table 2.1: Vortex shedding frequencies for different throttle angles. Reproduced from Alsemgeest et al. [8]

Angle	Average Period	Frequency Range	Average Frequency
α (°)	T (s)	ΔN (Hz)	N (Hz)
12.5	-	-	-
19.0	4.41×10^{-3}	-	227
30.0	3.65×10^{-3}	267-278	274
47.0	2.98×10^{-3}	329-333	332
60.0	2.28×10^{-3}	429-450	438

Despite the inherently complex nature of the flow past the throttle plate, Woods and Goh [9] showed through experiments and simple 1-D models that the flow rate through a butterfly valve, i.e., a throttle blade, can be accurately represented using a quasi-steady method. These simple steady and quasi-steady methods can be combined with experimentally determined discharge coefficients, and used to produce a map of the throttle operating regime where the mass flow rate is a function of engine speed, throttle angle, and manifold pressure, as shown by Pursiful et al. [10] in Figure 2.6.

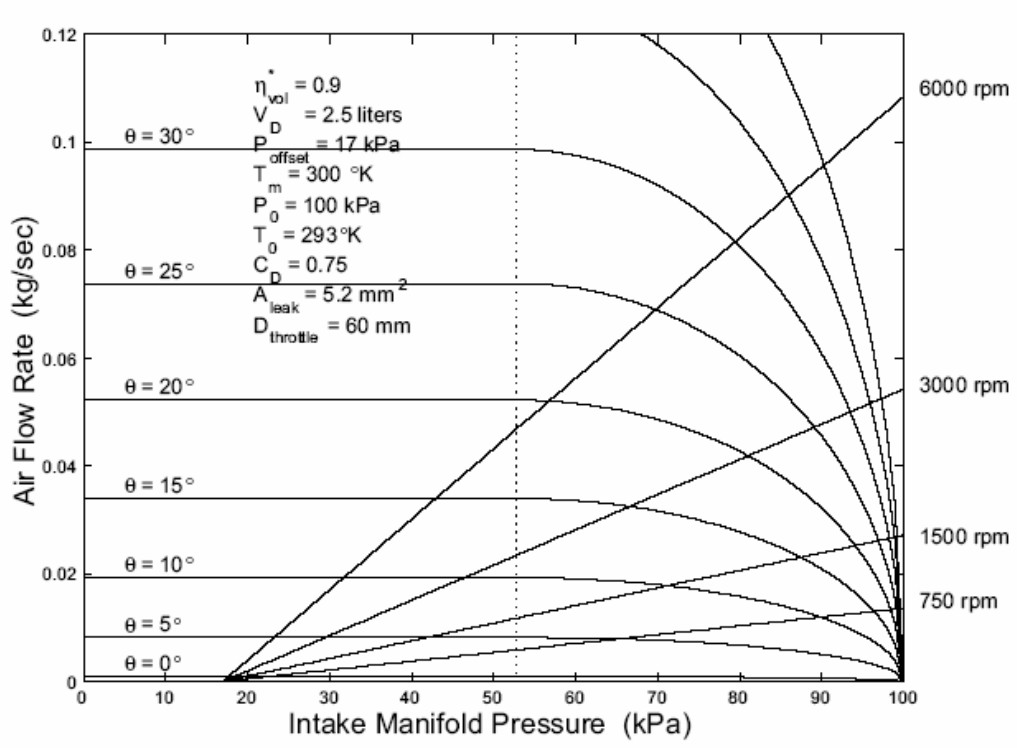

Figure 2.6: Air mass flow rate for varying throttle angles as a function of manifold pressure bounded by limits for differing engine speeds. Reproduced from Pursiful et al. [10].

Figure 2.6 shows that, at low manifold pressures, the mass flow rate reaches a maximum despite further decreases in manifold pressure or further increases in engine speed. These regions exhibit choking at the throttle plate that occurs when

$$\frac{p_t}{p_o} = \left(\frac{2}{\gamma + 1} \right)^{\gamma/(\gamma+1)} \tag{2.5}$$

For air, this condition occurs at a pressure ratio of approximately 0.528.

In single cylinder applications, the assumption of steady or even quasi-steady flow is questionable because the amplitude of the flow variations is large, however, for applications with numerous cylinders and a common manifold, the use of steady flow equations is reasonable because the amplitudes of the cylinder pressure variations is

reduced. Harrington and Bolt [11] examined a V8 engine operating under steady conditions and applied a steady state analysis to examine fuel flow. The study includes an analysis of the airflow path and utilizes the 1-D isentropic flow relations previously defined to study flow past a throttle blade to find that the area of the flow passage past the throttle plate is given by

$$\begin{aligned} A(\theta) &= \frac{\pi D^2}{4}\left[1-\frac{\cos\theta}{\cos\theta_o}\right] \\ &+\frac{d}{2\cos\theta}\sqrt{D^2\cos^2\theta - d^2\cos^2\theta_o} \\ &+\frac{D^2\cos\theta}{2\cos\theta_o}\sin^{-1}\left(\frac{d\cos\theta_o}{D\cos\theta}\right)-\frac{d}{2}\sqrt{D^2-d^2} \\ &+\frac{D^2}{2}\sin^{-1}\left(\frac{d}{D}\right) \end{aligned} \tag{2.6}$$

where $A(\theta)$ stands for the throttle area as a function of throttle angle θ, D represents the diameter of the throttle bore, d represents the throttle shaft diameter, and θ_o represents the non-zero throttle closing angle. Figure 2.7 describes the variables of equation (2.6). In this analysis, Harrington made the assumption that the throttle can be approximated as a nozzle with zero pressure recovery downstream of the throat.

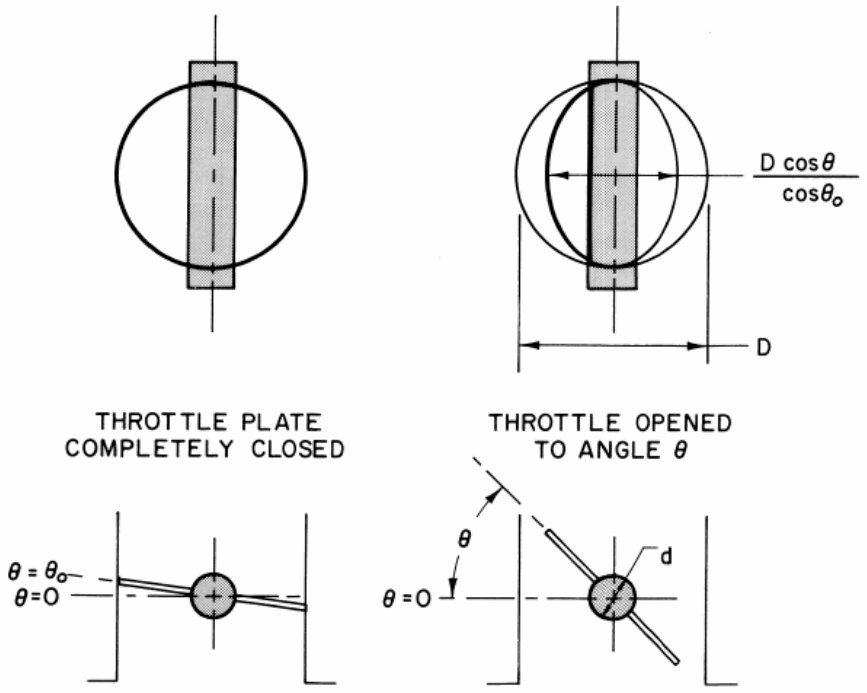

Figure 2.7: Variables in the equation used to find the throttle plate area.

Once past the throttle blade, the airflow proceeds past the idle and transition ports where fuel is delivered under idle and part load conditions. The static pressure at this point is now significantly lower than when the air entered the intact tract due to losses incurred at the throttle at conditions other than WOT.

2.1.4 Intake Runner Pressure Losses

After the airflow has left the carburetor body and enters the main inlet runner, it experiences additional pressure losses through friction and heating of the inlet air through wall conduction processes. Once past the inlet runner, the flow enters the vicinity of the inlet valve where the flow area narrows substantially due to the presence of the valve guide and the boss used to support the guide. Upon entering the cylinder, the flow must now expand and change direction. Intake runner geometry pressure losses have been studied extensively in the literature by Takizawa [12], Ohata [13]. Chapman [14], and

others. Figure 2.8 gives detailed information about where pressure losses generally occur in intake runners. This diagram indicates that most losses occur around the valve and valve seat, identified as regions 6,7, and 8. Heywood [5] identified this area for further study and discovered that the discharge coefficient does not remain constant over the duration of valve lift due to the presence of three different flow regimes. These three flow regimes are identified in Figure 2.9.

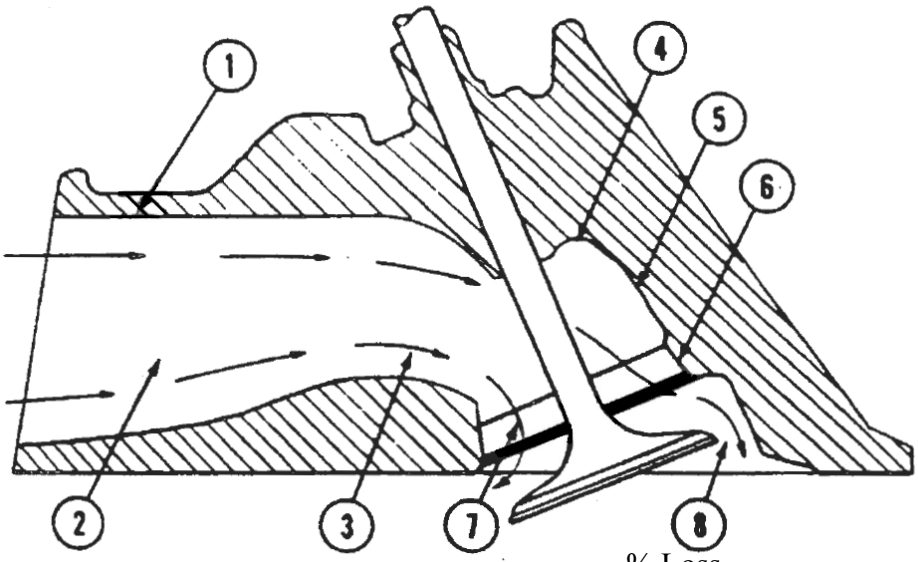

Source of Flow Loss	% Loss
1. Wall friction	4
2. Contraction at push-rod	2
3. Bend at valve guide	11
4. Expansion behind valve guide	4
5. Expansion, 25°	12
6. Expansion, 30°	19
7. Bend to exit valve	17
8. Expansion exiting valve	31
	100

Figure 2.8: Pressure loss sources in a generic SI engine intake runner. Adapted from Superflow Flowbench 600 Instruction Manual [15]

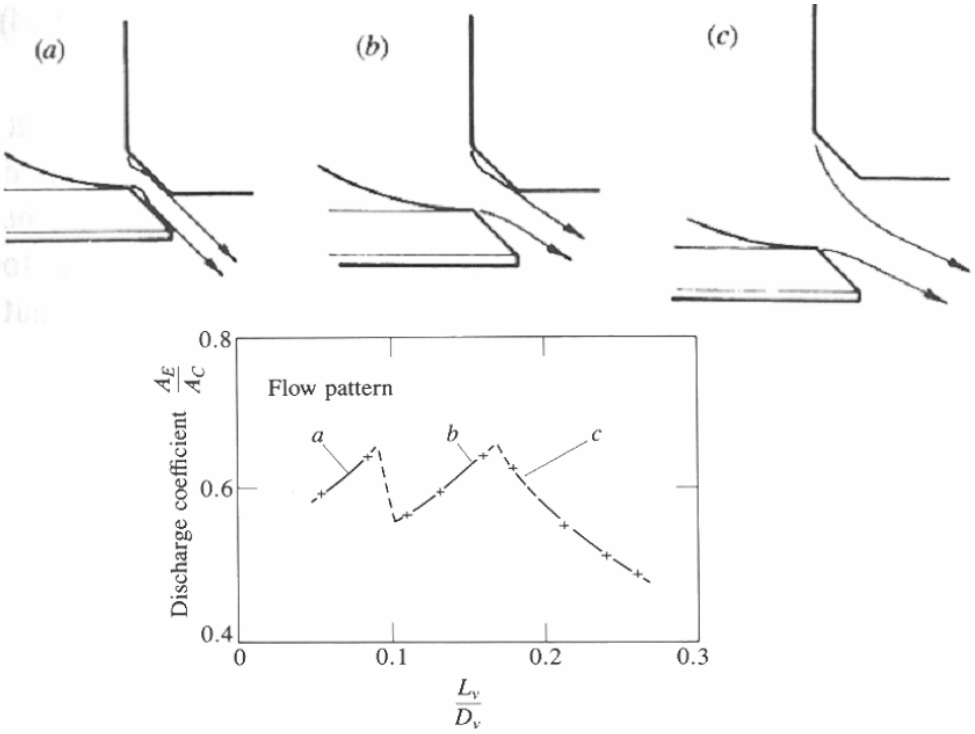

Figure 2.9: Flow regimes present in typical inlet valve flow and their effect of discharge coefficients, from Heywood [2.1].

In Figure 2.9, region (a) identifies a regime of low lift where the airflow remains attached to both the valve and seat with increasing lift. Upon further increases in the valve lift/valve diameter ratio (L_v/D_v) around 0.1, the flow separates from the valve and a sudden decrease in the discharge coefficient is encountered, identified as the trough between region (a) and region (b). The discharge coefficient then steadily rises with further increases in valve lift until the flow separates from the valve seat as well around $L_v/D_v = 0.17$. This region of complete separation is identified by region (c). It can be seen from this discussion that the discharge coefficient is inherently unsteady during actual engine operation, but Bicen et al. [16] have found that steady flow discharge coefficients can be used to adequately predict dynamic engine performance. These

discharge coefficients can be combined with equations (2.3, 2.4) to model the pressure loss in the intake runner/ intake valve system.

In addition to the losses just described, the decrease in area around the guide boss and the valve is significant enough that choking can occur at high engine speeds. Choking conditions and the resultant downstream pressure can be determined with the same method as that for the throttle plate by equation (2.5).

In the research literature available up until the present, pressure losses in the intake system have been mostly quantified as steady flow losses with experimentally determined discharge coefficients. During actual engine operation unsteady phenomena play a large role in determining cylinder filling performance and pressure losses in the intake system. Unsteady phenomena will be examined next followed by a brief review of the different methods used to model actual engine intake system airflow.

2.2 Unsteady Gas Flow Effects in the Intake System

During actual engine operation, the effective valve area is driven by the profile machined onto to the camshaft lobes; the valve area changes throughout each revolution of the engine. The volume of the cylinder also changes during each revolution due to the motion of the piston and the crankshaft. These two effects combine to produce an unsteady, constantly varying pressure distribution in the intake manifold. The pressure distribution varies with time in a nearly sinusoidal fashion. This changing pressure distribution is the force that drives airflow into and out of the combustion chamber. However, the mass of the intake air, although small, has significant inertia when it reaches high speeds; the inertia of the intake air can be utilized in order to provide

enhanced cylinder filling at higher engine speeds due to the so-called ram effect. Acoustic phenomena are also occurring and contribute to enhanced filling.

2.2.1 Volumetric Efficiency

It is convenient at this point to identify a parameter that quantifies cylinder filling performance. The volumetric efficiency is defined as actual volume rate of airflow into a cylinder divided by the rate at which volume is displaced by the piston. This parameter accounts for all losses and gains encountered in the engine air intake system, including heating, friction, choking, ram effects, and wave effects (discussed next). In terms of process variables, volumetric efficiency is defined as:

$$\eta_{vol} = \frac{m_a}{\rho_a V_d} \tag{2.7}$$

where m_a is the mass of air inducted, ρ_a is the density of the inlet air at the inlet to the engine, and V_d is the volume displaced by the piston. Volumetric efficiency then determines how much air actually reaches the combustion chamber, and can be regarded as a fundamental parameter in engine performance. Volumetric efficiency will be used in conjunction with the air-to-fuel ratio (*AFR*) mentioned previously to determine a wide range of emissions characteristics and performance parameters.

2.2.2 Ram Effect

At the end of the inlet stroke, as the piston is approaching TDC, the column of fresh charge that is moving towards the intake valve has built up significant momentum. Therefore, even after the piston reaches and proceeds past TDC, cylinder filling will continue. This inertial effect will increase with engine speed and, taken alone, would provide a large increase in trapped mass at intake valve closing (IVC); however, other

high speed losses, such as friction and choking in the valve tend to reduce the efficiency of the filling process as engine speed increases and therefore offset this inertial effect. Figure 2.10 provides insight into how volume, determined by intake runner length and diameter, plays a role in governing this inertial phenomenon.

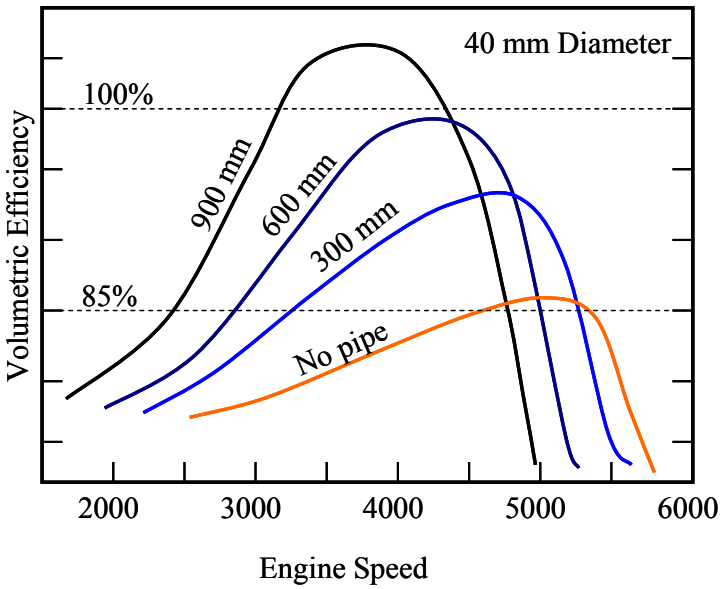

Figure 2.10: Induction inertial ram cylinder charging for a given engine. Adapted from Heisler [17].

Figure 2.10 shows that it is possible to achieve a trapped mass that is larger than the mass that would fill cylinder volume of the engine under STP conditions. This possibility is indicated by a volumetric efficiency curve that surpasses 100%. Also one can see that longer inlet runner lengths produce increased volumetric efficiency due to increased momentum, but the curve falls quickly once the maximum is reached. From this graph it is also obvious that a tradeoff is occurring between flow velocity, which generates increased momentum due to inertial forces, and friction produced by increased shear along the pipe walls. Inertial ram charging is an unsteady effect that can have a

profound effect on engine airflow and is therefore important to the carburetor fuel metering process.

2.2.3 Wave Tuning

The intake valve opens at the beginning of the induction stroke when the piston approaches TDC. Upon opening, a negative pressure wave is produced that travels up the intake port at the speed of sound. Upon reaching the end of the intake tract, the wave compresses, and reflects back down the intake port as a positive pressure wave. If this pressure wave reaches the intake valve during IVC, a gain in cylinder filling, and volumetric efficiency, can be realized. This effect is coupled with, but distinct from, inertial ramming because it is based on acoustic waves and not the inertia of the air charge. Timing the pulse to reach the intake valve at IVC can be achieved for only one distinct engine speed. Additional, less powerful pulses (i.e. the 2^{nd}, 3^{rd}, and 4^{th} pulses associated with additional reflections) can be timed to reach the intake valve at IVC as well. This behavior produces distinct peaks and valleys in a graph of volumetric efficiency as a function of engine speed, as shown in Figure 2.11 for a single cylinder engine with a constant runner diameter

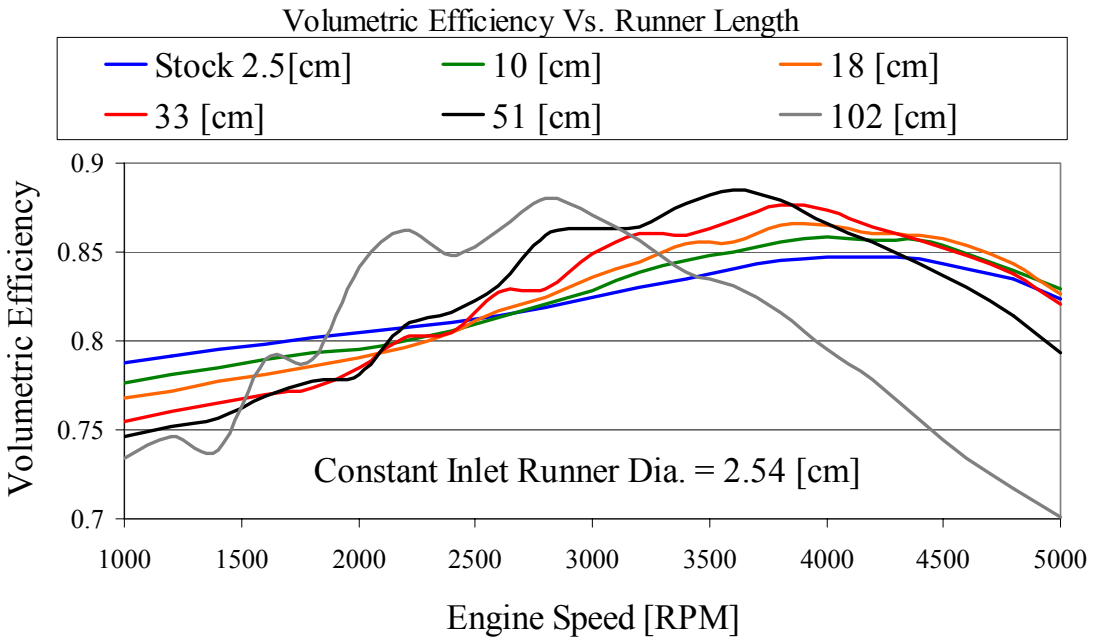

Figure 2.11: Volumetric efficiency for a single cylinder engine with varying runner lengths. Created by the author.

Figure 2.11 shows that wave tuning effects can significantly alter the volumetric efficiency of an engine over the range of engine speed operation compared to the baseline configuration. Examining the plot for a 40 in. runner length, distinct peaks and valleys appear, indicating the effect of different characteristic pulses serving to increase the effective cylinder filling rate. Also apparent is that, after the maximum volumetric efficiency has been attained, the performance of the engine decreases steadily as engine speed is further increased, again indicating the trade-off between wave timing, friction, and inertial ramming. Finally, we can differentiate between inertial ramming and wave tuning by recognizing that the increase in volumetric efficiency, for a given pipe length, would be monotonic if wave tuning effects were not present.

Figure 2.11 was generated by an engine model in which all of the effects discussed in this section have been accounted for. The solution of the system of equations needed to generate a result akin to Figure 2.11 is a daunting task, yet it is intimately linked to the overall determination of airflow rate in an engine. The carburetor is a passive fuel metering device that is driven by the air flow rate; therefore, accurate prediction of the air flow rate is extremely important in order to predict the fuel flow that is produced by a small engine carburetor. The next section will discuss the systems of equations and the methods that are used to generate results such as shown in Figure 2.11. The discussion will then proceed to current models that are used to determine fuel flow from small engine carburetors.

2.3 Airflow Modeling Techniques

Airflow through the intake system can be simulated using a variety of different models that are characterized by different degrees of accuracy and computational requirements. Several of these models are discussed in this section.

Using basic engine design parameters such as bore, stroke, engine speed, connecting rod length, etc., Horlock and Winterbone [18] describe three separate techniques that can be used to model the flow of air through an engine: the Quasi-Steady Method (QSM), the Filling and Emptying Method (FEM), and the Finite Element Method or Wave Action Method (WAVE). The characteristics of these techniques are summarized in Table 2.2.

Table 2.2: Characteristics of the three models typically used to compute the air flow through an engine, from Chung [19]

Item	QSM	FEM	WAVE
Mathematical Complexity	Simple	Complex	Complex
Accuracy	Low	High	High
Reliance on empirical data	High	Low	Low
Calculation speed	Fast	Slow	Slow

2.3.1 The Quasi-Steady Method

The Quasi-Steady Method (QSM), described by Heywood [5], is based on a steady state compressible flow model. Extension of the steady flow equations into the time domain is accomplished by relating the volumetric flow rate to the change in engine volume with time, as described by Stone [20].

$$V = V_C + A\left[r(1-\cos\theta) + \left\{ l - \sqrt{(l^2 - r^2 \sin^2\theta}\right\} \right] \tag{2.8}$$

$$\frac{dV}{dt} = A\left[r\sin\theta\frac{d\theta}{dt} + (l^2 - r^2\sin^2\theta)^{-1/2} r^2 \sin\theta\cos\theta\frac{d\theta}{dt} \right] \tag{2.9}$$

where V is the instantaneous cylinder volume. V_C is the clearance volume (in the combustion chamber). A is the piston cross-sectional area, r is the crank throw (stroke/2), θ is the crank angle , l is the connecting rod length, and t is the time. Cylinder pressure couples to the rate of change of engine volume through use of a polytropic relation given as:

$$pV^{\gamma} = K \tag{2.10}$$

where K is a constant determined by experimental data. Equation (2.10) assumes that the working fluid of the engine is treated as an ideal gas. Crank angle relates to time through the following,

$$\frac{t}{\theta} = \frac{RPM}{6} \tag{2.11}$$

where *RPM* specifies engine speed in [rev/min], $\frac{t}{\theta}$ is the time per crank angle degree of engine rotation [s/deg], and the 6 accounts both for the conversion from minutes to seconds and from revolutions to degrees.

The engine air mass flow rate is governed by the same isentropic compressible flow equations, repeated here for convenience, in slightly different form and incorporating discharge coefficients as corrections for real gas effects. For subsonic flow the engine mass flow rate is:

$$\dot{m} = \frac{C_D A_R P_O}{\sqrt{R T_O}} \left(\frac{P_R}{P_O} \right)^{(1/\gamma)} \left\{ \frac{2\gamma}{\gamma - 1} \left[1 - \left(\frac{P_R}{P_O} \right)^{(\gamma-1)/\gamma} \right] \right\}^{1/2} \tag{2.12}$$

while for choked flow, the mass flow rate is:

$$\dot{m} = \frac{C_D A_T P_O}{\sqrt{R T_O}} \gamma^{1/2} \left(\frac{2}{\gamma + 1} \right)^{(\gamma+1)/2(\gamma-1)} \tag{2.13}$$

where $\dot{m}$ is the mass flow through the duct or region under considerations, C_D is the discharge coefficient that characterizes the region under consideration, A_R is the minimum area or reference area, P_O is the stagnation inlet pressure, P_R is the static

pressure at the reference area, γ is the ratio of specific heats (1.4 for air), R is the gas constant for air, and T_O is the inlet stagnation temperature.

To utilize this method, each element in the flow path is represented with equations 2.12 and 2.13. This means that across the air filter/inlet system, through the venturi, across the throttle blade, and through the valve system, the pressure losses are calculated and summed to calculate the mass flow.

In calculating the mass flow rate of the engine, the QSM model treats the engine as a series of interconnected components, and is well represented by electrical analog in which mass flow rates are analogous to current, pressure ratios are analogous to voltages, and friction is analogous to resistance. Mass flow rates must balance across components and pressure must be continuous from component to component. The engine manifold is assumed to have negligible volume, and since mass accumulation and inertia are not included in the model, the air flow response of the engine is instantaneous.

The QSM model uses the experimentally determined, steady-state characteristics of each different engine elements to develop the required discharge coefficients, and therefore the model is extremely dependent on empirical information. The QSM model also neglects the intermittent nature of the engine cycle.

2.3.2 The Filling and Emptying Method

The Filling and Emptying Method (FEM) is a mathematical description of airflow phenomena that treats the engine manifolds as finite volumes and therefore includes the effect of mass accumulation. The FEM incorporates transient effects by employing non-linear ordinary differential equations for the conservation of mass, momentum, and energy, as described by Nowakowski and Sobieszczanski [21] for a 1-D model running

from the air filter to the combustion chamber (the x coordinate is along the direction of flow):

$$\frac{\partial \rho}{\partial t} + \frac{\partial}{\partial x}(\rho u) = 0 \tag{2.14}$$

$$\frac{\partial}{\partial t}(\rho u) + \frac{\partial}{\partial x}(\rho u^2 + p) = 0 \tag{2.15}$$

$$\frac{\partial}{\partial t}\left(\rho \frac{u^2}{2} + \frac{p}{\gamma - 1}\right) + \frac{\partial}{\partial x}\left[\rho \frac{u^2}{2} + \frac{\gamma}{\gamma - 1} p\right] = 0 \tag{2.16}$$

The air flow is assumed to obey the ideal gas equation of state:

$$p = \rho R T \tag{2.17}$$

where p is the air pressure in the finite volume, ρ is the air density in the finite volume, u is the air velocity in the coordinate direction in the finite volume, and T is the air temperature in the finite volume.

The FEM model requires less empirical information to describe the airflow through the intake manifold but its computational time requirement is an order of a magnitude more than the QSM model. The FEM model describes the different volumes using a single pressure and temperature, so wave tuning information cannot be obtained from the model output. This means that if the intake runner is modeled as a single volume, then the FEM model will not provide a pressure distribution along the length of the runner; rather, a single pressure represents the entire intake runner. However, with the short intake runners encountered in most small engine designs, wave tuning effects are nearly negligible. Therefore, use of the FEM would be appropriate to describe the cyclic nature of most small engines

2.3.3 Finite Element Method or Wave Action Method (WAVE)

The solution of the unsteady compressible gas flow equations in one dimension throughout the entire flow path is generally accepted to be the most accurate, but time consuming, method to model airflow in an intake manifold. Work performed by Benson [22], Winterbone [23], Zhu and Reitz [24] and others has shown that the WAVE method can provide predictive results which closely match experimental data for manifold pressure and airflow fields; an example is shown in Figure 2.12.

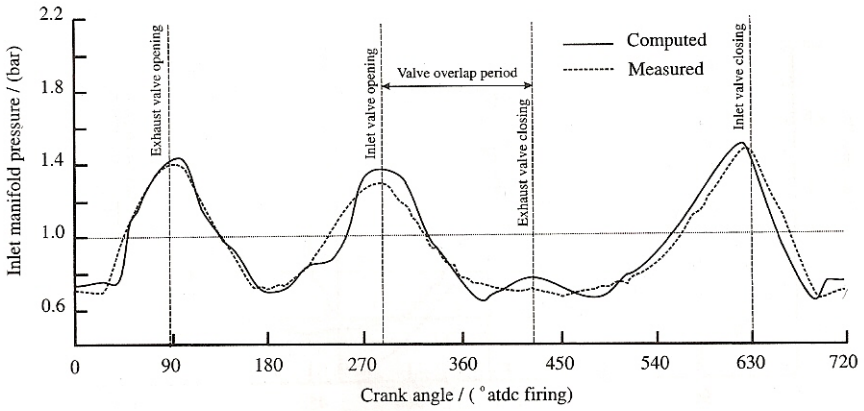

Figure 2.12: Representative example of the predictive capabilities of WAVE action techniques for predicting pressure profiles in operating engines. Formula 1 intake manifold operating at 13,000 RPM. Taken from [23].

The power of the WAVE method relies on the solution of heterogeneous pressure field in different volumes of the inlet and exhaust system of a particular simulated engine. This approach accounts for resonances and the subsequent tuning effects produced by different lengths, volumes, and geometries. One-dimensional wave action methods have been integrated with several commercial engine packages such as AVL Boost [25], Ricardo WAVE [26], and GT-Power [27].

For research conducted with small engines at low engine speeds, any of three aforementioned methods would be acceptable for calculating the pressure and airflow fields inside a small engine intake manifold. Based on the discussions above, the WAVE model will provide the most accurate results, followed by the FEM model, and finally the QSM model. To produce the most accurate intake manifold airflow simulations under idle and transitional conditions, the GT-Power software was chosen to simulate the intake airflow. GT-Power uses wave action techniques to incorporate all relevant unsteady effects.

At this point, a review of the relevant physics occurring in the intake system (with regards to airflow) has been completed. A software program that accounts for all of the important phenomena described here has been selected in order to model the pressure distributions and mass airflow rate in the intake system. In subsequent section, some typical models of carburetor fuel delivery will be investigated; based on this discussion, an assessment will be made of the current needs of the small engine community with regards to fuel flow prediction will be carried out.

2.4 Carburetor Fuel Flow Process Description

The development of an idle and transition model for a small engine carburetor requires an in-depth understanding of the processes that govern the fuel delivery under wide open throttle (WOT) conditions, (i.e., an understanding of the main fuel path delivery system). Therefore, an attempt is made to thoroughly describe both systems in this review. Furthermore, idle and transition systems/circuits incorporate many of the same devices as that of main path systems and thus the individual circuits, which have vastly different requirements, can be viewed as somewhat similar in function, design, and

operation. Figure 2.13 presents the main circuit and idle circuit found in a prototypical small engine carburetor.

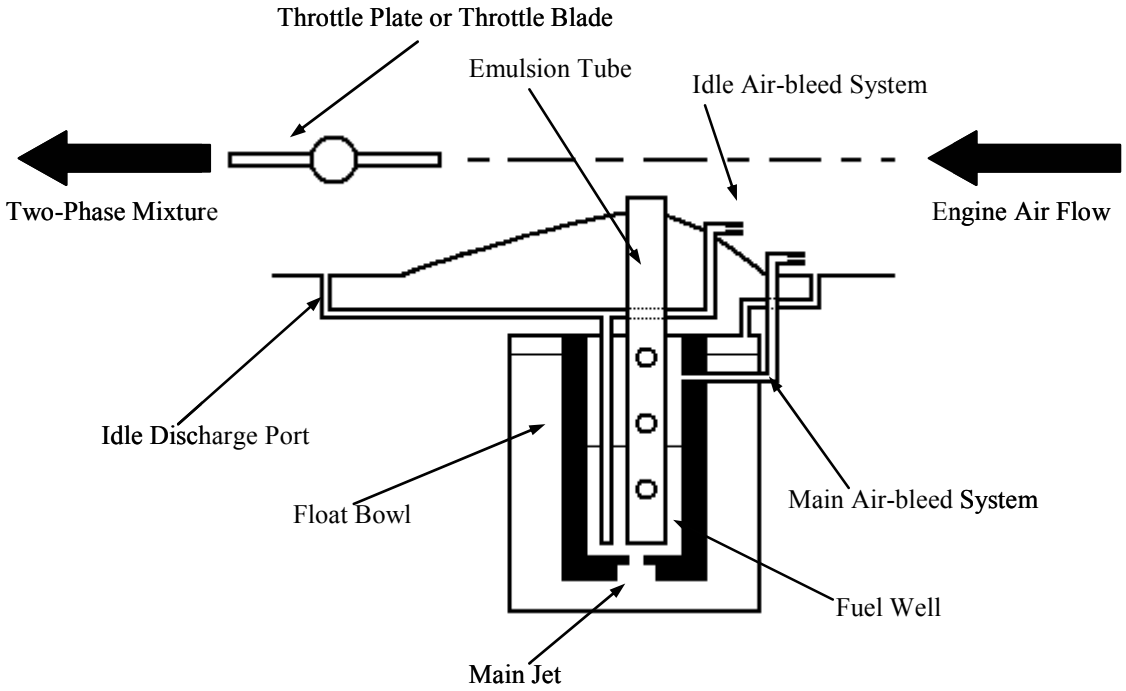

Figure 2.13: Significant features of a modern small engine carburetor.

2.4.1 High Speed Operation of the Main Path System

During high speed operation, the throttle plate is almost wide open (as shown in Figure 2.13), and air flow is drawn through the engine and accelerated by the shape of the venturi. At the throat of the venturi, the static pressure of the air reaches a minimum. This low pressure drives fuel flow from the float bowl through the main jet, which is a small metering orifice, into the fuel well. From the fuel well, the fuel is drawn up into the emulsion tube. At this point, the fuel encounters air being forced into the main air-bleed system. The air-bleed system, also known as the air-bleed compensation system, contains a metering orifice, a series of bends, and other obstructions that are collectively known as minor losses. At the end of the main air-bleed system, air will mix with the

fuel traveling up the emulsion tube to form a two-phase mixture. The mixture is discharged from the end of emulsion tube into the engine air stream.

The height of the liquid fuel in the fuel well is determined by a balance between the pressure inside the emulsion tube and the pressure at the surface of the fuel in the fuel well. Depending on the pressure conditions and therefore the liquid fuel height, a different number of emulsion tube holes will be exposed and this will tend to alter the resistance to air flow through these holes. This mechanism regulates the rate of mixing that occurs between the fuel and air. The amount of air driven into the emulsion tube decreases the mean density of the mixture, and increases the fuel flow for a given pressure drop. However, incorporating an air-bleed system decreases the pressure differential across the main jet which decreases fuel flow. Therefore, the correct balance between compensating air flow and jet size must be determined to provide the correct mixture. Furthermore, an additional complication arises from the increase in air mass of the two-phase mixture. The additional air flow increases the pressure drop along the emulsion tube compared to that of a pure single-phase fluid. Therefore another balance is created between increased two-phase flow and increased two-phase pressure drop.

At this point it is important to clarify and summarize the coupled performance features of the emulsion tube and air-bleed compensation system. The features are listed as follows:

1. The addition of bleed air to the main circuit through use of an air-bleed system decreases the mean density of the mixture and increases fuel flow for a given pressure differential between the main jet and the venturi throat.

2. Incorporating air-bleed compensation reduces the pressure differential driving fuel flow through the main jet and this decreases fuel flow through the main jet system.
3. The effects of 1 and 2 are balanced by sizing the main jet metering orifice and the air-bleed metering orifice to provide the correct *AFR* for a given operating condition.
4. The cumulative effect of the air-bleed system reduces the fuel flow delivered to the engine by providing a leaning effect compared to the fuel flow that would be delivered without an air-bleed system. In this manner, the air-bleed system, "bleeds off" some of the pressure differential driving fuel flow.
5. Leaning the *AFR* during and after air-bleed activation creates a fuel flow characteristic curve that is proportional to engine airflow demand. This helps stabilize the *AFR* around a constant value when operating over a wide range of WOT and part throttle conditions. Effectively, the fuel flow rate becomes linearly proportional to engine air flow. Air-bleed system activation will be further discussed in section 2.5.1.
6. With the use of compensating air that effectively leans the mixture, the main jet diameter can be increased and this eases manufacturing complexity.
7. Use of an emulsion tube air bleed system helps to atomize the fuel mixture before it leaves the carburetor.
8. The use of an emulsion tube, offers increased design flexibility in that the tube is modified readily and the holes sizes and locations can be easily adjusted to tune the response of the carburetor to different operating conditions. Note: The ideal

carburetor would not require tuning and would provide an appropriate *AFR* under all operating conditions.

9. With an increase in bleed air flow, the two-phase mixture will experience a pressure drop much larger than that of a single phase flow for a given flow rate.

These competing effects are extremely complex and require an accurate model to adequately characterize the sensitivity of the carburetor to each of the aforementioned parameters such as main jet size, air-bleed metering orifice diameter, emulsion tube diameter, and the dimensions associated with the size and locations of the emulsion tube holes.

2.4.2 Low Speed Operation of the Idle Path System

During low speed operation, where the throttle is nearly closed, air flow through the engine is substantially decreased by the additional resistance offered by the throttle. The driving pressure difference between the throat of the venturi and the float bowl decreases to the point where eventually fuel flow through the main path ceases. In order to maintain engine operation in this low speed condition (known as the idle condition), the engine must continue to be supplied with a certain quantity of fuel (albeit a much smaller quantity than under high speed operation). The amount of fuel provided to the engine under idle conditions must be precisely metered in order to avoid wide variations in *AFR* that can alter emissions and performance at idle conditions. To achieve this control, carburetor designers typically employ a simplified version of the main path system as depicted in Figure 2.13 and in much greater detail in Figure 2.14.

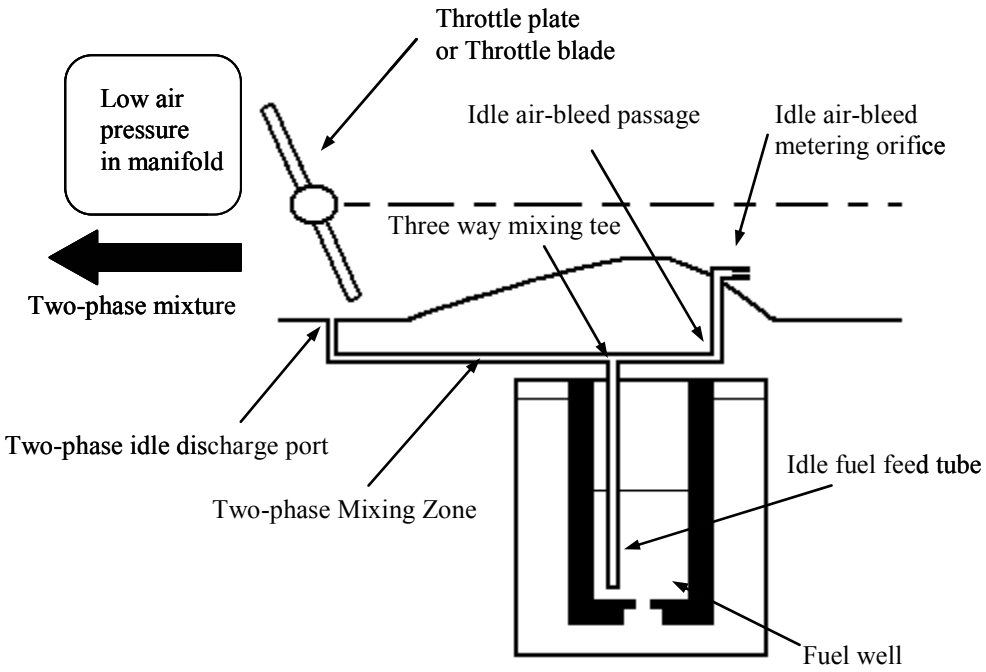

Figure 2.14: Significant features of a typical idle path found in small engine carburetors during low speed operation.

Liquid fuel, at the same pressure as that in the bottom of the fuel well, proceeds through a small idle fuel feed tube to a three way mixing tee. The idle fuel feed tube is usually sized to restrict fuel in a manner similar to that of the main jet metering orifice in the high speed circuit. At the mixing tee, air from the idle air-bleed passage mixes with the fuel. The idle air-bleed system is also equipped with a metering orifice similar in design and operation to that of the main air-bleed metering orifice. In general, use of an idle air bleed allows use of larger two-phase metering orifices because the pressure drop across the idle discharge port is reduced. The use of larger orifices eases manufacturing limitations. Downstream of the tee, the two-phase mixture proceeds and develops until it reaches the two-phase idle discharge port. This port is usually a hole drilled into the wall of the venturi. The hole size serves to act as a metering orifice to restrict the two-phase

discharge. From this point, the two-phase mixture flows through the manifold on its way to the cylinder.

The idle system is usually sized to deliver a rich mixture at idle conditions. The idle air-bleed system also looks to establish a balance between increased fuel flow due to emulsifying air and decreasing pressure potential which restricts fuel flow. Overall, fuel flow is reduced by the idle air-bleed compensation system but is still considered rich.

2.4.3 Transition from Low Speed to High Speed Operation

During transient throttle opening, engine airflow increases rapidly, but the response of the fuel delivery system is delayed due to the inertia of the fuel. This time lag is most noticeable between idle conditions and high speed operation, i.e., when the manifold pressure driving the idle system is falling and the pressure differential between the float bowl and the venturi throat is increasing. This lag in carburetor response causes a lean condition that requires fuel enrichment. Additional fuel is metered and supplied by an auxiliary system built into the idle system as shown in Figure 2.15.

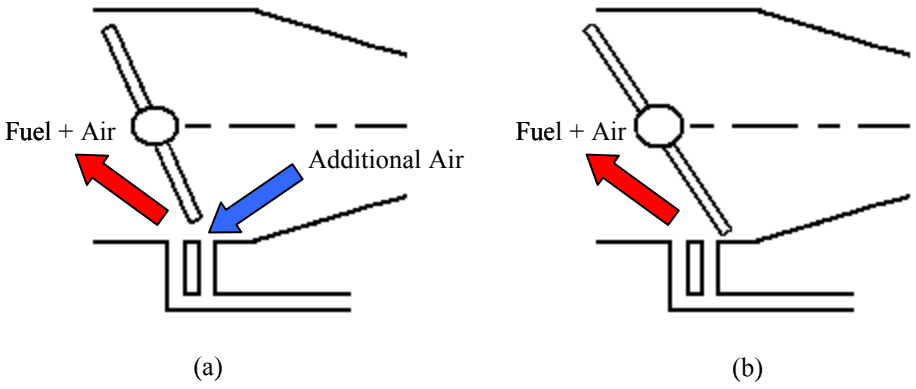

Figure 2.15: Transition system typically employed in small engine carburetors during two different throttle conditions

A mixture of fuel and air from the primary idle air-bleed proceeds down the two-phase region towards the idle port discharge area. If the carburetor is equipped with a transition system, two different events may occur based on throttle angle. If the throttle angle is small, additional air will bleed into the two-phase mixture, further decreasing the average mixture density and decreasing fuel flow. This occurs because the air pressure on the upstream side of the throttle plate in Figure 2.15(a) will be greater than the manifold air pressure on the downstream side of the throttle plate. In Figure 2.15(b), the throttle angle is increased and now the discharge holes are both exposed to the same pressure, i.e., manifold air pressure. Therefore, no additional air is bled into the system beyond the primary bleed air upstream of the venturi throat. Furthermore, the additional hole serves to increase the area of the idle discharge port, thereby decreasing the resistance to fluid flow and providing enrichment upon sudden increases in throttle angle. This additional hole compromises the transition system in a typical small engine carburetor. In general, when supplying additional bleed air, the transition system weakens the mixture strength and is thus suitable for part throttle operation where full power is not required.

Note: the schematics explained above in no way describe all variations in carburetor design. However, the carburetor geometries described above are usually the most cost effective and are thereby most typically employed by small engine manufacturers. Within the small engine community, many variations on transition system design are present. Some carburetors employ no transition system, while others employ simple holes and yet others use slots instead of holes.

From the description above, it is obvious that carburetors are very complex both in design and operation. Their control of the fuel metering process is essential in controlling emissions and performance. The next section of this review will describe models used to simulate the fuel flow process.

2.5 Fuel Flow Models

As with air flow modeling, fuel flow models exist with three distinct levels of complexity and accuracy. The first model discussed is the easiest to understand and the most common type reported in the literature. The steady state model uses steady (time averaged) values for boundary conditions. The boundary conditions include venturi mass flow rate, manifold air pressure, and upstream stagnation air pressure. The model is particularly useful for situations where the airflow through the intake tract is approximately steady, such as with multi-cylinder engines.

2.5.1 Steady State Models

One of the most thorough attempts to generate a fuel flow model of the entire carburetion process was produced by Harrington and Bolt [11]. A FORTRAN model was used to examine this system as part of a large flow network. The carburetor under consideration was of considerable complexity, incorporating numerous air bleeds for both the main system and the idle path. Two phase effects were specified by a mass weighted average density (homogeneous assumption) and liquid transport effects in the intake manifold were accounted for as well. Liquid transport effects concern droplet transport in the air stream and the flow of fuel as a film along the manifold wall. The results of the computer simulation agreed well with experiments, on average agreeing to within 5%.

Figure 2.16 shows some of the results of the compressible flow model built and the predicted fuel economy results for the same engine compared with experimental data.

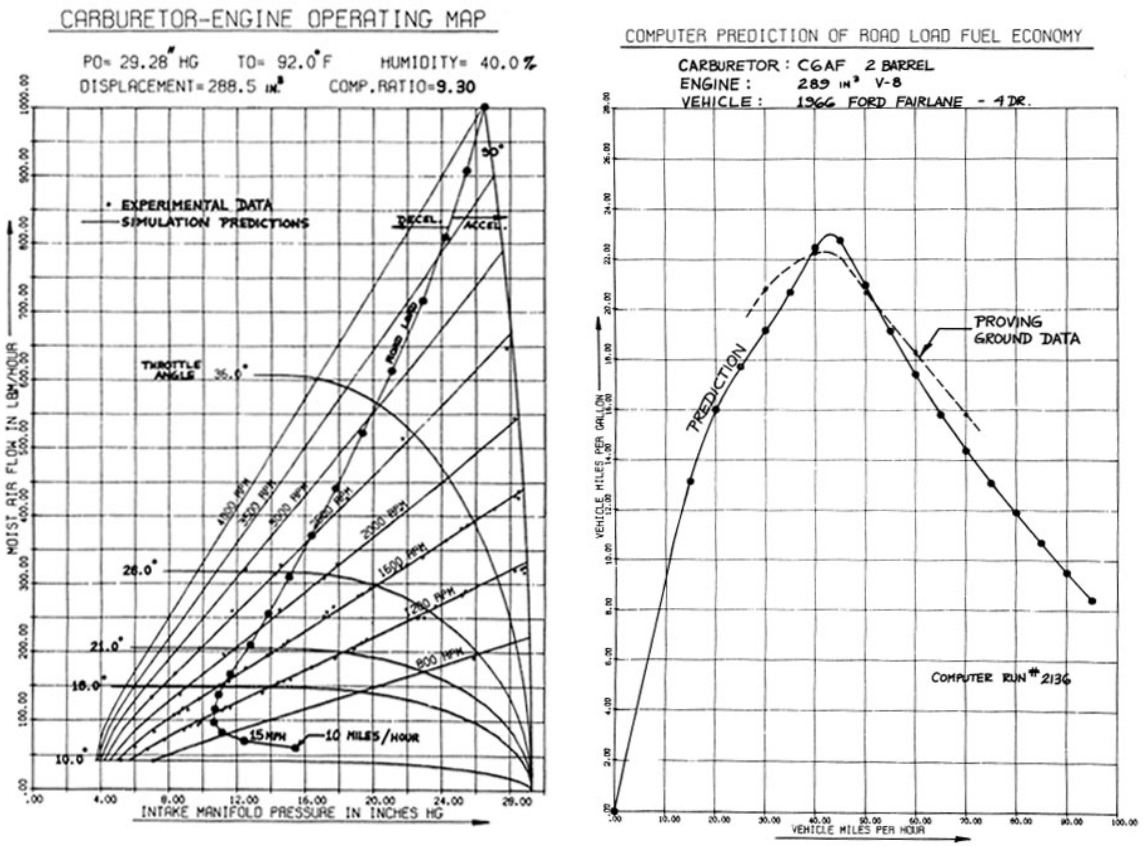

Figure 2.16: Predicted and experimental results for airflow and fuel economy in 289 in^3 engine with a 2-BBL downdraught carburetor. Reproduced from Harrington and Bolt [11].

Utilizing careful experiments to generate discharge coefficients for metering orifices, results were obtained that matched over-the-road results very well. These results give an indication of the importance of steady-state testing and the impact it can have on design.

Shinoda et al [28] took an even deeper look into some of the governing phenomena occurring in a modern carburetor, and published a similar steady state model that attempted to ascertain some of the governing effects of different geometric

parameters on fuel flow response in the transition region. Figure 2.17 illustrates the geometry examined during the course of the project along with some of the results obtained during analysis.

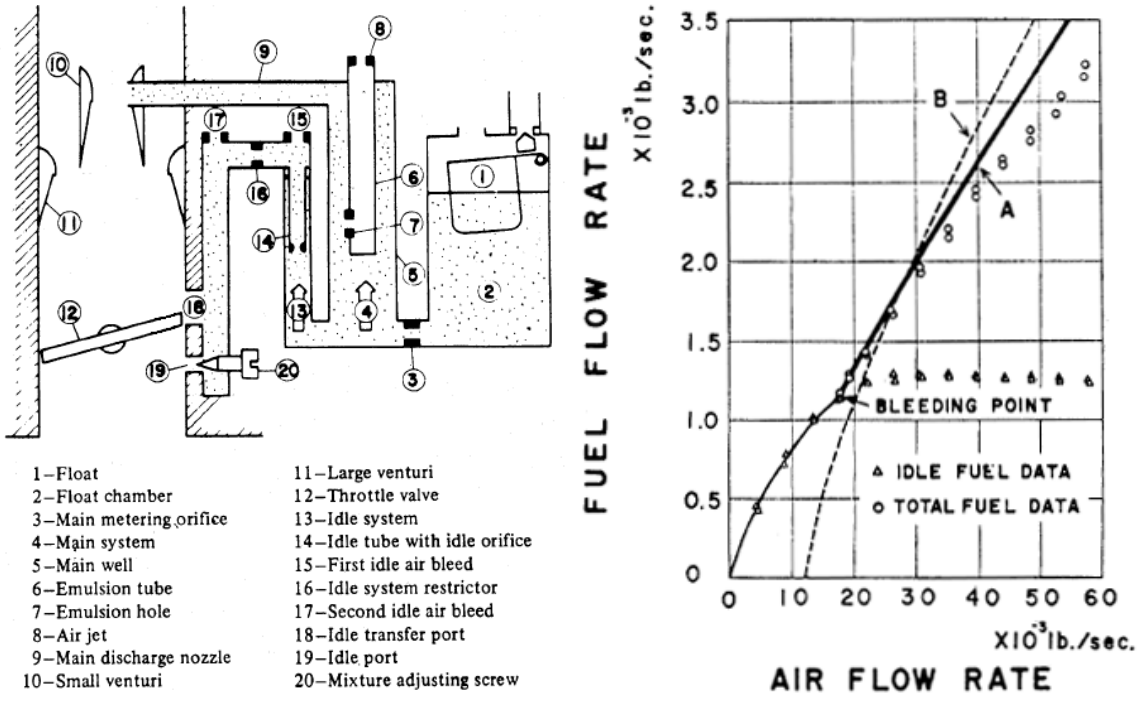

Figure 2.17: Geometric details used by Shinoda et al. [28] in their transition region metering analysis, and results obtained from steady state analysis over entire operating range.

The Figure 2.13(b) shows the fuel flow rate as a function of air flow rate and illustrates both the idle path fuel flow and the total fuel flow. Notice that when the idle system reaches its maximum delivery rate, the air-bleed system begins to turn on the main system which provides a constant increase in fuel flow that is proportional to the increase in air flow.

This analysis also relies on experimentally determined discharge coefficients in order to generate acceptable results. The authors were able to identify and understand

some of the more subtle behaviors of the air bleed system using their analysis. Specifically:

1. The transition region requires an air-bleed system to ensure a uniform air-to-fuel ratio in the transition region, i.e., the point where the main system takes over for the idle circuit.
2. Surface tension effects in the emulsion tube must be considered in a pressure drop analysis for accurate results.
3. Bleed-air decreases the average fuel density in the emulsion tube and increases fuel flow. However, this effect is balanced by an increased pressure drop in the two-phase region.

Furuyama [29,30] continued to examine air-bleed characteristics, but narrowed his focus to concentrate on the fuel supply characteristics of the idle system and, specifically, the interaction of the air-bleed system with the bypass port, identified in Figure 2.18a. The author closely examined three cases, identified in Figure 2.18b, that explain the function of the bypass port and how the response of the fuel system changes during each condition. A description of bypass port shape effects was provided as well, as detailed in Figure 2.18c.

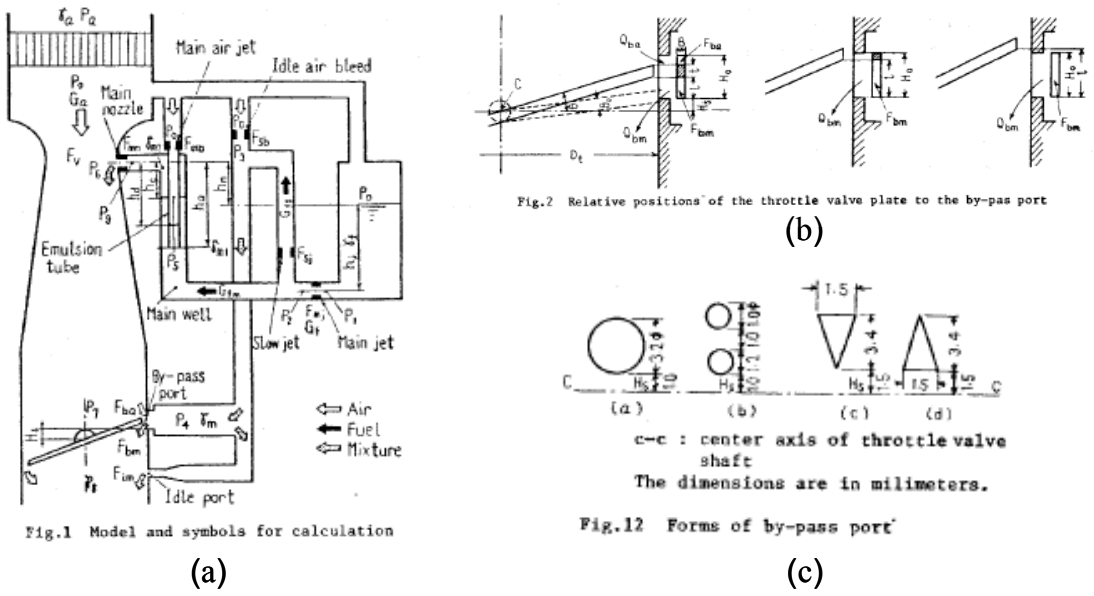

Figure 2.18: (a) Carburetor model under consideration, (b) bypass port cases examined, and (c) forms of bypass port studied. Reproduced from Furuyama [30].

Figure 2.14(a) shows that for a fixed idle jet (slow jet) size, the effective flow area formed by the edge of the throttle plate and the Venturi wall acts much like a carburetor with a variable Venturi throat size. The *AFR* of the mixture supplied will change as a function of airflow and throttle angle due to changing effective areas. The author states that this effect is somewhat compensated for by the changing air-bleed effect of the bypass port. However, Figure 2.14(b) shows the compensation effect provided by bypass air will cease once the throttle plate proceeds past the bypass port.

The different port shape geometries shown in Figure 2.14(c) has a predictable effect as long as the change in area versus the change in throttle angle can be discerned; the author notes that this is true regardless of the shape of the bypass port, whether it is a simple hole, series of holes, or a more complex shape. Note that the inverted triangular shape provides the most linear response of all the shapes tested but is obviously the most complex shape to manufacture.

Recently, Sendyka and Heydal [31] presented an analysis of a constant depression (variable venturi) carburetor that showed fuel economy gains of up to 18% compared with a conventional fixed venturi carburetor. However, their analysis did not examine air-bleed effects and their results were not compared against experimental data.

At this point it is relevant to mention that all of the previous models, no matter how detailed, encountered difficulties relating to unsteady effects experienced during actual carburetor operation. These unsteady effects, aptly named pulsation effects, will be discussed next, along with the various methods used by different authors to compensate.

2.5.2 Pulsation Effects during Actual Carburetor Operation

From the first attempt at simulating a modern carburetor it has been recognized that pulsation effects are present. Hosho [32] recognized their presence and attributed them to different flow modes set up inside the main fuel circuit during air-bleed operation.

Harrington and Bolt [11], mentioned previously, also experienced difficulty in accounting for pulsation effects. They correctly attributed the pulsation effects to corresponding intake pulses by use of a flow visualization technique to examine the fuel discharge. Their revelation calls into question their assumption of steady flow in a V8 engine, but they corrected their steady state analysis with a factor relating the amplitude and frequency of the pressure waves to engine speed.

Moss [33] eliminated the air-bleed system, and concluded that pressure pulses in the intake system contributed to unsteady effects. Moss recognized that enrichment effects become more pronounced as engine speed increases and proposed a correction to

his model in order to account for the wave form of the sinusoidal pressure pulse. However, this proved to be difficult because the shape of the pressure waveform changes with engine speed. This result indicates that all relevant unsteady phenomena were not fully accounted for; this is evident in Figure 2.15 which compares model prediction to data as a function of the pulsation factor.

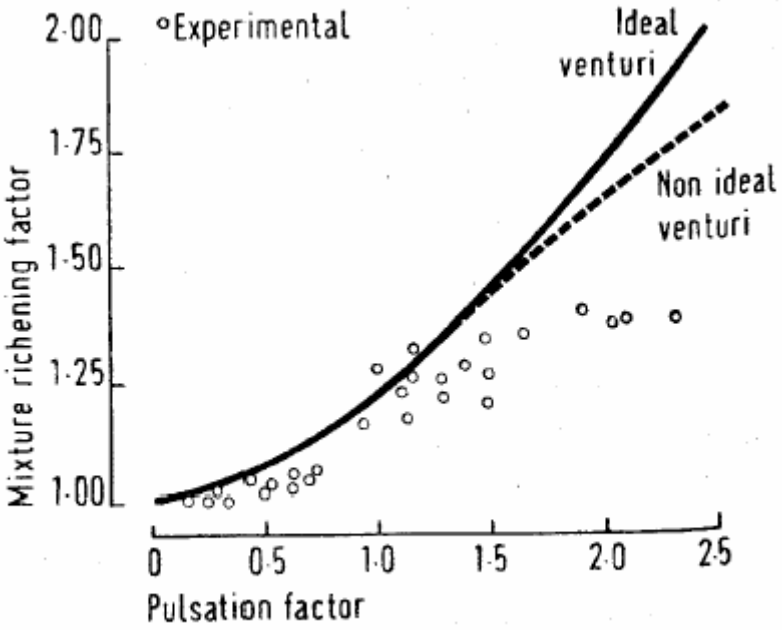

Mixture richening factors vs *pulsation factor.*

Figure 2.19: Predicted and experimental results gathered by Moss [33]. Pulsation factor is a term used to describe the amplitude of the pressure wave in the intake manifold. Mixture richening factor prescribes the additional amount of fuel delivered in terms of a factor.

The work of Moss was extended by Tanaka [34] who proposed that the length of the intake tract was primarily responsible for the pressure pulsations felt by the carburetor. Again, a frequency and amplitude correction factor was proposed to bring the steady state results into alignment with the experimental data.

The discussion above indicates that it is important that the pressure variation in the intake manifold be predicted accurately in order to correctly predict the pulsation enrichment effect.

Using an ingenious device to cyclically and controllably vary manifold pressure, Furuyama and Ohgane [35] used a carburetor equipped with an air-bleed system to provide further evidence for the ideas proposed by Moss, Tanaka, and others. Their findings can be summarized as follows:

1. At low air and fuel flow rates, the effects of pulsations are small.
2. For higher air flow rates (larger pressure variations in the intake manifold), the fuel flow rate is higher under pulsating flow than it would be for the same average air flow rate at steady flow conditions.

All of the aforementioned authors offer various suggestions for the role and impact that pressure variations have on pulsation enrichment effects. To deal with the deviation from expected results, all authors proposed a correction scheme to account for unsteady conditions. None of the researchers provide any evidence to suggest that the response of the fuel system may also be linked to the inertia of the fuel.

Derezinski [36], who advanced the work performed by Harrington and Bolt, devoted his entire study to the computer simulation of oscillatory flow in carburetor metering channels, thereby acknowledging the importance of fluid mass on response. However his study used a few limiting assumptions, with one being the assumption that the *AFR* remains constant in different branches of the flow network. Therefore, the response of the branches can be appropriately examined, but the results will not be

entirely useful because the *AFR* in a given channel does not remain constant over the duration of a cycle. Despite these handicaps, Derezinski was able to obtain satisfactory results under steady state, indicating that the depth of the analysis was sufficient. Once again, he was one of the first to suggest that pulsation effects can be partly attributed to the inertia of the different fluids moving through the carburetor.

Despite the indication that fuel inertia is important, most of the authors above assumed fuel inertia was negligible. Therefore, the authors mostly agree that the primary agent responsible for deviations from steady state must be the role of pressure variation in the intake manifold. The models discussed next attempt to account for these periodically changing boundary conditions. Since these boundary conditions change in time and since inertial effects in the fuel flow are neglected, these models are deemed quasi-steady models.

2.5.3 Quasi-Steady State Fuel Flow Models

An extension of the steady-state fuel flow model into the time domain is defined as a quasi-steady model. Extension into the time domain is accomplished using equation (2.10) which allows time varying boundary conditions for pressures to be utilized.

Hubbard [37] created a model that used a lumped mass approximation to predict the pressure variations in the intake manifold as a function of time. This approximation accounts for inertial effects in the intake system, but not acoustic effects. The author also used an electrical analogy to model inertial effects in the fuel system but due to computing power available at the time the model was simplified to the point that it is of questionable use in any carburetor design.

A modern carburetor equipped with an air-bleed system was analyzed by Szczecinski and Rychter [38] to study fuel flow response with varying pressure conditions. Instead of relying on a computer prediction for intake manifold pressure as a function of crank angle, the authors simply collected manifold pressure data from their engine and applied it to their fuel flow model in the form of a sinusoidal pressure variation. Their results agreed well with experimental data taken.

Other researchers have eliminated the collection of the experimental data and instead relied on a computer prediction for intake manifold pressure as a function of crank angle, Sendyka and Filipczyk [39] created a quasi-steady model of the engine airflow process to eliminate some of the empiricism employed by Szczecinski and Rychter. The model predicted a leaner *AFR* ratio than was measured; indicating dynamic effects were inadequately represented by the model. In a similar study, Tanaka, Sato, and Watanabe [40] also created a computer simulation to model the pressure pulsations in the intake tract. Their results also agreed well with experimental data.

Although limited by available computing power, the quasi-steady models presented represent a step forward in understanding, not only with regards to carburetion theory, but also with the effects of pulsating flows in the intake system. The next section describes unsteady models where the effects of acoustics and inertia are accounted for in the intake system. Unsteady models also account for the transient effects of fuel flow in the carburetor, which are a characteristic result of sinusoidal pressure variations applied to the boundary conditions of the carburetor.

2.5.4 Unsteady Fuel Flow Models

Other than the work performed by Derezinski and Hubbard, there have been no previous attempt to account for the transient effects of fuel flow in the carburetor have been attempted. Arias [41] recognized this deficiency and produced a model that accounted for dynamic fuel flow effects. The author derived and solved the partial differential equation that governed the unsteady fuel flow in the single phase portion of the emulsion tube, and this provided an explanation for the pulsation enrichment effects described by Moss [33] and others [32,11].

The differential equation below was solved in order to obtain the velocity of the fuel in the emulsion tube.

$$\frac{\partial u_{et,0}}{\partial t} = -\frac{1}{\rho}\frac{(P_{mj} - P_{et,0})}{L_{et,0}} + f\frac{1}{D_{et}}\frac{u_{et,0}^2}{2} - g \tag{2.18}$$

where $\frac{\partial u_{et,0}}{\partial t}$ specifies the change in velocity at the end of the single phase fuel portion of the emulsion tube over the change in time, P_{mj} represents the pressure directly after the main jet, $P_{et,0}$ represents the pressure at the end of the single phase fuel portion of the emulsion tube, $L_{et,0}$ is the length of the single phase part of the emulsion tube, f is the Darcy friction factor, D_{et} is the diameter of the emulsion tube, and g is the gravitational acceleration.

An example of the results predicted is provided in Figure 2.20, which shows the fuel flow rate as a function of crank angle (the EES-dyn curve represents the dynamic model, the EES-qss curve represents the quasi-steady model results at the same conditions).

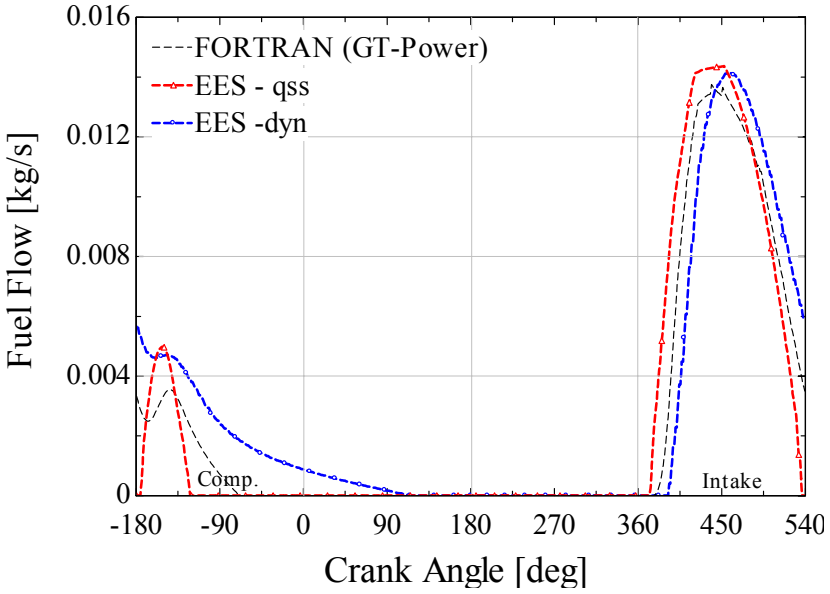

Figure 2.20: Comparison of fuel flow models implemented by Arias [41]. EES-qss represents the quasi-steady model, EES-dyn defines the results of the dynamic fuel flow model, and Fortran (GT-Power) represents a dynamic model coupled to GT-Power.

The figure displays a few interesting trends. First, the unsteady model does not reach the peak in fuel flow achieved by that of the quasi-steady model implemented in the numerical software package EES [42]. However, after IVC, the dynamic model delivers more fuel than the quasi-steady model because the inertia of the fuel extends the fuel delivery event well past the point in the cycle where the driving pressure differential falls to zero. The figure also displays the same unsteady fuel flow model as implemented in FORTRAN with application to a user-specified function coupled directly to GT-Power as detailed by Arias [43]. Note that the GT-Power results account for inertial and acoustic effects in the intake system (accounting for the difference between the original dynamic model results); by coupling the dynamic model of the carburetor with the very detailed model of the intake track all of the deficiencies associated with previous work in this area have been addressed.

Arias carried out a series of methodically designed experiments to further characterize the two-phase flow occurring in the emulsion tube instead of relying on the assumption of homogeneous flow as Harrington [11], Shinoda [28 Furuyama [29], Sendyka [31], and others have. A complete characterization of the flow regime justified the use of an algebraic momentum balance in that portion of the emulsion tube [2], and this assumption allowed use of a correlation which simplified programming while still adequately capturing the response of the system.

The homogeneous flow model just mentioned assumes that the two phases of liquid flow and gaseous air are separated from each other, and the relative velocity between the two fluids is zero. This model allows calculation of a mean density as defined by the void fraction. The mean density and void fraction are given as follows:

$$\rho_{mix} = \rho_a(1-\alpha) + \alpha\rho_f \tag{2.19}$$

$$\alpha = \frac{\frac{\dot{m}_a}{\rho_a}}{\frac{\dot{m}_a}{\rho_a} + \frac{\dot{m}_f}{\rho_f}} \tag{2.20}$$

where ρ_{mix} defines the two-phase mixture density, ρ_a identifies the air density, ρ_f represents the fuel density, α defines the void fraction, $\dot{m}_a$ represents the mass air flow rate of the bleed air, and $\dot{m}_f$ defines the fuel flow rate of the tube under consideration.

Use of the homogeneous model is accepted in practice, but better predictions can be made with models designed for specific use with air and fuel under the conditions common in a small engine carburetor. A review of the two-phase models currently used in small engine carburetors is detailed next.

2.6 Two-phase Flow Models in Tubes and Orifices

Any modern carburetor using an air-bleed system will produce a two-phase flow that proceeds along straight tubes and eventually exits to the engine air stream at the carburetor venturi throat. A description of the homogeneous model was given above and can be used to describe two-phase pipe flow and two-phase discharge through metering orifices. Specifically, the homogeneous model allows for the calculation of a mean density, viscosity, and velocity, which in turn can be used to prescribe a friction factor to the flow. This friction factor can in turn be used to calculate pressure drop due to shear along the wall. Alternately, the two-phase velocity, viscosity, and area of the metering orifice can be used to determine expansion and contraction losses at pipe exits and entrances respectively.

2.6.1 Two-Phase Flow in Tubes

It has been observed that the flow pattern established in emulsion tubes varies depending on a host of parameters such as emulsion tube diameter, emulsion tube length, hole size, fluid densities, etc. Oya [44,45] conducted visualization experiments to determine the flow regime map where carburetors are most likely to operate. The author produced a series of correlations to determine pressure drop based on the type of flow pattern present. Although insightful, determining which correlation to use, and under what conditions it should be applied, is not a simple task due to complicated nature of the flow regime map as presented in Figure 2.21. The map is based on the superficial velocities of the gas and liquid present in the two-phase flow. Superficial velocity is defined as the volumetric flow rate of a single phase divided by the area of the pipe.

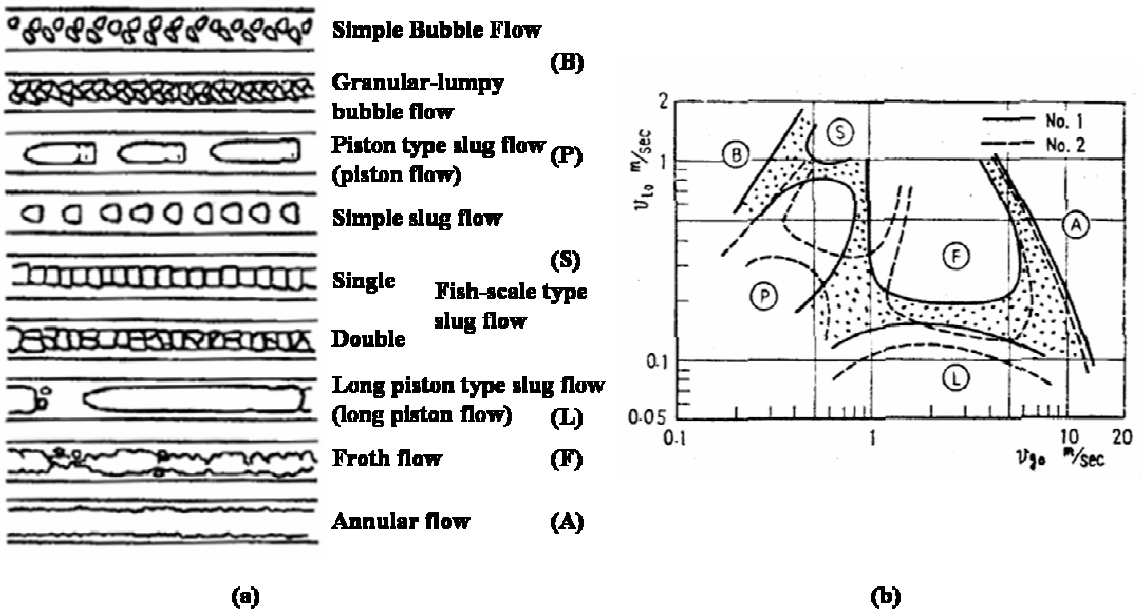

Figure 2.21: Flow patterns and flow regime map for different conditions. Reproduced from Oya [44,45].

Figure 2.21a indicates the flow patterns typical in two-phase passages of small engine carburetors. The map in Figure 2.21b indicates the regions where each type of flow regime occurs. The shaded regions indicate uncertainty about where one regime ends and another begins.

Arias [41], as mentioned previously, developed a correlation that was independent of operating condition and therefore could be implemented over a wide of conditions. Figure 2.22 shows the predicted and measured pressure drop for a range of operating conditions and three different tube sizes. Notice that the correlation developed by Arias becomes much less accurate when applied to passages that are smaller than 5 mm. In the typical idle path found in a carburetor, most passages are smaller than 5 mm and therefore the correlation is not appropriate.

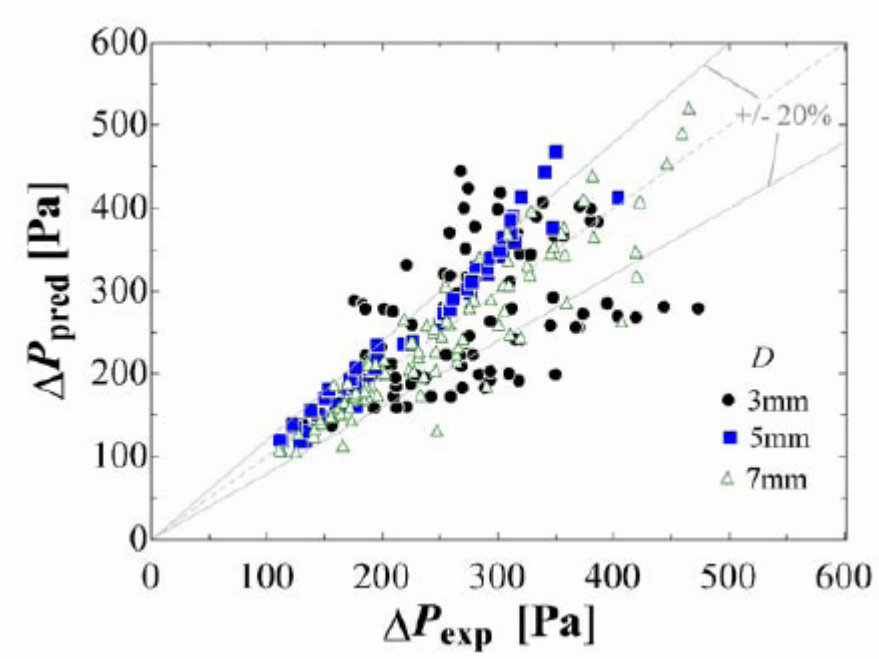

Figure 2.22: Pressure drop predicted by correlation developed versus measured pressure drop. From Arias [41].

2.6.2 Two-phase Flow through Metering Orifices

At the two-phase idle discharge port, the fuel and air mixture passes through a restriction which serves as a metering device; this was illustrated in Figure 2.14. The pressure drop associated with the two phase mixture as it passes through a metering orifice is therefore an important aspect of any model of a carburetor. Chisholm [46,47] has developed semi-empirical correlations to calculate pressure drop based on the Lockhart-Martinelli correlating parameter [48]. This model should be applicable to flows involving mixtures of fuel and air, since no information was given about constraints placed on the fluids modeled, however, most of the early two-phase literature is used for refrigerant flows and thus caution must be exercised when applying these models to two-phase flows in carburetors. These models could also be used to describe the pressure loss

due to expansion of the two-phase mixture into the engine manifold from the idle discharge port.

2.7 Multiphase Transport Effects

The previous sections summarized the literature available relative to engine air flow rate, carburetor fuel flow rate, and modeling two-phase mixtures has been discussed. In this section a short discussion of the physics of liquid fuel and droplet transport that occur in the intake manifold will be discussed.

Lenz [49], Harrington [11], and Ehara [50] have all observed a decrease in static pressure at the throat of the Venturi with increasing fuel flow. They reasoned that the presence of the fuel requires additional energy from the airflow to accelerate the fuel to the velocity of the air stream. Secondly, the authors agreed that the fuel requires additional energy to further atomize, and this also decreases the static pressure at the throat. Therefore, the conclusion can be made that although these effects are small in terms of their impact of *AFR*, they are important in describing the performance of a given engine/ carburetor combination and understanding the complete picture behind fuel delivery from a carburetor to the combustion chamber.

Along with droplets, liquid films are also present in the intake manifold. The effects of liquid films on emissions and performance have been detailed by many authors in the literature, such as Lenz [49], Jehlik and Ghandhi [51], Chen [52], and many others.

This study is concerned with the mixture preparation inside the carburetor only, and therefore for the remainder of this document, the effects of liquid films and fuel droplets, and their impact on delivered *AFR* will be ignored. However, in the general

design of engines, the effects of fuel transport in the manifold should not be readily neglected.

2.8 Summary of Literature Review

The literature review highlighted several areas where understanding regarding air, fuel, and two-phase flows could be improved. These opportunities are summarized here:

1. Previous dynamic models have focused almost exclusively on *AFR* prediction during main path system operation with little attention given to the idle and transition paths. Furthermore, these studies tended to neglect fuel inertia. Therefore an opportunity exists to study the effects of fuel inertia on idle and transition systems.
2. The transient operation of small engines is characterized by sudden changes in throttle angle which creates a dynamic response in the air bleed system. An in-depth study of the flow patterns created in the bypass port and the identification of the best method to characterize the system response to these changes would improve the current understanding of the transition between the main and idle metering systems.
3. Studies have been conducted on two-phase flow during operating conditions encountered in small engines; however, the correlations that have resulted are limited in terms of the applicability, specifically the tube size. Any new attempts at characterizing the developing two-phase fuel and air flow should focus on passage sizes that are smaller than 5 mm in diameter
4. No previous work has been carried out which examines the fuel and air flow in two-phase metering orifices found in typical idle path discharge ports. Since

theoretical models are difficult to apply, a wide range of experiments could be carried out in order to better understand these flows.

5. The coupled solution of the fuel and air flow in 1-D engine simulation software has been performed; however, this work excludes the idle and transition path. The development of a simulation tool that considers all of the circuits found in modern small engine carburetors would greatly aid the design and development process undertaken for new carburetor applications.

Chapter 3

Carburetor Model

This chapter will discuss the development of a theoretical model that is capable of predicting the fuel and air flow rate in the idle and transition path of a small engine carburetor with geometry that is similar to what was described in the previous chapter (e.g., see Figures 2.12-2.14). The model captures the dynamic fuel flow effects in the idle path using lumped inertial, capacitive and resistive elements. The model incorporates a correlation developed as part of this work which captures expansion losses at the two-phase idle path discharge orifice. The model was implemented in MATLAB in order to facilitate parametric studies and simplify the solution of the stiff system of equations that result when trying to compute fuel and air flow rates that are small compared to the pressures they occur in. Finally, a modified model of the main path is presented which is substantially simplified relative to the work of Arias et al [41] and therefore improves the computational speed and reliability of the solution.

3.1 Electrical Analog Description of the Idle Path

There are essentially an infinite number of idle path configurations that can be considered during the design of a carburetor; within each configuration, the geometry of each component can be varied. The modeling methodology that is described here is presented in the context of a specific configuration and geometry that is consistent with the idle path found in the Briggs and Stratton Intek (BSI) engine carburetor; however, the methodology is robust and can be applied to essentially any configuration or geometry without modification of the approach. Furthermore, the protocol of the simulation and its

structure is consistent with the engine simulation program GT-Power which will facilitate the integration of the model with this software.

Figure 2.13, repeated here for convenience as Figure 3.1, describes the current geometry considered and the conditions under which it operates.

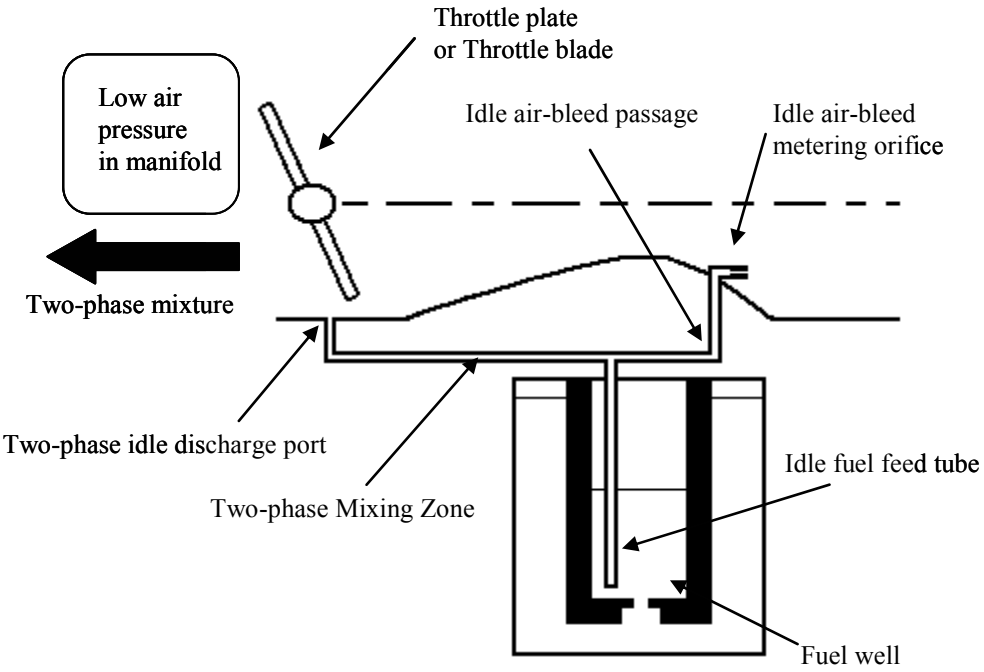

Figure 3.1: Idle path geometry of the Briggs & Stratton Intek carburetor

The idle path configuration consists of resistive elements that represent the single-phase air and two-phase sections (R_{ap} and R_{tp1}) and a resistive and inertial element that together represent the single-phase fuel section (R_{fi} and In_{fi}). The pressures that bound the idle path network include the pressure upstream of the Venturi ($P_{up,v}$), the pressure at the manifold (P_{man}), and the pressure in the fuel well after the main jet (P_{mj}). A detailed discussion of the methods that are used to calculate the boundary conditions will be presented in Section 3.7; however, the model will converge for any values of these boundary conditions. The fluid dynamic elements that make up the idle path are well represented by an electrical analogy, as shown in Figure 3.2.

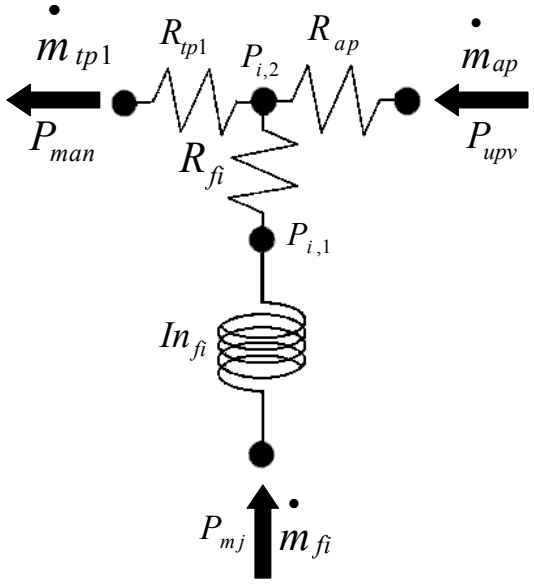

Figure 3.2: Electrical analogy of the current idle path with fluid flows and boundary conditions indicated.

Figure 3.2 describes the following process: A fuel mass flow rate, defined as $\dot{m}_{fi}$, is driven by the pressure after the main jet (P_{mj}) up the idle fuel feed tube. At the mixing junction, it encounters air at a mass flow rate $\dot{m}_{ap}$ which is driven by the pressure at the idle air-bleed ($P_{up,v}$). The two-phase mixture, defined as $\dot{m}_{tp1}$, proceeds down the two-phase mixing zone and empties into the engine air stream at the manifold pressure (P_{man}).

Alternative idle path configurations can also be considered using the modeling methodology described here. For example, many carburetors provide for transition conditions with discharge holes that are exposed to various pressures near the throttle plate and a final discharge hole that is located under the throttle plate. The schematic of this alternative idle path configuration is shown in Figure 3.3 for a transition system that

includes one additional discharge hole which provides additional bleed air to the idle system.

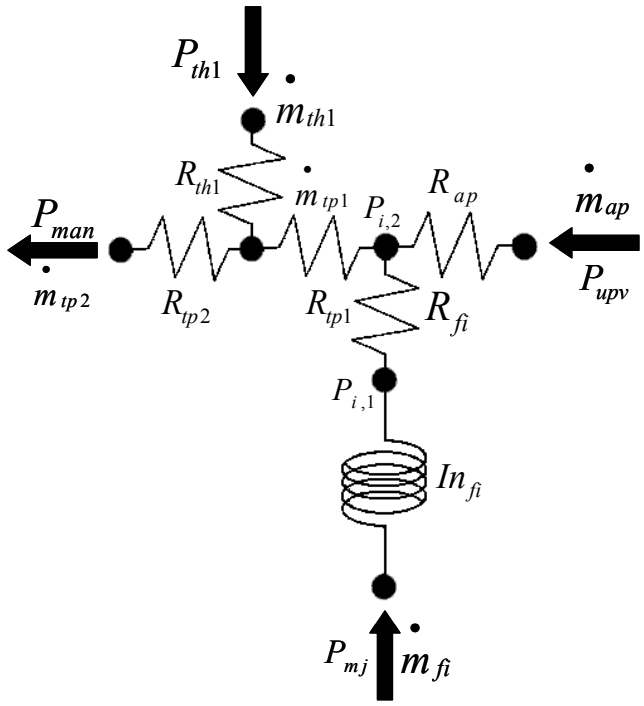

Figure 3.3: Alternative idle path configuration displaying a simple transition system.

The process described previously remains the same for the alternative system shown in Figure 3.2 except that the two-phase mixture ($\dot{m}_{tp1}$) emanating from the mixing junction will subsequently mix with additional bleed air from the transition hole ($\dot{m}_{th1}$) and become a slightly different fuel-air mixture ($\dot{m}_{tp2}$) which is discharged at the manifold pressure (P_{man}). It is possible for fuel and air to discharge from the transition under certain conditions. This occurs when the throttle plate uncovers the transition hole. In the simulation, the air flow is not allowed to cease but instead takes on a small finite value. The area of the primary discharge hole then increases to account for the decrease in resistance of the discharge system.

Clearly there are a large number of configurations that could be considered within each idle path configuration corresponding to additional constrictions, tubes, etc.; all of these configurations can be accommodated by altering the resistance network representation of the fluid dynamic elements.

The quantities that are required to characterize the configuration shown in Figure 3.1 are listed in Table 1; the nominal values for these quantities that are associated with the BSI carburetor are also provided in Table 1. The MATLAB file used to assign these quantities is contained in Appendix A.1.

Table 3.1: BSI characteristics for carburetor idle path studied

Symbol	Description	BSI Value
$n_{tp,1}$	number of two- phase (2-Φ) discharge holes	1 [-]
$D_{tp,o}$	diameter of discharge holes	0.00053[m]
$Cd_{tp,o}$	discharge coefficient characterizing 2-Φ holes at discharge point	0.8 [-]
D_{tp1}	diameter of 2-Φ section leading from mixing chamber	0.0016 [m]
L_{tp1}	length of 2-Φ section leading from mixing chamber	0.023 [m]
k_{tp1}	roughness in 2-Φ section	0.00001 [m]
C_{dap}	discharge coefficient of single phase air section	0.8 [-]
k_{ap}	roughness in air section	0.00001 [m]
L_{ap}	length of air section	0.127 [m]
D_{ap}	diameter of air section	0.0023 [m]
$Cd_{ap,o}$	discharge coefficient of orifice connecting air to mixing zone	0.8 [-]
$D_{ap,o}$	diameter of orifice connecting air to mixing zone	0.000838 [m]
D_{fi}	diameter of first single phase fuel section	0.000889 [m]
L_{fi}	length of first fuel section	0.0215 [m]
k_{fi}	roughness of first fuel section	0.00001[m]

3.2 Idle Path Model Structure

Figure 3.4 illustrates the structure of the idle path model. The details associated with each function that makes up the idle path model may change as different idle path configurations and geometric configurations are considered; however, the basic structure will remain the same. The `idlepath` program must be directly integrated with a larger, system-level simulation in order to be useful. Therefore, the idle path model must

receive information about the current state of the system as inputs (e.g., mass flow rates) and current operating conditions (e.g., pressures at the terminals of the carburetor) as well as all information that is necessary to specify the characteristics of the idle path and the size of the system timestep that must be simulated (Δt).

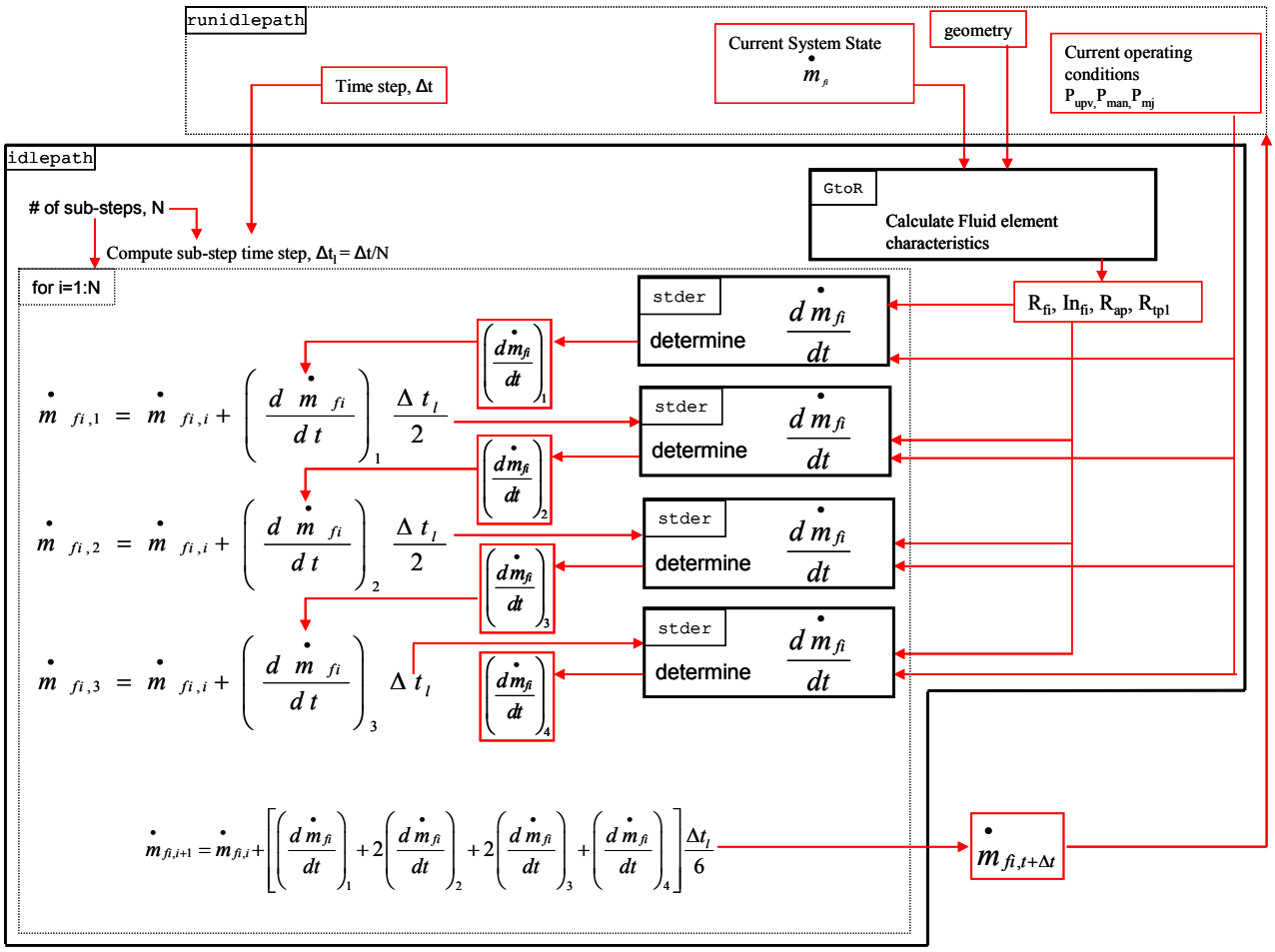

Figure 3.4: Structure of the idle path model

For the current idle path configuration, the operating conditions that must be provided include the pressures at the inlet to the single-phase air section ($P_{up,v}$, corresponding to the pressure upstream of the Venturi throat), at the inlet to the single-phase fuel section (P_{mj}, corresponding to the fuel well pressure), and at the exit to the two-phase section (P_{man}, corresponding to the manifold pressure). The system state

includes the instantaneous value of the mass flow rate of fuel ($\dot{m}_{fi}$) and air ($\dot{m}_{ap}$) that are passing through the idle path. The geometry information is provided in the form of a single array (`geometry`) that is constructed based on the characteristics of the idle path. This information must be provided by the calling program.

Returning to Fig. 3.4, the first step in the solution process is to evaluate the fluid element characteristics based on the geometry and instantaneous operating conditions. The fluid element characteristics include the three resistances, R_{ap}, R_{fi}, and R_{tp1} and the fuel inertia In_{fi}, as indicated in Fig. 3.2. This mapping of geometry and operating condition to fluid element characteristics is accomplished within the function `GtoR`. Within the function `GtoR`, the geometric configuration is identified and the information in `geometry` is interpreted in the context of the current conditions. This process is discussed in Section 3.3.

The fluid element characteristics are returned to the `idlepath` routine. The timestep specified by the system model (Δt) is broken into N sub-steps (Δt_l) as required in order to accurately simulate the potentially high frequency dynamics that characterize the idle path. The fluid element characteristics are sufficient to determine the derivative of the state variables within the idle path; this process occurs in the function `stder`. For example, the current configuration of the idle path contains only one energy storage component, represented by the fuel inertia. The state variable that characterizes the energy stored in the inductor is the mass flow rate through the inertial component. Therefore, the function `stder` computes the rate of change of the fuel mass flow rate; this process is discussed in Section 3.4. The rates of change of the state variables are integrated through the substep using a Runge-Kutta 4th order (RK4) technique in order to

determine the value of the state variable (and any other variables of interest) at the end of the substep(Δt_l); this process is repeated until the entire timestep is complete. This integration process is discussed in Section 3.5. The result of the simulation process are the predicted mass flow rates at the end of the system timestep ($\dot{m}_{fi,t+\Delta t}, \dot{m}_{ap,t+\Delta t}$) which are returned to the system simulation. The process, implemented using pressure information that is consistent with the Briggs and Stratton Intek Engine operating at a specific throttle position and engine speed, is presented in Section 3.6. Section 3.8 provides a parametric investigation of these results.

3.3 Calculation of the Fluid Element Characteristics

The function `GtoR` uses the geometry associated with a particular idle configuration/geometric configuration permutation in the context of the instantaneous operating conditions in order to determine the resistance, inertia and (if necessary) capacitance values that characterize the idle path. In this section, the details of this calculation are provided in the context of a carburetor with the geometric characteristics and configuration shown in Fig. 2.13). The MATLAB code `GtoR.m` is contained as Appendix A.2. However, the methodology is general and the process for alternative configurations or geometries should be clear based on this presentation.

3.3.1 Single Phase Air Section

The process of estimating a fluid resistance consists of using the instantaneous mass flow rate to determine the pressure drop across the section; the ratio of the pressure drop and mass flow rate is the resistance. The velocity of the air within the single-phase air section (v_{ap}) is

$$v_{ap} = \frac{4\dot{m}_{ap}}{\rho_{ap}\pi D_{ap}^2} \tag{3.1}$$

where ρ_{ap} is the density of air and D_{ap} is the diameter of the single-phase air section. Note that a nominal air density of 1.1 kg/m^3 is used for simplicity in these calculations, the inlet system density could also be taken from a GT-Power simulation and used as an input. Also note that the mass flow rate of the air ($\dot{m}_{ap}$) used for the resistance calculations is not allowed to go below a minimum value (0.1 g/s) in order to prevent singularities in the resistance calculations. The Reynolds number associated with the air flow within the passage (Re_{ap}) is

$$Re_{ap} = \frac{\rho_{ap} v_{ap} D_{ap}}{\mu_{ap}} \tag{3.2}$$

where μ_{ap} is the viscosity of air, which is also assumed to be constant (1.9E-5 Pa-s). The friction factor is calculated based on the Reynolds number according to Cengel [53] which states that the equation for the friction factor is

$$f_{ap} = \frac{64}{Re_{ap}} \tag{3.3}$$

for Reynolds numbers < 3000. Shah and London [54] provide a correlation to account for entrance length effects. The correlation calculates an entrance length and then produces a friction factor that accounts for developing flow in the laminar flow regime. The three equations used to calculate entrance effects are listed in equations 3.4, 3.5, and 3.6.

$$x_{ent} = \frac{L_{ap} / D_{ap}}{\mathrm{Re}_{ap}} \tag{3.4}$$

$$f_{ap,dev} = \frac{3.44}{\sqrt{x_{ent}}} + \left(\frac{1.25}{4x_{ent}} + 16 - \frac{3.44 / \sqrt{x_{ent}}}{1 + \frac{0.00021}{x_{ent}^{\,2}}} \right) \tag{3.5}$$

$$f_{ap} = \frac{4 f_{ap,dev}}{\mathrm{Re}_{ap}} \tag{3.6}$$

where x_{ent} is the hydrodynamic entrance length $f_{ap,dev}$ is the friction factor for developing flow, and f_{ap} is the friction factor correlation applied to circular ducts.

When applied, laminar flow entrance effects produced a negligible difference of less than 0.75% in the integrated *AFR* (when applied to liquid, air, and two-phase pipe sections). Therefore, for simplicity, the assumption is made that fully developed pipe flow is occurring in the laminar flow regime for all circular channels in the idle path. When the Re > 3000, the flow is assumed to transition to the turbulent flow regime. The friction factor in fully developed turbulent flow is calculated from equation 3.7.

$$f_{ap} = \left[0.790 \ln\left(Re_{ap} \right) - 1.64 \right]^{-2} \tag{3.7}$$

for Re >3000. Entrance effects in the turbulent regime are assumed negligible for the most part, but can be estimated based on a correlation created by Hausen and presented by Rohsenow et al [55]. The equation used to model turbulent entrance effects is provided in equation 3.8.

$$f_{ap} = f_{fd} \left(1 + \frac{1}{L_{ap} / D_{ap}} \right)^{0.7} \tag{3.8}$$

where f_{fd} is the fully developed turbulent friction factor designated as f_{ap} in equation 3.7. The effect of the turbulent entrance length when applied to all pipes in the idle path was less than 0.1% and therefore the assumption is made that when the Re > 3000 fully developed turbulent flow exists.

The total pressure loss in the single-phase air section (Δp_a) is

$$\Delta p_{ap} = \frac{\rho_{ap} v_{ap}^{\ 2}}{2}\left(f_{ap}\frac{L_{ap}}{D_{ap}} + Cd_{ap} + Cd_{ap,o}\frac{D_{ap}^2}{D_{ap,o}^2}\right) \tag{3.9}$$

where Cd_{ap} and $Cd_{ap,o}$ represent the discharge coefficients associated with main air bleed tube and the air bleed orifice, respectively, L_{ap} is the length of the single-phase air section, and $D_{ap,o}$ is the diameter of the orifice that feeds to the primary mixing chamber. Note that all variables with the subscript $_{ap}$ indicate association with the primary idle path air bleed and all variables using the subscript $_{ap,o}$ indicate variables in the air section orifice that feeds the primary mixing chamber. Equation (3.10) shows that the pressure loss is based on three components. The first component calculates the frictional resistance while the remaining terms are related to the inertial losses that occur as the air is constricted to enter the single-phase air section and constricted again to pass through the orifice.

The ratio of the total pressure drop across the air section to the mass flow rate is the resistance of the air section

$$R_{ap} = \frac{\Delta P_{ap}}{\dot{m}_{ap}} \tag{3.11}$$

In order to prevent convergence problems that would otherwise occur at very low values of the air mass flow rate due to the mass flow rate term in the denominator, the

friction factor is not allowed to go above 0.64 if the Reynolds number drops below 100. The parametric study conducted in Section 3.7 will address the sensitivity of the model predictions to the specific friction factor correlation that is used.

3.3.2 Single-Phase Fuel Section

The single-phase fuel section is characterized by a resistance and an inertial term. As with the single-phase air section, the resistance is calculated as the ratio of pressure drop to mass flow rate. In the single-phase fuel section the resistance (R_{fi}) is

$$R_{fi} = \frac{\Delta P_{fi}}{\dot{m}_{fi}} \tag{3.12}$$

The velocity of the fuel in the first section of the single-phase fuel line (v_{fi}) is

$$v_{fi} = \frac{4\dot{m}_{fi}}{\rho_f \pi D_{fi}^2} \tag{3.13}$$

where ρ_f is the density of the fuel (assumed to be constant at 769 kg/m^3) and D_{fi} is the diameter of the first single-phase fuel section. The lower allowable limit of fuel mass flow rate is 0.1 g/s in order to avoid convergence problems at very low Reynolds number. The Reynolds number of the fuel flow in the single-phase section (Re_{fi}) is

$$Re_{fi} = \frac{\rho_f v_{fi} D_{fi}}{\mu_f} \tag{3.14}$$

where μ_i is the dynamic viscosity of the fuel (assumed to be constant and equal to 0.00058 Pa-s). The friction factor in the first single-phase section (f_{fi}) is based on Reynolds number and is defined as

$$f_{fi} = \frac{64}{Re_{fi}} \tag{3.15}$$

for Re < 3000. Once again, according to the analysis in Section 3.3.1, entrance are negligible in both the laminar and turbulent regimes in all pipes in the idle path including the single phase fuel section. For turbulent flow the friction factor is given as:

$$f_{fi} = (0.790 \ln(Re_{fi}) - 1.64)^2 \tag{3.16}$$

for Re > 3000.

The total pressure loss across the first section of the single phase region (ΔP_{fi}) is:

$$\Delta P_{fi} = \frac{\rho_f v_{fi}^2}{2} f_{fi} \frac{L_{fi}}{D_{fi}} \tag{3.17}$$

A similar process is used to compute the pressure drop across any other remaining elements in the single–phase fuel path which are connected in series. For example if the single phase fuel path included two straight sections of different lengths and diameters as well as a metering valve separating the two sections, then the total pressure loss would be computed as:

$$\Delta P_{fi} = \frac{\rho_{f,1} v_{fi,1}^2}{2}(f_{fi,1} \frac{L_{fi,1}}{D_{fi,1}}) + \frac{\rho_{f,v} v_{fi,v}^2}{2}(Cd_{fi,v}) + \frac{\rho_{fi,2} v_{fi,2}^2}{2}(f_{fi,2} \frac{L_{fi,2}}{D_{fi,2}}) \tag{3.13}$$

where the subscripts *1*, *v*, and *2* and represent variables in the first single-phase fuel section, in the metering valve region, and in the second single-phase fuel section, respectively. This gives an indication of the ease with which small geometry changes can be incorporated into the model. Now, the total resistance of the single-phase fuel element is therefore

$$R_{fi} = \frac{\Delta P_{fi}}{\dot{m}_{fi}} \tag{3.14}$$

The inertia associated with the single-phase fuel path (In_{fi}) is

$$In_{fi} = \frac{L_{fi}}{A_{fi}} \tag{3.15}$$

where L_{fi} is the length of the single-phase fuel section and A_{fi} is the area of the single-phase fuel section associated with its inner diameter (D_{fi}). The inertia of the fuel increases the pressure drop according to

$$\Delta P_{in,fi} = In_{fi} \frac{d\dot{m}_{fi}}{dt} \tag{3.16}$$

where $\frac{d\dot{m}_{fi}}{dt}$ is the rate of change in the fuel flow. Therefore, the inertial pressure drop ($\Delta P_{in,fi}$) does not influence the resistance of the fuel section but does influence the pressure drop across the resistive element and therefore affects the fuel flow response curve.

Returning to the hypothetical example mentioned above, if the single phase fuel section contained an additional length of tube then the inertial term could be represented by a single element where the total inertia is the sum of the first and second sections

$$In_{fi} = \frac{L_{fi,1}}{A_{fi,1}} + \frac{L_{fi,2}}{A_{fi,2}} \tag{3.17}$$

Here $L_{fi,2}$ is the length of the second single-phase element and $A_{fi,2}$ is the area of formed by the second single-phase element of diameter $D_{fi,2}$.

3.3.3 Two-Phase Section

Computing the resistance to two-phase flow requires knowledge of the fuel and air mass flow rates that are passing through this resistive element; the two-phase pressure drop is strongly dependent on the relative amount of liquid fuel and air and therefore the problem is highly non-linear over any time-scale other than a very small time step.

The fuel and air combine in the mixing chamber and proceed through the two-phase resistive element to the throttle discharge port. A homogeneous flow model of the two-phase region is used; the homogeneous model assumes that the two-phases are uniformly mixed and therefore intensive property information can be obtained based on weighting the properties of the intensive properties of the individual phases using the void fraction (α). The void fraction is the ratio of the volumetric flow rate of air to the total volumetric flow rate, calculated according to equation (2.18) and repeated here

$$\alpha = \frac{\frac{\dot{m}_{ap}}{\rho_{ap}}}{\frac{\dot{m}_{ap}}{\rho_{ap}} + \frac{\dot{m}_{fi}}{\rho_f}} \tag{3.18}$$

Note that Arias [2] showed that the use of a homogeneous void fraction does not generally apply to the two-phase flows produced by small engine carburetors in the main path circuit. However, the correlation produced by Arias for emulsion tubes is also not appropriate because it is invalid for tubes smaller than 5 mm, and most idle path systems incorporate tubes much smaller than 5 mm and are not always oriented vertically. Therefore, in the absence of other correlations, the homogeneous void fraction model is used and the parametric study presented subsequently will show that the error resulting from this assumption is negligible for the specific baseline conditions considered here.

With knowledge of the void fraction, the density (ρ_{tp1}) and viscosity (μ_{tp1}) of the two-phase mixture can be computed using the void fraction

$$\rho_{tp1} = \alpha\rho_{ap} + (1-\alpha)\rho_f \tag{3.19}$$

$$\mu_{tp1} = \alpha\mu_{ap} + (1-\alpha)\mu_f \tag{3.20}$$

The two-phase aggregate density and viscosity allow the calculation of the Reynolds number in the two-phase section (Re_{tp1})

$$Re_{tp1} = \frac{\rho_{tp1} v_{tp1} D_{tp1}}{\mu_{tp1}} \tag{3.21}$$

where D_{tp1} is the diameter of the two-phase section and v_{tp1} is the velocity of the homogeneous mixture

$$v_{tp1} = \frac{\dot{m}_{tp1}}{\rho_{tp1} A_{tp1}} \tag{3.22}$$

where A_{tp1} is the area associated with the two-phase diameter, D_{tp1}. The two-phase mass flow rate ($\dot{m}_{tp1}$) is, by continuity

$$\dot{m}_{tp1} = \dot{m}_{ap} + \dot{m}_{fi} \tag{3.23}$$

The homogeneous model assumes the velocities of each individual phase are equal. The Reynolds number can be utilized to calculate the friction factor which has the following form

$$f_{tp1} = \frac{64}{Re_{tp1}} \tag{3.24}$$

for Re < 3000, and

$$f_{tp1} = (0.790 \ln (Re_{tp1}) - 1.64)^{-2} \tag{3.25}$$

for Re > 3000.

The two-phase friction factor can be used to calculate the pressure drop across the two-phase resistor. The pressure drop for the two-phase section (ΔP_{tp1}) according to

$$\Delta P_{tp1} = \frac{\rho_{tp1} v_{tp1}^2}{2} \left(k_{tp1} + f_{tp1} \left(\frac{L_{tp1}}{D_{tp1}} \right) \right) \tag{3.26}$$

where k_{tp1} represents the two-phase loss coefficient associated with the sudden expansion into the intake manifold that occurs below the throttle plate, and L_{tp1} is the length of the two-phase section. The resistance of the two-phase section is

$$R_{tp1} = \frac{\Delta P_{tp1}}{\dot{m}_{tp1}} \tag{3.27}$$

3.4 Calculation of the State Variable Derivatives

The fluid dynamic system was shown schematically in Fig. 2.13 and repeated in Fig. 3.1 for convenience. The dynamic system is first order because there is a single energy storage element (the inertia of the fuel). In order to integrate the dynamic behavior of the system forward through time, it is necessary to obtain a solution for the time rate of change of the mass flow rate in the inertia. This can be accomplished using a circuit analysis.

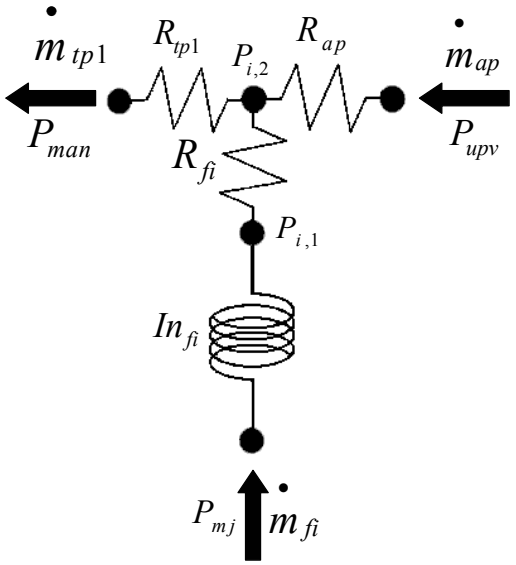

Figure 3.5: Schematic of idle path configuration with intermediate values

The constitutive equation for the single-phase air resistance is:

$$P_{up,v} - P_{i,2} = \dot{m}_{ap} R_{ap} \tag{3.28}$$

where $P_{i,2}$ is the pressure in the mixing zone. The constitutive equation for the single-phase fuel resistance is

$$P_{i,1} - P_{i,2} = \dot{m}_{fi} R_{fi} \tag{3.29}$$

where $P_{i,1}$ is the pressure separating the inertia and resistance of the fuel section. Note that this is a fictitious pressure in the sense that the inertia and resistance characteristics of the section are distributed and not truly separated, as shown in Fig. 3.5, but rather distributed. However, the separation of these behaviors into distinct elements is a typical method for representing continuous elements and captures the physical behavior of the fuel line adequately for this model. The constitutive equation for the two-phase resistance is

$$P_{i,2} - P_{man} = \dot{m}_{tp1} R_{tp1} \tag{3.30}$$

while the description of the fuel inertia is

$$\frac{d\dot{m}_{fi}}{dt} = \frac{1}{In_{fi}}\left(P_{mj} - P_{i,1}\right) \tag{3.31}$$

The elements are constrained such that mass must balance at the mixing zone. Here we assume that the mixing zone has negligible volume (although this volume could be represented using a capacitance in more advanced idle path configurations or models) so that

$$\dot{m}_{ap} + \dot{m}_{fi} = \dot{m}_{tp1} \tag{3.32}$$

Equations (3.28) through (3.32) represent 5 equations in 5 unknowns: $P_{i,1}$, $P_{i,2}$, $\dot{m}_{ap}$, $\dot{m}_{tp1}$, and $\frac{d\dot{m}_{fi}}{dt}$. The state variable that defines the system is $\dot{m}_{fi}$; this is evident by the fact that the energy stored by the fluid inertia is related to $\dot{m}_f$ and this is the only

variable that appears in a time derivative. The remaining unknowns could be removed from the governing equations using algebra; however, for convenience and clarity they are retained. The calculation of the derivative of the mass flow rate of the fuel and the other intermediate variables is computed by placing Equations. (3.28) through (3.32) in matrix form

$$\begin{bmatrix} 1 & -1 & 0 & 0 & 0 \\ 0 & 1 & R_{ap} & 0 & 0 \\ 0 & 1 & 0 & -R_{tp1} & 0 \\ 0 & 0 & 1 & -1 & 0 \\ \dfrac{1}{In_{fi}} & 0 & 0 & 0 & 1 \end{bmatrix} \begin{bmatrix} P_{i,1} \\ P_{i,2} \\ \dot{m}_a \\ \dot{m}_{tp} \\ \dfrac{d\dot{m}_f}{dt} \end{bmatrix} = \begin{bmatrix} \dot{m}_{fi} R_{fi} \\ P_{up,v} \\ P_{man} \\ -\dot{m}_{fi} \\ \dfrac{P_{mj}}{In_{fi}} \end{bmatrix} \tag{3.33}$$

or

$$A X = b \tag{3.34}$$

Under typical conditions, the resistances associated with the air and two-phase paths are much larger than the resistance associated with the fuel. Therefore, the matrix equation is poorly conditioned (the elements in the 1st row are 8 orders of magnitude smaller than those in other rows). This will be true in many idle path configurations where the resistance to the flow of a given mass flow rate of air or two-phase mixture that is composed mostly of air, by volume, will always be larger than the resistance to the flow of a fuel. As a result, it is advantageous to decompose the matrix *A* into a lower and upper triangular matrix, *L* and *U*, using an LU decomposition algorithm defined by Press [56].

$$LU X = b \tag{3.35}$$

The lower triangular element is well conditioned and therefore it is possible to solve the equation

$$U\,X = Y \tag{3.36}$$

where

$$Y = L^{-1}\,b \tag{3.37}$$

by starting from the last element and working backwards explicitly. Therefore

$$\frac{d\dot{m}_{fi}}{dt} = \frac{Y(5)}{U(5,5)} \tag{3.38}$$

and

$$\dot{m}_{tp1} = \frac{Y(4) - U(4,5)\dfrac{d\dot{m}_{fi}}{dt}}{U(4,4)} \tag{3.39}$$

and so on for the other elements in the matrix. The function `stder.m` carries out these calculations given arbitrary inputs and is contained in Appendix A.3.

3.5 Integration of the State Variables over the System Timestep

The procedure described in Section 3.4 provides the derivative of the state variable(s) evaluated as a function of the variable(s) itself; for the current idle path configuration this can be written functionally as

$$\frac{d\dot{m}_{fi}}{dt}\left(\dot{m}_{fi}\right) \tag{3.40}$$

The derivative(s) are integrated through the system timestep (Δt) using a Runge-Kutta 4th order (RK4) integration procedure. The system timestep is divided into N local timesteps (Δt_l)

$$\Delta t_l = \frac{\Delta t}{N} \tag{3.41}$$

To move through any local timestep, the derivative is evaluated 4 times according to

$$\left.\frac{d\dot{m}_{fi}}{dt}\right|_1 = \frac{d\dot{m}_{fi}}{dt}\left(\dot{m}_{fi,i}\right) \tag{3.42}$$

$$\left.\frac{d\dot{m}_{fi}}{dt}\right|_2 = \frac{d\dot{m}_{fi}}{dt}\left(\dot{m}_{fi,i} + \frac{\Delta t_l}{2}\left.\frac{d\dot{m}_{fi}}{dt}\right|_1\right) \tag{3.43}$$

$$\left.\frac{d\dot{m}_{fi}}{dt}\right|_3 = \frac{d\dot{m}_{fi}}{dt}\left(\dot{m}_{fi,i} + \frac{\Delta t_l}{2}\left.\frac{d\dot{m}_{fi}}{dt}\right|_2\right) \tag{3.44}$$

$$\left.\frac{d\dot{m}_{fi}}{dt}\right|_4 = \frac{d\dot{m}_{fi}}{dt}\left(\dot{m}_{fi,i} + \Delta t_l\left.\frac{d\dot{m}_{fi}}{dt}\right|_3\right) \tag{3.45}$$

where $\dot{m}_{fi,i}$ is the mass flow rate of fuel at the beginning of the local timestep. The mass flow rate at the end of the local timestep ($\dot{m}_{fi,i+1}$) is therefore

$$\dot{m}_{fi,i+1} = \dot{m}_{fi,i} + \frac{\Delta t_l}{6}\left(\left.\frac{d\dot{m}_{fi}}{dt}\right|_1 + 2\left.\frac{d\dot{m}_{fi}}{dt}\right|_2 + 2\left.\frac{d\dot{m}_{fi}}{dt}\right|_2 + \left.\frac{d\dot{m}_{fi}}{dt}\right|_4\right) \tag{3.46}$$

This process is repeated N times to simulate each substep that makes up the system timestep. The result of the integration is the new fuel flow rate as well as any secondary variable of interest (e.g., the air flow rate) at the end of the timestep. The function `idlepath.m` is contained in Appendix A.4.

3.6 Nominal Results for the Briggs & Stratton Intek Engine

Eventually, the carburetor idle path model will be integrated with a system level simulation code. For debugging and demonstration purposes, the `idlepath.m` file is executed from a MATLAB shell script (`runidlepath.m`) that calls the idle path model using a matrix that includes the boundary pressures ($P_{up,v}$, P_{man}, and P_{mj}) at different times (contained in the vector *time*) associated with a single stroke of the engine. The process is started from an arbitrary initial fuel mass flow rate and continues until the system reaches a cyclic steady state. The process could be run for any arbitrary pressure/time variation that is, for example, predicted by GT power for transient operation of a particular engine or even measured data for an engine. The code `runidlepath.m` is contained in Appendix A.5.

Figure 3.6 illustrates the pressure variations associated with the Briggs and Stratton Engine operating at a 3° throttle angle and 1800 [rev/min]. The parameters required to simulate this engine in GT-Power are included in Appendix B.1. The fuel well and Venturi pressures do not vary significantly whereas the manifold pressure drops dramatically during the intake portion of the stroke. The manifold pressure falls below the critical pressure; therefore, if this idle path was equipped with a transition system then the pressure at the nozzle formed by the throttle plate would be at the choked condition.

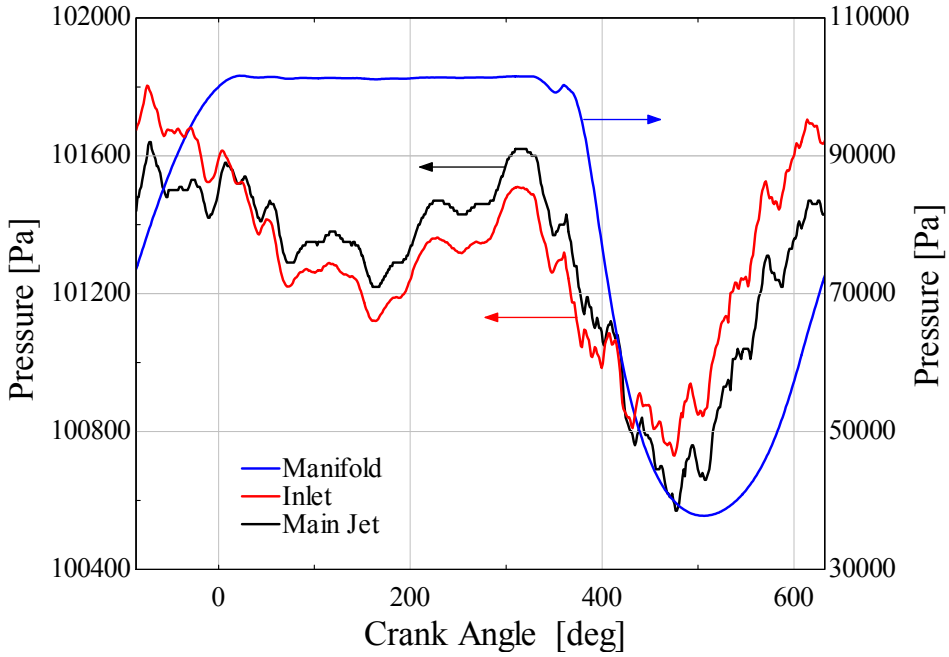

Figure 3.6: Venturi, manifold, and fuel well pressures for a Briggs & Stratton Intek Engine carburetor operating at a 3° throttle angle and 1800 [rev/min]. Note choking at the throttle plate occurs around 52000 Pa.

Figures 3.7 illustrates the fuel and bleed air flow rates as a function of crank angle for the same simulation conditions as that listed in Fig. 3.6. A plot of fuel flow rate predicted by a quasi-steady model (labeled QSS) is also shown. A quasi-steady model is produced from the dynamic model by setting the inertia in the system to a value close to zero.

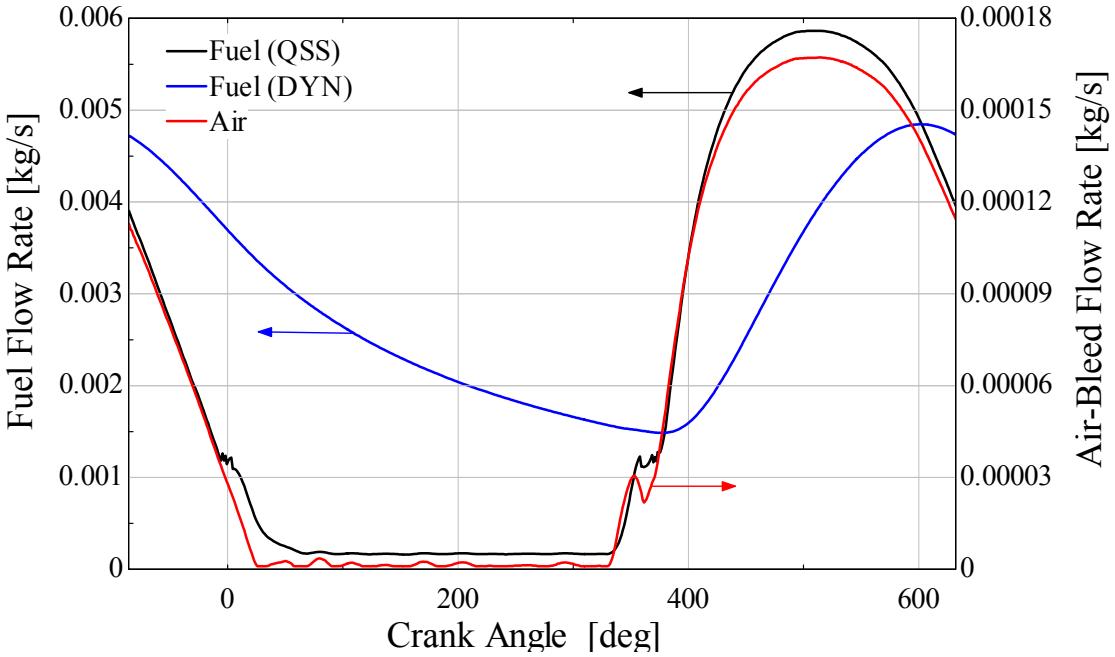

Figure 3.7: Fuel and air-bleed flow as a function of crank angle for a Briggs & Stratton Intek Engine carburetor at a 3° throttle angle and 1800 [rev/min]

Notice that when the inertia of the idle path system is included, the idle path delivers significantly more fuel than is predicted by the quasi-steady state (QSS) solution. The suction signal from the manifold is so strong at a throttle opening of 3° that fuel flow never ceases during steady engine operation because the inertia of the fuel continues to drive the flow even after the manifold pressure returns to near atmospheric conditions. The plot of the QSS solution shows that when the inertia of the fuel is not considered, the flow responds instantaneously to the air flow rate (also shown) and ceases instantaneously when the pressure difference between the manifold and main jet falls to zero. Note that the fuel flow in the QSS solution does not quite reach zero due to limits imposed in the code to prevent singularities at very low mass flow rates.

3.7 Boundary Condition Calculations for Idle and Transition Path Circuit

3.7.1 Solving for Pressure at Transition System Discharge Holes

Figures 3.5 and 3.6 indicate that the idle path model requires several boundary conditions. The pressure upstream of the Venturi ($P_{up,v}$) and the pressure in the intake manifold (P_{man}) are taken at directly from the GT-Power simulation. If the carburetor is equipped with a transition system then the pressure at the throat of the nozzle formed by the throttle plate and the venturi wall (P_{th1}, see Figure 3.8) is also required in order to simulate the first transition system hole. The pressure boundary conditions that would be required for additional transition holes would be labeled as P_{th2}, and so on.

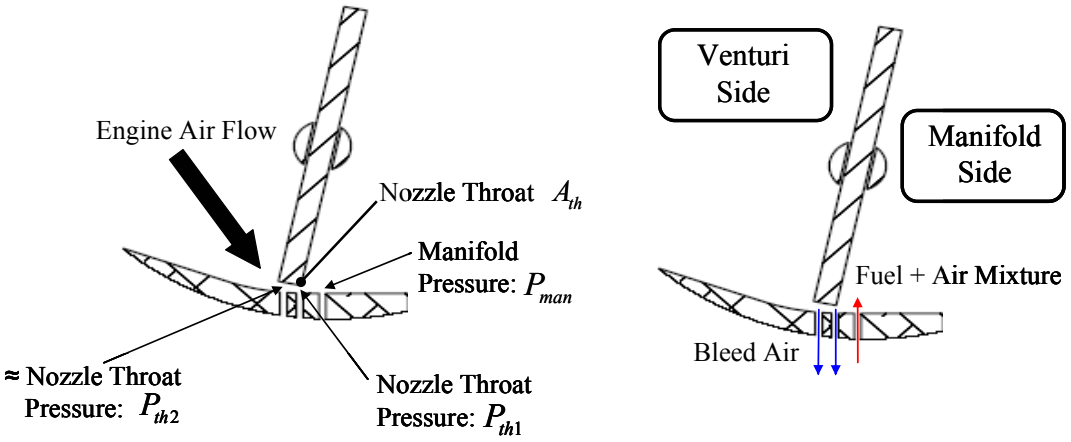

Figure 3.8: Terminology associated with transition system boundary conditions and depiction of current flow directions at pictured throttle angle

Calculation of the pressures associated with the transition system, requires solution of equations (2.3) and (2.5) that characterize flow around the throttle plate; these equations are repeated here for convenience. These two equations solve for the area formed by the throttle plate and the pressure at the throat of the nozzle assuming isentropic flow. GT-Power will solve for this pressure if the entire geometry of the venturi is simulated. In most applications however, the entire carburetor is placed on a flow bench and a discharge coefficient map is produced for varying throttle angles. This

map of discharge coefficient versus throttle angle is then input into GT-Power and hence all information concerning the pressure at the throat of the nozzle formed by the throttle plate is lost.

$$\begin{aligned} A_{th}(\theta) &= \frac{\pi D^2}{4}\left[1-\frac{\cos\theta}{\cos\theta_o}\right] \\ &+\frac{d}{2\cos\theta}\sqrt{D^2\cos^2\theta - d^2\cos^2\theta_o} \\ &+\frac{D^2\cos\theta}{2\cos\theta_o}\sin^{-1}\left(\frac{d\cos\theta_o}{D\cos\theta}\right)-\frac{d}{2}\sqrt{D^2-d^2} \\ &+\frac{D^2}{2}\sin^{-1}\left(\frac{d}{D}\right) \end{aligned} \tag{3.47}$$

$$\dot{m}_{engine} = C_{d,th}A_{th}[2\rho_o(p_o - p_{th})^{1/2}\left\{\frac{[\gamma/(\gamma-1)][(p_{th}/p_o)^{1/2}-(p_{th}/p_o)^{(\gamma+1)/\gamma}]}{1-(p_{th}/p_o)}\right\}^{1/2} \tag{3.48}$$

$\dot{m}_{engine}$ is the mass flow rate of air through the engine, specified by GT-Power, $C_{d,th}$ is the discharge coefficient of the throttle plate and is used to account for loss effects at a specified throttle angle θ, A_{th} is the area formed by the throttle plate and the wall of the venturi, and P_{th} is the pressure at the throat. In the case of the transition system pictured in Figure 3.7, P_{th} corresponds to P_{th1} or P_{th2}. The area formed by the throttle plate changes as a function of throttle angle, as depicted in Figure 3.9 for the BSI carburetor.

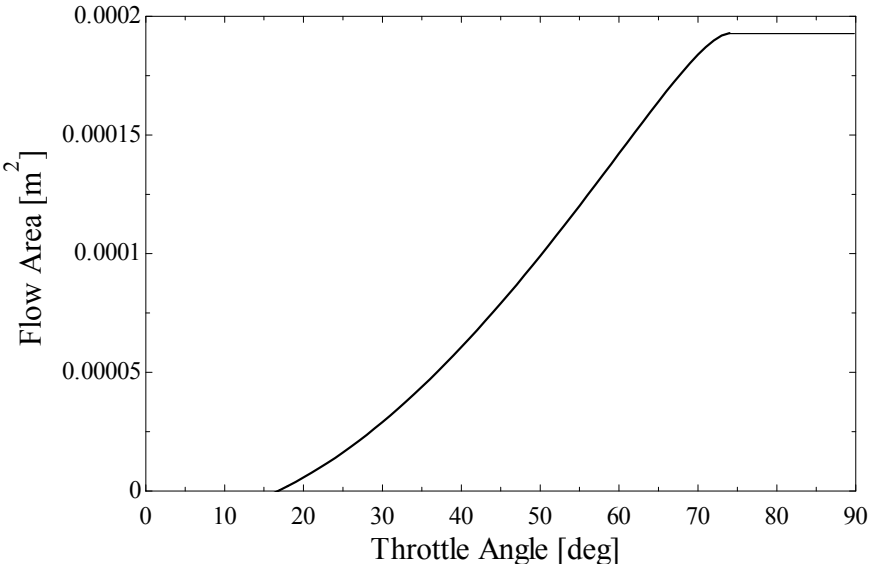

Figure 3.9: Throttle flow area as a function of throttle angle for the Briggs & Stratton Intek Engine carburetor

The throttle area reaches a maximum at 74^{o} due to shaft blockage effects and the throttle effectively closes at 17^{o}.

The discharge coefficient of the throttle plate is also a non-linear function of the throttle angle; the discharge coefficient of the throttle plate is shown in Figure 3.10 based on data collected by Harrington [11].

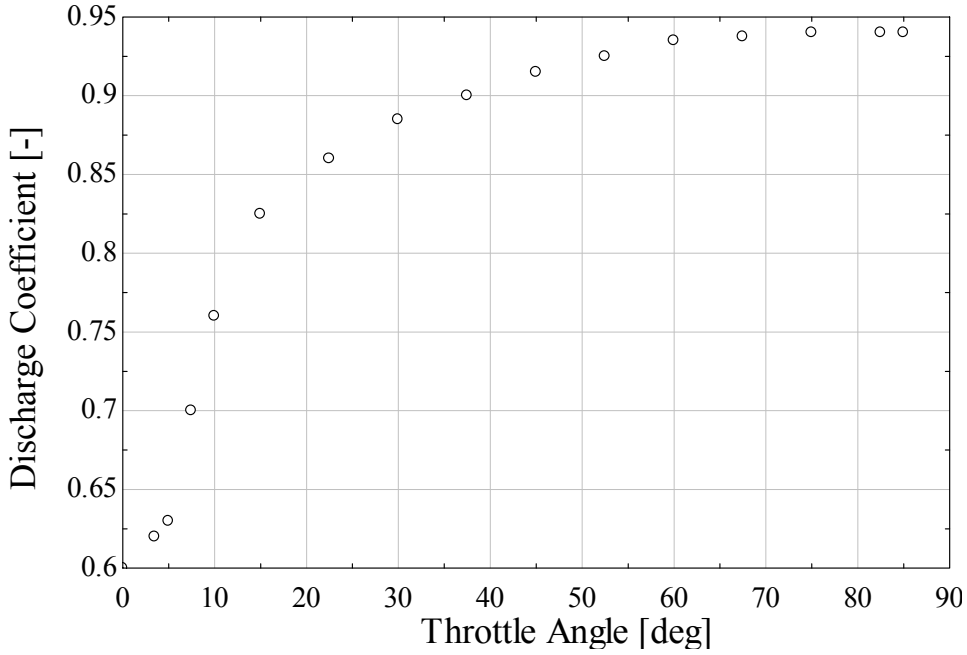

Figure 3.10: Experimentally determined discharge coefficient as a function of throttle angle for a generic throttle plate as taken from Harrington [11]

If the backpressure falls below the critical pressure then the system is choked according to equation (2.4) and the mass flow rate reaches a maximum. Solving for the throat pressure in equation (3.48) requires an iterative routine which is accomplished in MATLAB using a root finding algorithm. The `fzero` function finds the root of a specified function. In this case, equation (3.48) is rewritten as follows

$$Y = \left(C_{d,th}A_{th}\right)^2 \left(2\rho\left(P_o - P_{th}\right)\right)\left[\left(\frac{\gamma}{\gamma-1}\right)\left(\frac{\left(\frac{P_{th}}{P_o}\right)^{\frac{2}{\gamma}} - \left(\frac{P_{th}}{P_o}\right)^{\left(\frac{\gamma+1}{\gamma}\right)}}{1-\frac{P_{th}}{P_o}}\right)\right] - \dot{m}_{engine}^{\,2} \qquad (3.49)$$

where Y is the variable to be minimized by varying P_{th}. Mathematically, this minimization is accomplished by one of three methods [57]: the bisection, the secant, or the inverse quadratic interpolation method. The routine requires a guess value to start the

procedure that is calculated by assuming incompressible flow across the throttle plate. Specifically, the equation used to generate a guess value is

$$P_{guess} = P_o - \frac{\dot{m}_{engine}^2}{2\rho(C_{d,th}A_{th})^2} \tag{3.50}$$

where P_{guess} is the calculated guess pressure inserted into the `fzero` optimization routine.

The solution for the throttle plate pressure as a function of crank angle is presented in Figure 3.11 for various throttle angles with other required input data stemming from simulations conducted in GT-Power.

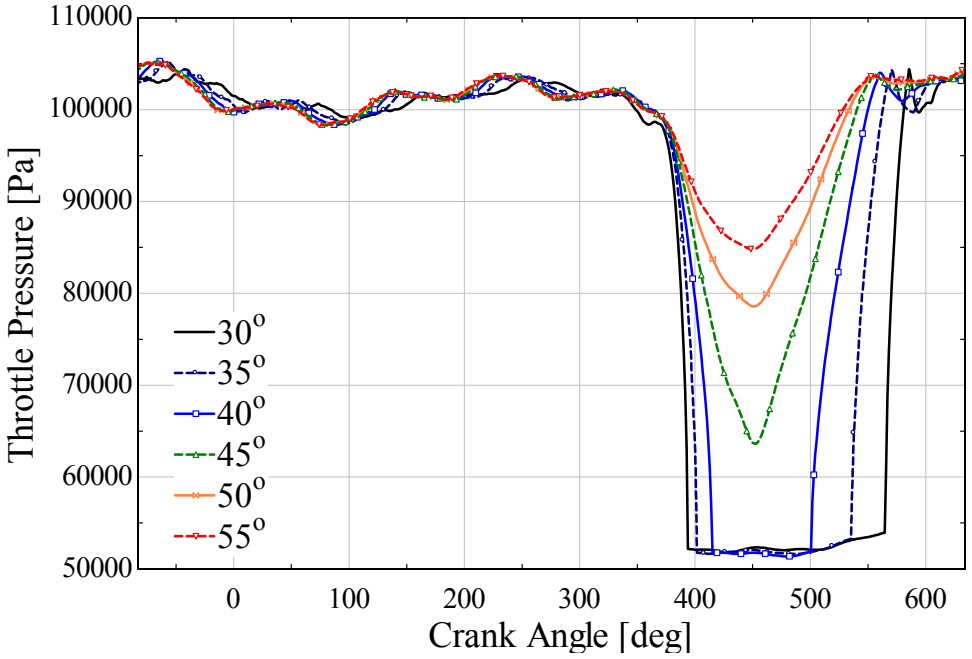

Figure 3.11: Throttle pressure as a function of crank angle for varying throttle angle, calculated in MatLab with data for air flow rate taken from GT-Power at 1800 [rev/min] with a BSI carburetor.

As can be seen in this figure, at low throttle angles (<45°), the airflow through the throttle reaches the critical pressure and chokes, leading to a relatively constant throttle pressure with time during the intake portion of the cycle. The pressure distribution

around the throttle plate and the geometric information about the position of the transition system holes in relation to the throttle plate can be used to specify the boundary condition at the transition hole. Using this information and output from GT-Power, the idle path configuration that contains an optional transitional system can be simulated.

The last boundary condition is the pressure after the main jet (P_{mj}) which requires a solution of the main path system. A method used to calculate the pressure after the main jet, based on the model created by Arias [41] is detailed in the next section.

3.7.2 Calculation of the Main Jet Pressure Using a Simplified Main Path Model

To complete the specification of the boundary conditions required to operate the idle/transition path model in MATLAB; information is needed about the pressure after the main jet as a function of crank angle. The model presented by Arias [43] can be coupled with GT-Power and used to directly solve for this pressure. Alternatively, a modified model was created in MATLAB using the same system of equations derived by Arias [2,41] but implemented using a modeling methodology that is similar to what was described for the idle path in Figure 3.1. The electrical analog of the main path circuit is presented in Figure 3.12 along with the simplified version, detailed next. Table 3.2 defines each variable.

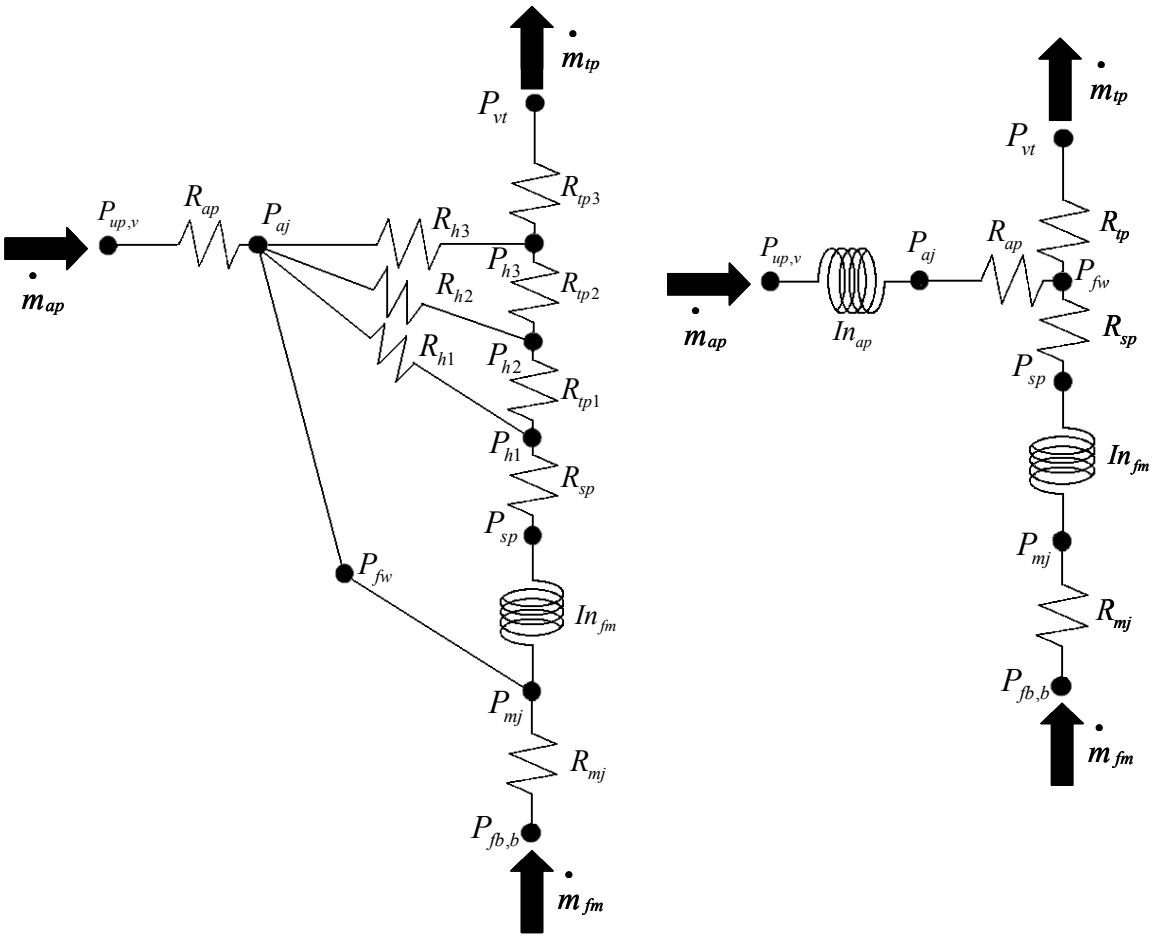

Figure 3.12: Electric analog descriptions of main path from Arias and presented simplified main path circuit

Table 3.2: Variable definitions for Figure 3.12

Variable	Description
$\dot{m}$	Mass flow rate
P	Pressure
R	Resistance to fluid flow
In	Inertia
Subscript	**Description**
fm	Fuel in the main path circuit
fw	Fuel well
mj	Main jet
fb,b	Bottom of the float bowl
sp	Single phase fuel section
h1	at the first set of emulsion tube holes
h2	at the second set of emulsion tube holes
h3	at the third set of emulsion tube holes
tp1	in the first two-phase section of the emulsion tube
tp2	in the second two-phase section of the emulsion tube
tp3	in the third two-phase section of the emulsion tube
up,v	upstream of the Venturi
aj	main air-bleed metering orifice
ap	air path

The parallel resistances governing airflow through the main path (R_{h1}, R_{h2}, R_{h3}) and the three consecutive two-phase resistances (R_{tp1}, R_{tp2}, R_{tp3}) are combined into a single resistance that governs the two-phase pressure loss through the main path. The resistance of the single phase fuel section, main jet (R_{sp} and R_{mj}), and the resistance of the air path (R_{ap}) remain unchanged; their specification is the same as that found in the model formulated by Arias [41]. Dynamic fuel flow effects in the main path are accounted for in the same manner as that for the single phase fuel section in the idle path, and it was discovered that adding an inertial term to the air-bleed side added stability to the numerical solution thought it did nothing to alter the results of the simulation.

The resistances and inertial terms used to simulate the main path system are listed next. Calculation of fluid resistances and inertial terms is the same as that given in the

idle path but applied to the geometry of the main path system. A more in-depth description of the two phase section found in the main path logically follows.

The resistance of the main jet R_{mj} is defined as follows

$$P_{fb,b} - P_{mj} = \dot{m}_{fm} R_{mj} \tag{3.51}$$

The resistance of the main jet is characterized by its diameter, discharge coefficient, and fluid velocity. The metered fuel then flows into the single phase portion of the emulsion tube which uses a series representation to define the inertia and resistance of the single phase fuel section. Note the resistance of the single phase fuel section and all other resistances described in equations 3.51 through 3.57 include frictional pressure loss effects, entrance and exits pressure losses, and other minor losses similar to the resistances identified in Section 3.3.

$$P_{mj} - P_{sp} = \frac{d\dot{m}_{fm}}{dt} In_{fm} \tag{3.52}$$

$$P_{sp} - P_{et} = \dot{m}_{fm} R_{sp} \tag{3.53}$$

At the end of the single phase portion of the emulsion tube, the fuel encounters bleed air and mixes. The two-phase flow through the emulsion tube is now govern by a single resistance described by equation 3.54. The two-phase mixture empties to the venturi throat and is governed by the venturi throat pressure boundary condition.

$$P_{et} - P_{vt} = \dot{m}_{tp} R_{tp} \tag{3.54}$$

Returning now to the air side, the bleed air enters the system through a metering orifice upstream of the venturi throat at the stagnation pressure. A series representation of the resistance associated with passage through the air bleed system and an inertial term

describing the fuel flow response delay are used to represent the bleed air system just as the single phase fuel section is represented with a resistance and inertial term. The equations governing the air flow through the bleed system are described in equations 3.55 and 3.56.

$$P_{up,v} - P_{aj} = \frac{d\dot{m}_{ap}}{dt} In_{ap} \tag{3.55}$$

$$P_{aj} - P_{et} = \dot{m}_{ap} R_{ap} \tag{3.56}$$

The six constitutive equations are governed by a constraint equation that balances mass flow at the emulsion tube hole. The constraint equation is given in equation 3.57.

$$\dot{m}_{fm} + \dot{m}_{ap} = \dot{m}_{tp} \tag{3.57}$$

Equations 3.51 and 3.57 are collected and rearranged in matrix form, as the idle path was in Section 3.4, and are solved using the same RK4 integration method with LU decomposition.

Returning now to the two-phase resistance identified in equation 3.54, and the electrical analog diagram of Figure 3.12b, the value of the single two-phase resistance must be controlled through constraint equations to properly approximate the function of three sets of emulsion tube holes (and therefore six resistances) as identified in Figure 3.12a for this carburetor model. The equations implemented in the model to define the function of the variable area emulsion tube hole are described next.

Model implementation is accomplished by applying constraint equations to control the system response. Instead of treating each level of emulsion tube holes as a discreet entity, all levels of emulsion tube holes are absorbed into a single hole set that has a variable area, mathematically detailed in equations 3.58, 3.59, and 3.60. This

system then bases the resistance to airflow through the emulsion tube on this collective area. Therefore instead of performing a separate mass balance at each level of emulsion tube holes, the new model approximates this scenario by assuming only one hole exists but its area can change to adjust its resistance. The method is also diagrammed in Figure 3.13.

$$A_{et,total} = n_{et,1} \frac{\pi D_{et,1}^2}{4}\bigg|_1 \tag{3.58}$$

$$A_{et,total} = n_{et,1} \frac{\pi D_{et,1}^2}{4}\bigg|_1 + n_{et,2} \frac{\pi D_{et,2}^2}{4}\bigg|_2 \tag{3.59}$$

$$A_{et,total} = n_{et,1} \frac{\pi D_{et,1}^2}{4}\bigg|_1 + n_{et,2} \frac{\pi D_{et,2}^2}{4}\bigg|_2 + n_{et,3} \frac{\pi D_{et,3}^2}{4}\bigg|_3 \tag{3.60}$$

$A_{et,total}$ represents the area that air will pass through when bleeding into the emulsion tube, and n_{et} defines the number of holes at each level in the emulsion tube. Some designs use only one, while others use 2 or 4 holes at each level. D_{et} is the diameter of each emulsion tube hole. For instance, when two levels of emulsion tube holes are uncovered in the fuel well based on a pressure balance, detailed in equations 3.52 through 3.56, the model will select the total flow area given by equation 3.52 to calculate the resistance to air flow through the emulsion tube. As the air flow to the engine is increased, the fuel level in the fuel well will drop uncovering another set of emulsion tube holes. The model will detect this condition and specify the area of the emulsion tube hole (and hence its resistance to air flow) as the area given by equation 3.53.

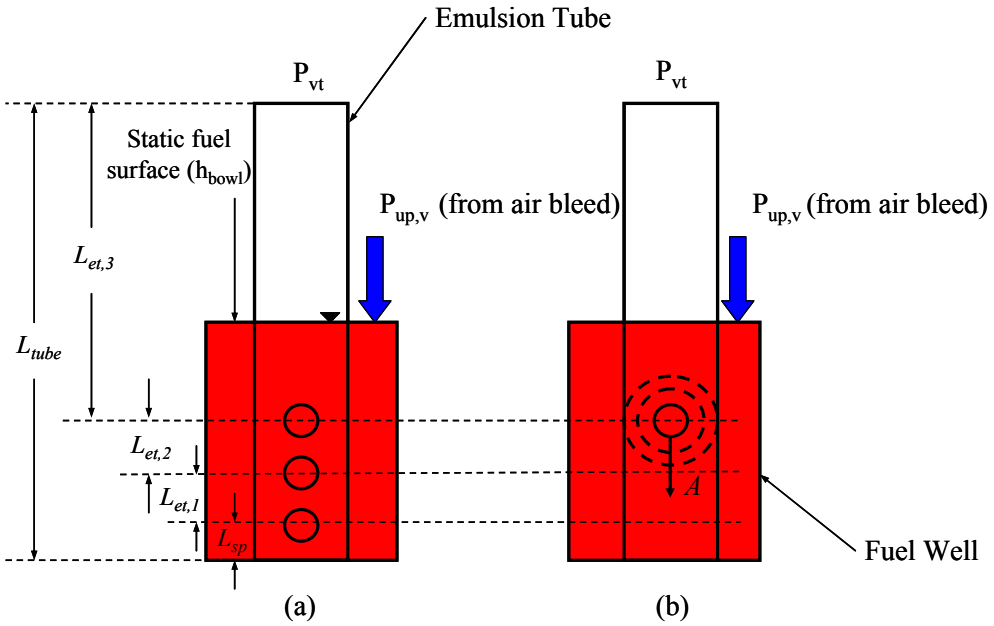

Figure 3.13: Emulsion tube model for main path approximation showing the situation under which air flow does not enter the emulsion tube.

In figure 3.13, L defines a characteristic length and A defines the area of the expanding/ contracting orifice. The pressure constraints simulating the behavior of the fuel well are given as follows and the sequence of events which activates each equation is described next.

$$\Delta P = P_{up,v} - P_{vt} \tag{3.61}$$

$$\Delta P < \rho_f g\left(L_{tube} - h_{bowl}\right) \rightarrow \dot{m}_{fm} = 0; \dot{m}_{ap} = 0 \tag{3.62}$$

Returning briefly to Figure 3.12, the pressure differential used to drive bleed air into the emulsion tube is governed by the pressure differential identified in equation 3.61. When the difference between the throat pressure and pressure upstream of the air bleed is less than the hydrostatic pressure required to drive the fuel level in the fuel down and therefore lift fuel to the exit of the emulsion tube, then no fuel will flow through the system. The hydrostatic pressure difference required to turn on the main path system is given in equation 3.62. Note the pressure conditions use the $P_{up,v}$ boundary condition to

activate the constraints, but the resistance and therefore the airflow is governed by the dynamic pressure after the air side metering orifice identified as P_{aj} in Figure 3.12. This is an approximation used to explicitly define the pressure at the boundaries.

As engine air flow increases, the driving pressure differential in the air bleed system increases and forces the level in the fuel well down even further. If the pressure differential is less than the hydrostatic pressure required to uncover the first set of emulsion tube holes but greater than that required to start fuel flow, the main path will deliver single phase fuel only; the bleed air system will not activate. This condition is detailed in equation 3.63.

$$\rho_f g\left(L_{tube} - h_{bowl}\right) < \Delta P < \rho_f g\left(L_{et,3}\right) \rightarrow \dot{m}_{fm} \neq 0; \dot{m}_{ap} = 0 \tag{3.63}$$

With further increases in engine air flow, the driving pressure differential of the air bleed system will force the level of fuel in the fuel well even lower and this will eventually uncover a set of emulsion tube holes. At this point, air will enter the fuel and form a two phase mixture. The condition is diagrammed in Figure 3.14. The condition required to achieve a two-phase mixture is described in equation 3.64.

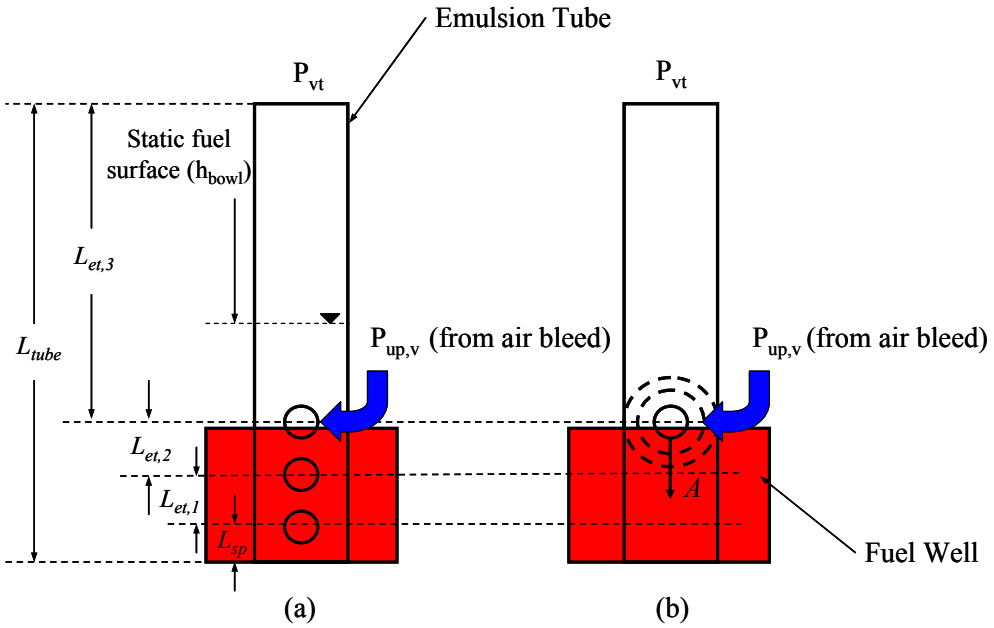

Figure 3.14: Emulsion tube model showing one set of holes uncovered

$$\Delta P > \rho_f g\left(L_{et,3}\right) \rightarrow \dot{m}_{fm} \neq 0; \dot{m}_{ap} \neq 0 \quad \left(1 \text{ hole set uncovered}\right) \tag{3.64}$$

After initiation of the air bleed system, the new model diverges in form from the Arias model. With still further increases in driving pressure differential two sets of emulsion tube holes uncover, air will enter both hole sets separately. In the new model the area of the orifice expands to simulate the area of two hole sets, as detailed in Figure 3.15. The constraint used to govern air flow into two hole sets and then three hole sets is detailed in equations 3.65 and 3.66.

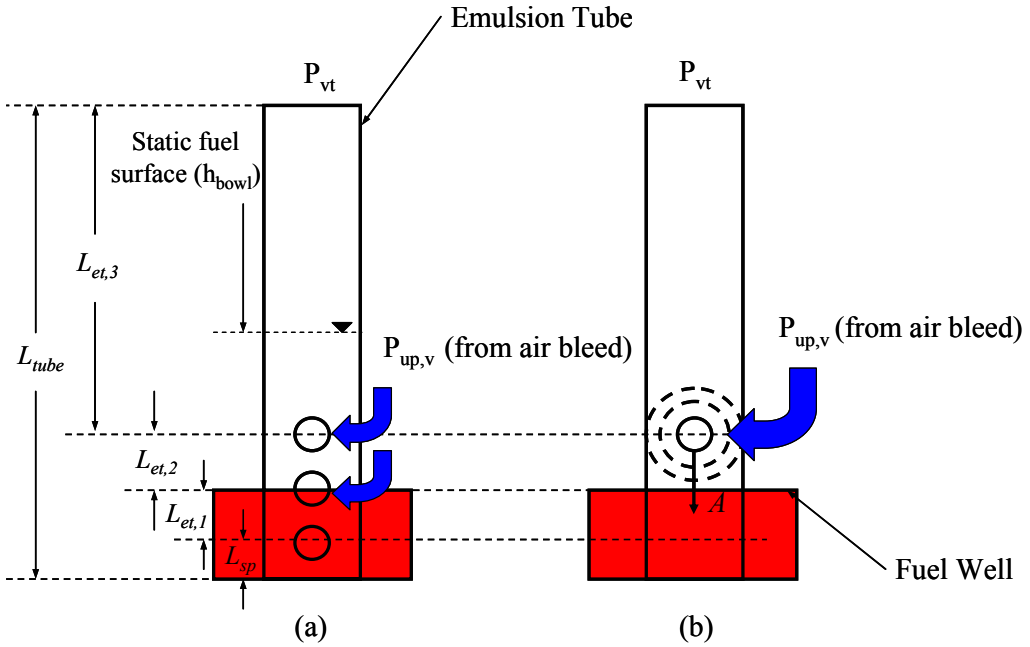

Figure 3.15: Air flow through two sets of emulsion tube holes as represented in the Arias model and in the newly proposed model

$$\Delta P > \rho_f g\left(L_{et,3} + L_{et,2}\right) \rightarrow \dot{m}_{fm} \neq 0; \dot{m}_{ap} \neq 0 \quad \left(2 \text{ hole sets uncovered}\right) \tag{3.65}$$

The representation of the emulsion tube model when three sets of holes are uncovered is detailed in Figure 3.16.

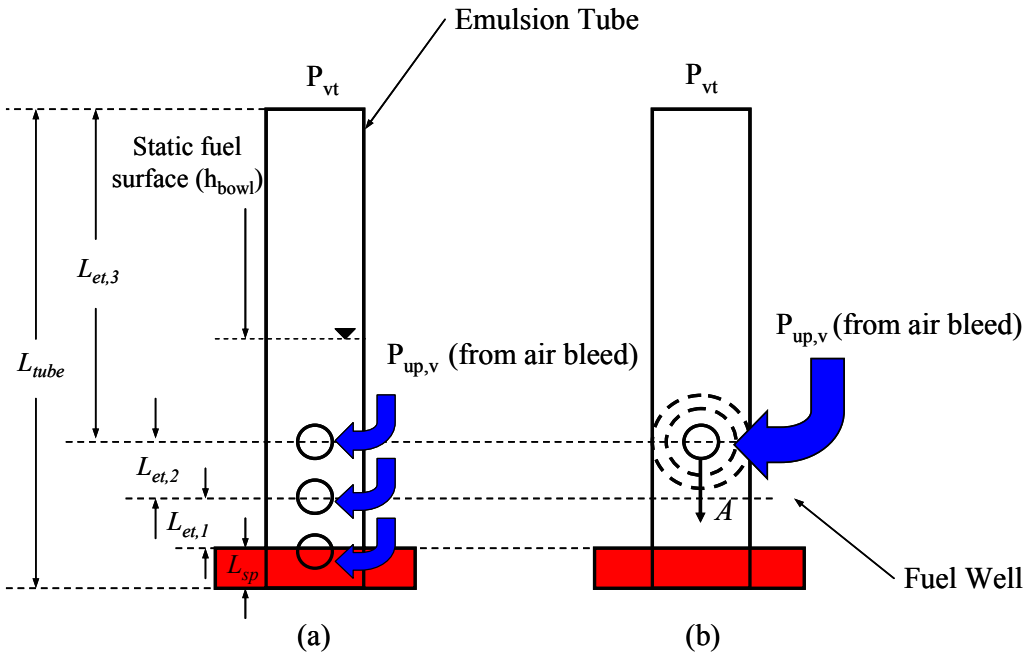

Figure 3.16: Model representation when three sets of emulsion tube holes are uncovered

$$\Delta P > \rho_f g\left(L_{et,3} + L_{et,2} + L_{et,1}\right) \rightarrow \dot{m}_{fm} \neq 0; \dot{m}_{ap} \neq 0 \quad \left(3 \text{ hole sets uncovered}\right) \quad (3.66)$$

Equation 3.66 describes the situation in which three hole sets are uncovered, but this could be extended to an arbitrary number of hole sets.

As constraint equations 3.62-3.66 are realized, i.e. as the dynamic pressure balance in the fuel well uncovers emulsion tube hole sets, the variable area orifice expands by decreasing the resistance to fluid flow in the two-phase element R_{tp}. The orifice expansion accounts for the increase in pressure loss due to surface tension effects with equation 3.67, and it also accounts for non-ideal air flow behavior through the emulsion tube holes with discharge coefficients similar to equation 3.5 for the pressure loss through the air-bleed system in the idle path.

$$\Delta p_{st} = \frac{4\sigma}{D_{et}} \quad (3.67)$$

where Δp_{st} is the additional pressure differential required due to surface tension effects. The surface tension is denoted as σ.

Further information on the equations implemented and the scheme used to control this system of equations is included in Appendix C.1-C.9. As with the idle path, the main path model is run by a similar shell model denoted as `runmainpath.m` with a calculation of the system resistances and inertial terms carried out in `GtoRmain.m` file. This file also contains the constraint equations used to model the emulsion tube holes. The integration through the system timestep using the RK4 method is carried out in `mainpath.m`, and the decomposition of the matrix is handled by `stder_main.m`. Finally, the geometry of the main path system is contained in the file `Nikki_Geometry.m`. Other functions are included in this appendix, but these files

only serve to simplify the coding process. For example, since the correlations for the laminar and turbulent friction factor are used often, the code set was turned into a function and is called within the `GtoRmain.m` file. Furthermore, all accessory programs are called within the `GtoRmain.m` file.

Figure 3.17 compares the fuel flow prediction of the simple main path model, referred to from here on as the SIMPLE model, with the dynamic model created by Arias, referred to as Arias (DYN) from here on, for three different engine speeds at WOT in a single cylinder engine using a Nikki carburetor.

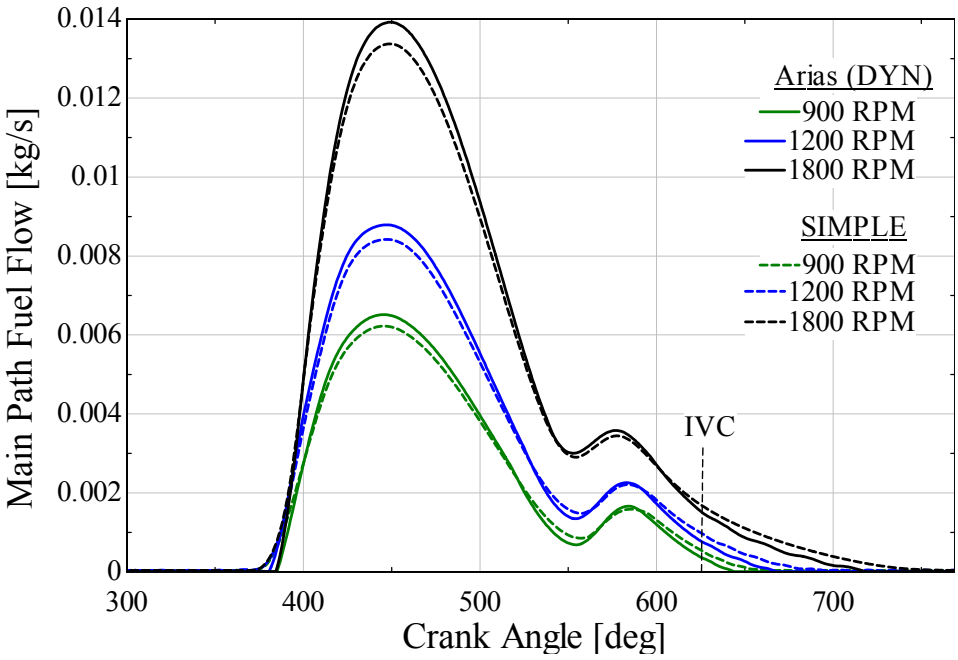

Figure 3.17: Fuel Flow prediction between the SIMPLE main path model created in MATLAB and the Arias (DYN) model created by Arias [41] in EES.

The SIMPLE model adequately captures the dynamic events of the fuel flow process. At Crank Angle = 632°, the intake valve closes and this cuts the driving pressure differential of the main path to zero. However, the inertia of the fuel in the main path circuit continues to drive fuel flow well after IVC. Comparing the integrated *AFR* for each engine speed, a maximum difference of 0.75% is encountered at the highest

engine speed of 1800 RPM. In each graph, the SIMPLE model slightly under predicts the peak fuel flow rate, and the duration of the fuel flow event is slightly larger than each curve derived from the Arias (DYN) model. This indicates a slight difference in the method used to model and predict inertial effects.

The SIMPLE model also performs well when compared against other models used to predict main path fuel flow, as shown in Figure 3.18. The Arias (DYN) model uses the unsteady one dimensional momentum balance described by equation 2.17, modeled in EES with a predictor-corrector timestep integration method. The Arias (QSS) model uses an algebraic momentum balance in EES to model single phase fuel flow; this results in a fuel flow curve that responds instantaneously with time. The Arias (GT-Power) model uses a modified Newton-Raphson method for solving the system of non-linear equations and integrates the differential momentum balance using a Crank-Nicolson scheme.

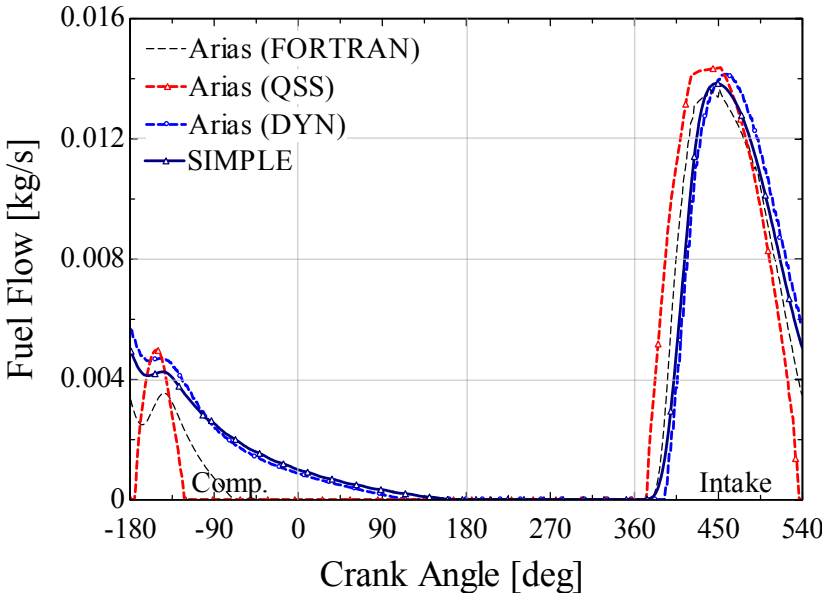

Figure 3.18: Comparison of four different fuel flow models used to predict fuel flow in the main path circuit.

The three dynamic models, namely the Arias (FORTRAN), Arias (DYN), and the SIMPLE (DYN) model all exhibit a characteristic first order response with regards to fuel flow meaning that after the signal to the venturi decays, fuel flow continues due to the momentum of the fuel. The difference in the prediction of *AFR* with the SIMPLE model and the Arias (DYN) model is smaller than the difference in the *AFR* predicted between the Arias (DYN) model and the identical model Arias (FORTRAN), implemented in GT-Power. This indicates that the SIMPLE model captures all the relevant fuel flow dynamics compared to other accepted models.

A change to the emulsion tube model has an effect on other aspects of the fuel system response. First, information concerning the quantity of bleed air entering each emulsion tube hole is lost. The simple model can only track the total bleed air admitted to the system. Second, the pressure drop applied inside the emulsion tube is altered and now only a single flow rate of air can be prescribed for the entire length of the tube. Therefore a correction is needed to correctly predict the bleed-air flow rate if accurate information of this kind is needed (for example, for use in a different model such as a droplet transport model). Despite these limitations, changes to the geometry of the emulsion tube are easily handled with a change to the file `GtoRmain.m` described in Section 3.3. No other subprograms need to be altered and, most importantly, the state derivation (Section 3.4) will only need to be performed once. This decreases the computational complexity of the entire program significantly.

Despite the inherent simplicity of the proposed SIMPLE model it predicts fuel flow well compared to previously published models. The sensitivity analysis performed by Arias [41] indicates that the most relevant parameter of the main path system is the

main jet diameter. The simplified model incorporates main jet and single phase fuel flow dynamics into the simulation, therefore this important aspect is accounted for. Second, Asano [58] recognized that the position of the first air bleed, and therefore the time it takes for the fuel level in the fuel well to reach that emulsion tube hole, dictates the response of the system; the SIMPLE main path model retains this information by positioning the expanding orifice at the height of the first emulsion tube hole set. The two-phase pressure drop occurring along the length of the emulsion tube is important, but only to determine total bleed air inducted into the fuel flow.

With a working model for the main path, the pressure after the main jet can be determined. Figure 3.19 shows a comparison between the pressure after the main jet as predicted by the SIMPLE model and the Arias (DYN) model.

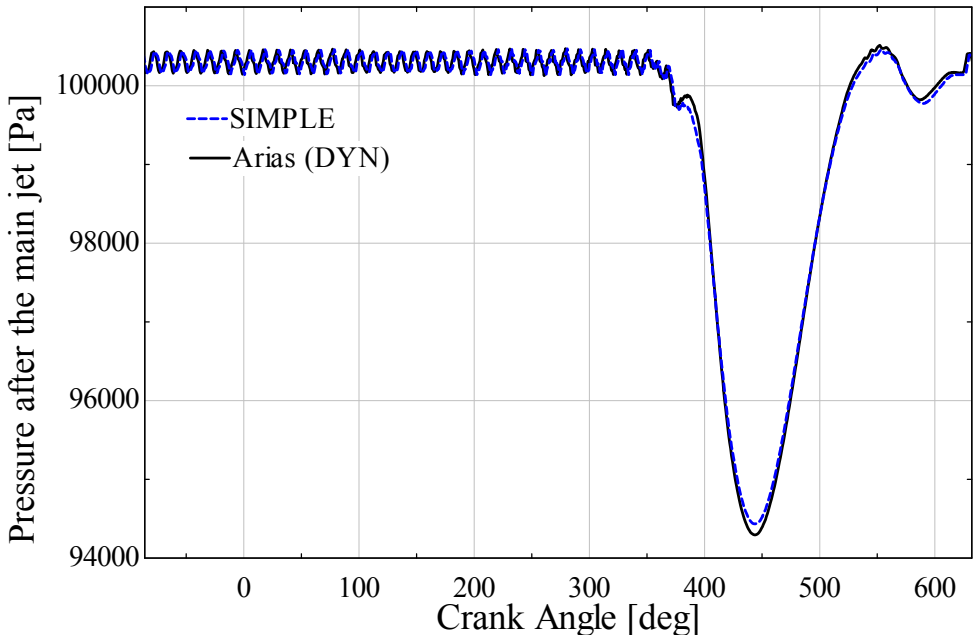

Figure 3.19: Predictions of main jet pressure with simple MATLAB main path model and EES model created by Arias for a Nikki carburetor at 900 RPM and WOT conditions.

Figure 3.19 shows the SIMPLE model does an adequate job of predicting main path pressure after the main jet for a given engine cycle.

3.8 Parametric Study of the Briggs & Stratton Intek Engine

3.8.1 Sensitivity Analysis

The dynamic model of the idle path, outlined in the previous sections, is explored in this section in the context of the fuel flow response of the Briggs and Stratton Intek carburetor. Changes in the fuel flow response can be interpreted as modifications in the integrated air-to-fuel ratio. The sensitivity study was carried out using a constant throttle angle (5^o) and a constant engine speed (900 RPM). The analysis identified those areas within the idle path that dominate the air fuel ratio and therefore should be the focus of further, more detailed study.

The relative sensitivity of the any parameter k (ε_k) can be computed according to

$$\varepsilon_k = \frac{\partial \dot{m}_{fi}}{\partial k} \frac{k}{\dot{m}_{fi}} \tag{3.68}$$

where ε_k represents the relative sensitivity of the fuel flow rate to changes in the parameter k. Every variable required to specify the carburetor and included in the file `geometry` (see Table 3.1) was perturbed in the sensitivity analysis, the results are summarized in Figure 3.20.

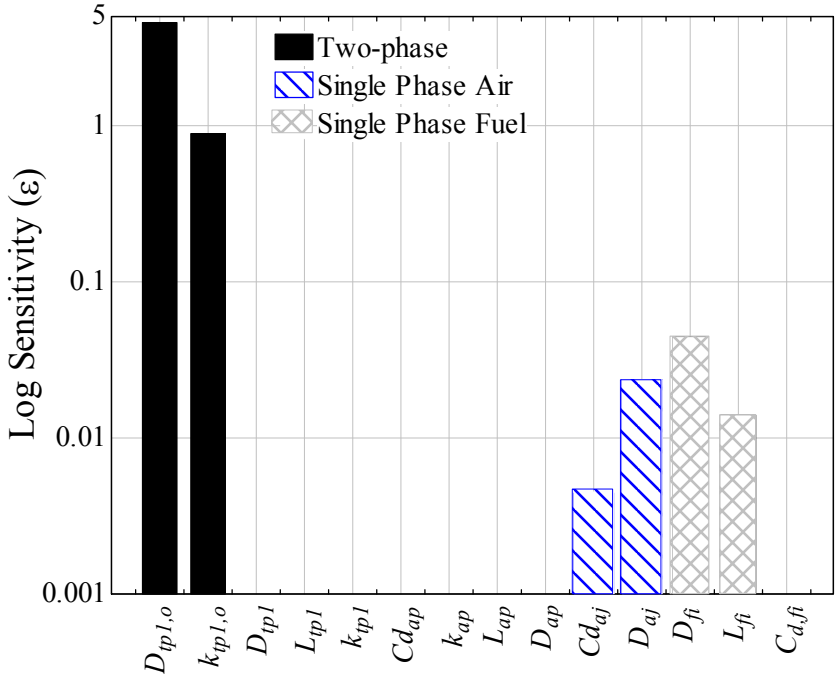

Figure 3.20: The relative sensitivity (ε_k) for each input parameter (k) contained in the `geometry` file shown in Table 3.1 simulated under dynamic conditions. Note that the sensitivity axis is a logarithmic scale.

The results indicate that the model is extremely sensitive to the diameter of the discharge holes in the throttle bore ($D_{tp1,o}$) and the loss coefficient ($k_{tp1,o}$) associated with the sudden expansion of the two-phase mixture into the intake manifold also has a large effect on the fuel flow response in the idle path. The analysis therefore also suggests that the modeling methodology that is used to determine the resistance of the two-phase section may be important. In addition, it appears that the single-phase air and fuel region has a small effect on the fuel flow response (see D_{fi}, L_{fi}, and D_{aj} in Fig. 3.20; however, the characteristics of the single-phase sections are of minor importance as compared to the two-phase region.

Examining the results of the sensitivity analysis reveals that the diameter and length of the single phase fuel section are important controlling parameters of the fuel flow curve. The orifice diameter of the single phase air section and its discharge

coefficient are also important with respect to the air-bleed flow rate, however, all of these effects are still small relative to the effects of the two phase region.

To summarize, the two-phase discharge diameter and loss coefficient are the controlling parameters for the idle path fuel flow response. The first single phase fuel section appears to be important in terms of the fuel flow response; however, its impact on the delivered fuel flow is relatively unimportant relative to the two-phase effects. The sensitivity of the single phase air diameter is also important but current techniques used to model this phenomenon are well-accepted in the published literature and further analyses will assume that this parameter is correctly modeled. All of the parameters that were identified as having some importance will be examined in further detail below; specifically, alternative techniques and correlations that can be used to model the two-phase flow losses and specify inertial effects will be examined.

3.8.2 Inertial Effects in the Single Phase Fuel Region

The sensitivity analysis identified that the dynamic effect of the inertia of the single phase fuel section may significantly alter the fuel flow response of the idle path. Inertial effects are manifested as an increased pressure drop related to accelerating or decelerating the fluid (i.e., changing its mass flow rate). As the diameter of the fuel line is decreased or its length is increased, the inertia of the fuel increases. Inertial forces also increase as the operating speed of the engine increases at higher engine speeds, the peak fuel flow decreases and the response curve (fuel flow versus time) exhibits a larger amount of phase shift relative to the driving pressure. The increase in frequency tends to maintain fuel flow for a significant period of time after the driving manifold pressure

differential drops to zero, a phenomenon that has been referred to previously as pulsation enrichment.

The fuel flow response of the Briggs and Stratton Intek carburetor idle path is shown below in Figure 3.21. The line labeled QSS corresponds to a quasi-steady approximation where the inertia in the model is set to zero and therefore the response of the idle path is instantaneous. The other curves represent various engine speeds. Notice that as the engine speed increases, the peak fuel flow decreases and the response exhibits a greater time delay. The total fuel flow over a cycle (for the idle path only) actually increases but only by a negligible amount as indicated by a slight decrease in the integrated air-to-fuel ratio shown in Figure 3.22.

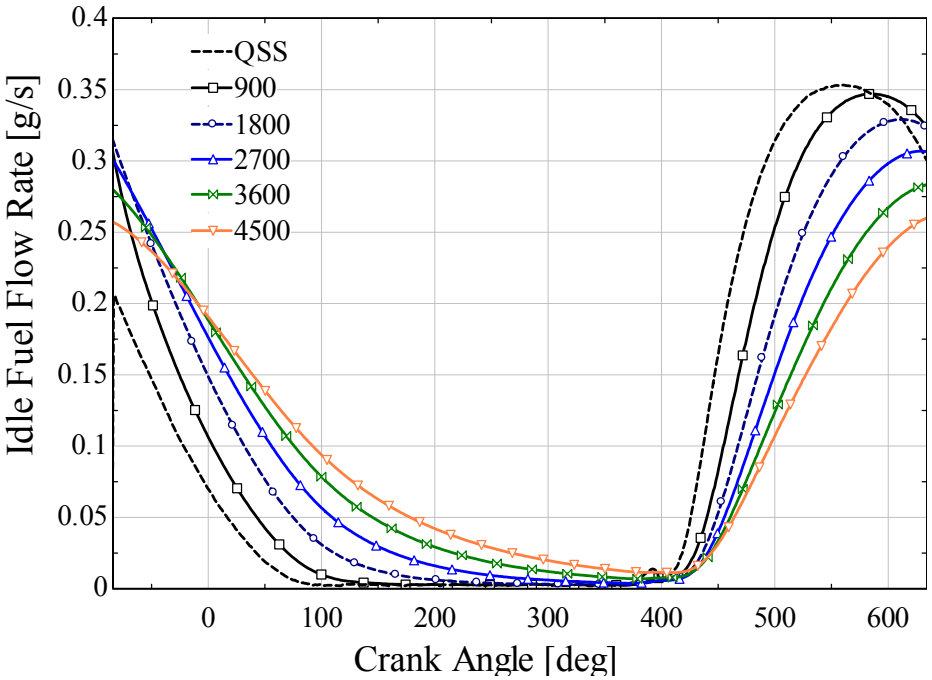

Figure 3.21: The effect of the inertia on the single-phase fuel region. Notice the overall increase in the fuel flow associated with going from the quasi-steady model, labeled (QSS), to the high speed condition.

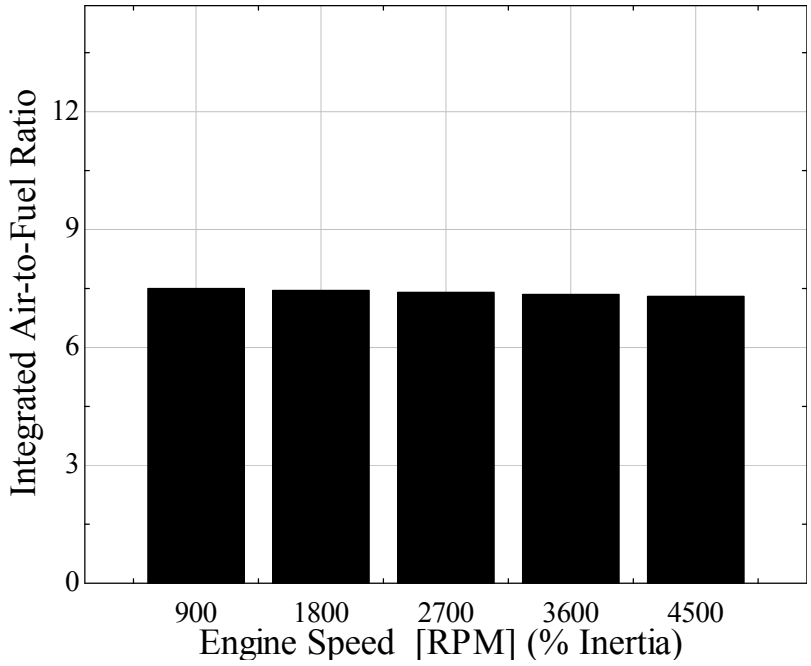

Figure 3.22: Integrated air-to-fuel ratios for Figure 3.21, showing that the A/F ratio is essentially unaffected by the inertia as given by the sensitivity analysis parameters L_{fi} and D_{fi}. There is a negligible fuel-enrichment associated with the inertia in this configuration of the idle path.

Figure 3.22 shows that the change in the integrated air-to-fuel ratio between a purely resistive idle path (QSS) and a resistive-inductive idle path at an engine speed of 4500 RPM is less than 2.7%. This implies that for this idle path configuration, inertial effects may be considered insignificant as they relate to the modeling technique (algebraic or differential equations) used to simulate the idle process. Although small, the increase in fuel flow also confirms the pulsation enrichment effects reported by Moss [33] and simulated by Arias [41]. Also, with smaller diameter and longer length single phase fuel sections, inertial terms may become more significant and careful consideration must be given to each analysis undertaken.

3.8.3 Two-Phase Flow Correlations

The sensitivity analysis indicated that the two-phase discharge port diameter ($D_{tp1,o}$) and loss coefficient associated with the discharge port ($k_{tp1,o}$) were the most important parameters relative to the fuel flow behavior. In order to better understand the processes within the two-phase section of the idle path, several pressure drop correlations were identified in the literature and used to model the two-phase frictional loss and the expansion loss. The different models for expansion losses produced a large variation in the predicted air-to-fuel ratio. The models used to describe frictional pressure drop produced large variations in *AFR* only when the path length was significantly large. Therefore, it is clear that a predictive model of the carburetor idle path requires an accurate predictive model of the two-phase behavior in the flow path.

The homogeneous model was previously described in Section 2.5.4 and Section 3.3.3, and was utilized to calculate the change in pressure along the length of the two-phase flow section for all of the results previously presented. However, as stated earlier, numerous authors and industry professionals question the validity of using the homogeneous model in this type of flow regime. Therefore, alternative correlations, summarized by Thome [59], were implemented to characterize the two-phase pressure drop and their effect on the integrated air-to-fuel ratio.

Figure 3.23 presents the fuel flow response of the current idle path configuration (L_{tp1} = 0.1 mm) when simulated with different two-phase frictional pressure drop models. The graph shows that for a short two-phase path length, model choice is not critical, which could be inferred from the sensitivity analysis. The integrated *AFR* for all models is approximately 9.9 except that of Friedel which is slightly leaner at 10.5.

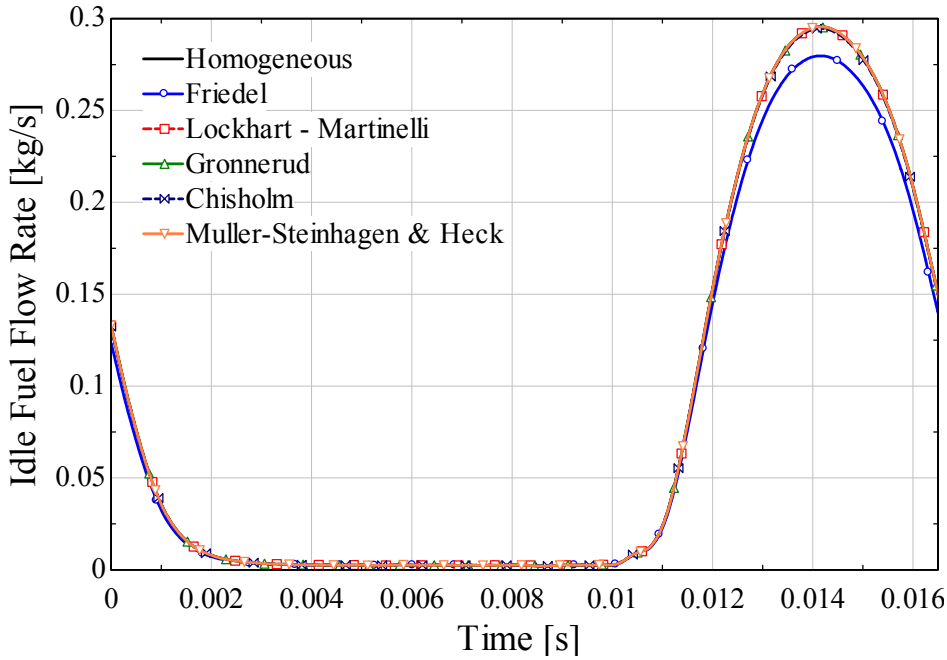

Figure 3.23: Two-phase flow frictional pressure drop correlations applied to two-phase zone in idle path for L_{tpI}= 0.01 mm. Correlations described by Collier and Thome [59].

Except for the curve using correlation given by Friedel, all other models appear to change the integrated air-to-fuel ratio by a very small amount. The short length of the two-phase section provides a very small pressure drop relative to other losses, and therefore changes in the model used to specify the two-phase pressure drop are unimportant. However if the length of the two-phase region is artificially lengthened, as in Figure 3.24, the fuel flow response changes dramatically. Although artificial in this model, lengthening the two-phase region is encountered in practice due to the wide variations present in carburetor design.

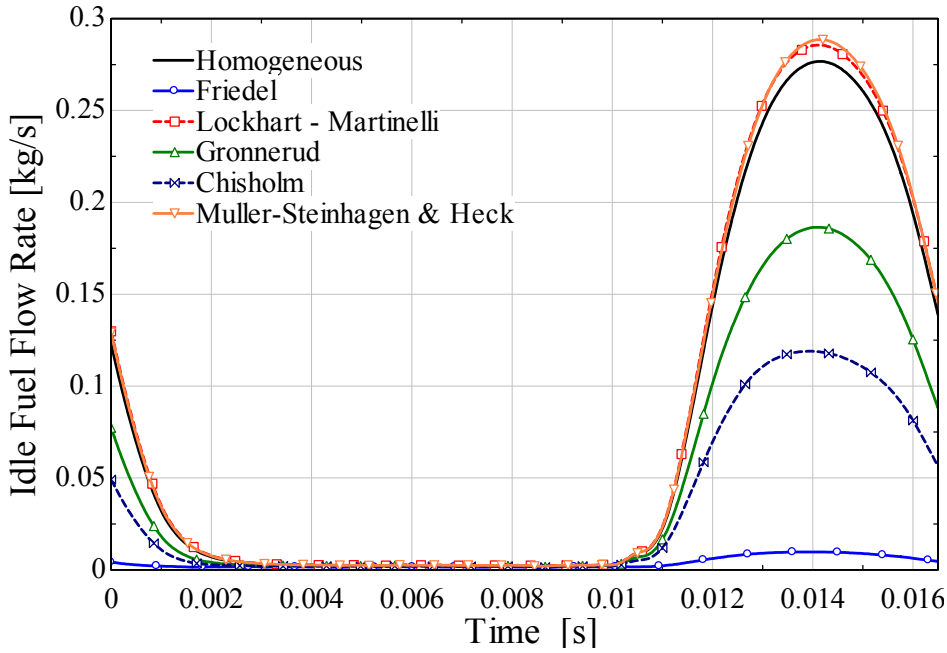

Figure 3.24: Fuel flow response variations due to two-phase frictional pressure drop model specified for an artificially long path length, L_{tp1}= 50.0 mm.

Figure 3.24 shows a wide variation in fuel flow rates for one complete cycle. The integrated *AFR* for five cycles can be examined in Figure 3.25. If the length of the two phase section is increased to 50.0 mm from 0.1 mm, then the pressure drop associated with friction in the two-phase region will increase and eventually dominate the pressure loss associated with the single phase sections and losses associated with bends and/or sudden expansion/contraction. This result indicates that carburetor designs and configurations will be sensitive to different parameters and any time a major change is made in the system, the controlling parameters should be re-examined carefully to ensure that the model is capturing the relevant phenomena.

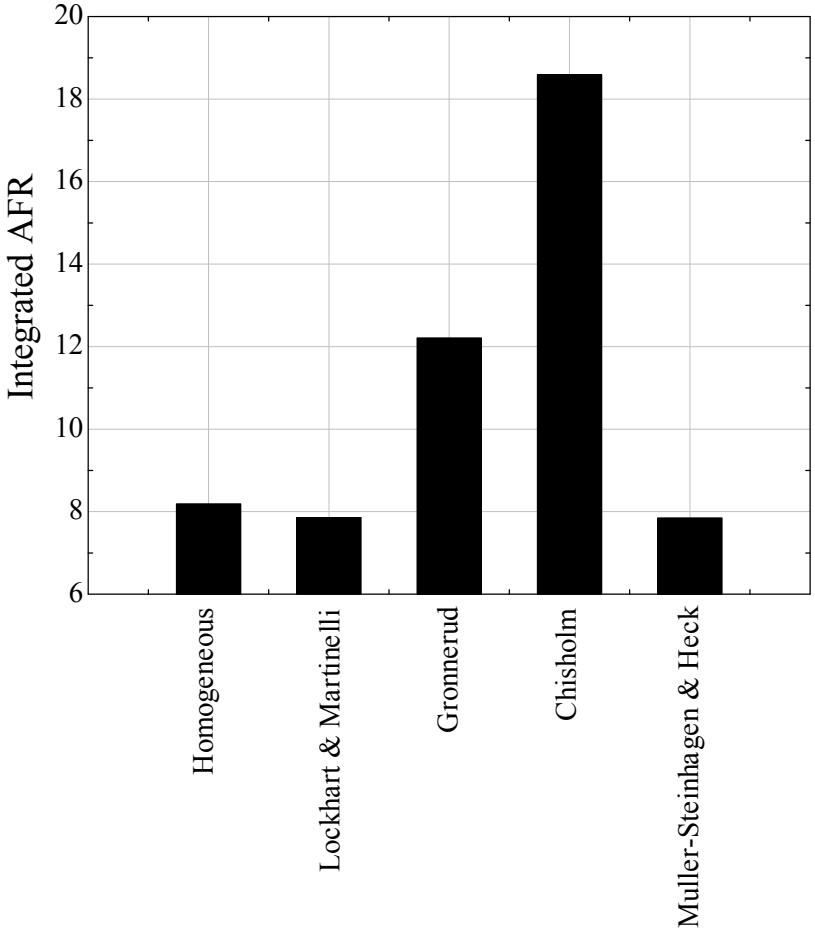

Figure 3.25: Integrated *AFR* for different two-phase flow correlations implemented in the carburetor idle path.

3.8.4 Two-Phase Flow Expansion Loss Models

Of the parameters examined in the sensitivity analysis, the two-phase expansion loss has the second highest impact on the performance so the development of an appropriate model of this component is important in order to correctly predict fuel flow response in the idle circuit. Therefore, several different two-phase expansion loss models were implemented in order to examine the effect on the integrated *AFR*.

First, the expansion loss coefficient was set equal to zero ($k_{tp1,o}$=0), this would imply viscous expansion losses are negligible. The resistance in the two-phase circuit falls dramatically and the fuel flow more than doubles in terms of total flow. This causes

the air-to-fuel ratio to fall to 0.23, indicating an incredibly rich situation that seems very improbable. This observation confirms the existence of a large pressure loss related to sudden expansion into the intake manifold. This result also provides the motivation to examine numerous expansion loss models in more detail.

The expansion loss was implemented using a loss coefficient specified according to [53]

$$K_{tp1o} = \left(1 - \left(\frac{D_{tp1o}^2}{D_{th}^2}\right)\right)^2 \tag{3.69}$$

where D_{th} is the fictitious diameter that represents a very large area for the two-phase flow to empty into. This equation limits to unity when flow is expanding into a large reservoir or plenum, as is the case of the idle path. The results for this model, and others described subsequently below, are presented in Fig. 3.26.

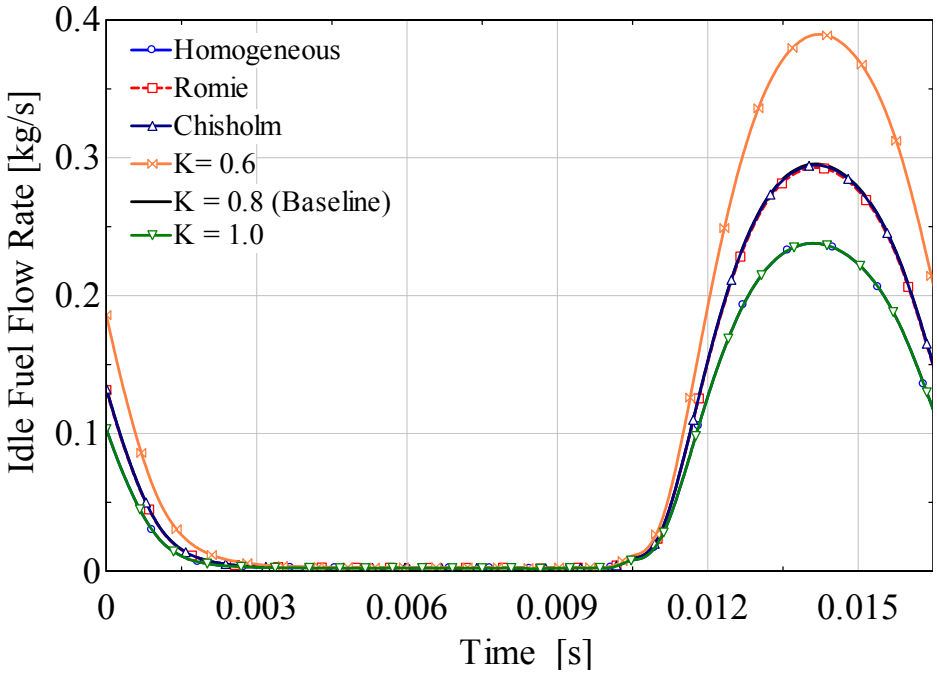

Figure 3.26: Two-phase expansion loss models as implemented in the idle path code. Not shown is the result when the expansion loss coefficient is set equal to zero.

The previous expansion loss models used the homogeneous flow model to describe the interaction of the two phases, as does the model proposed by Romie and described by Collier and Thome [59]. This model ignores wall shear and gravitational forces and focuses on modeling the correct proportion of the kinetic energy recovered in static pressure across an area change. The model also assumes that the void fraction remains constant across the area change.

The last correlation was developed by Chisholm and Sutherland and presented by Collier and Thome [59]. It considers the processes occurring in the orifice before the sudden expansion. The previous correlations presented take a macroscopic approach and are the results of curve fits to experimental data, while this correlation attempts to consider the physics of the actual flow processes.

As seen in Fig. 3.26, the different models produce wide variations in fuel flow and lead to integrated air-to-fuel ratios varying from 5-10. Note that neither of the correlations simulated are exactly appropriate for the idle path process, meaning the orifices tested by the authors (Romie and Chisholm-Sutherland) were much larger than the idle discharge orifice of a typical carburetor, and the fluid mixtures examined were composed of water and air. However, the experiments were conducted at conditions matching those of the idle path, namely the input pressure is close to atmospheric and the mixtures velocities passing through the orifice were comparable to those calculated with the homogeneous model. The results also indicate that a new model correlating expansion pressure loss with fuel and air flow rate is also needed to accurately predict fuel flow in carburetor idle paths.

Chapter 4

Characterization of the Expansion Loss at the Two-Phase Idle Discharge Metering Orifice

The sensitivity analysis performed on the idle path of the carburetor in Chapter 3 indicated that model predictions were extremely sensitive to the two-phase expansion losses; therefore, it is important that the expansion losses be correctly characterized in order to allow accurate prediction of the idle path fuel flow response and the delivered *AFR*. The parametric analysis of the idle path also explored various two-phase flow models found in the literature. It was found the integrated *AFR* that is predicted varies dramatically depending on which of these two-phase flow models are applied to the idle path discharge metering orifice. These observations provide motivation for the experimental work discussed in the chapter which leads to an appropriate correlation for the expansion loss for two-phase flow through a small orifice.

This chapter discusses an experiment that was conducted in order to characterize the pressure drop across the idle discharge orifice. The measured pressure drop is used to develop a correlation which is subsequently compared to published correlations for two-phase metering orifices. From this set of experiments, a general correlation was developed which is based on the homogeneous model with an additional two-phase multiplier. The resulting pressure drop correlation is then applied integrated with the idle path model in order to simulate a small engine carburetor.

4.1 Experimental Setup

Fluid mixtures of air and mineral spirits were tested in a loop which was designed to provide a two-phase expansion into a low pressure plenum (i.e., to reproduce the conditions associated with the two-phase expansion of fuel and air into the intake manifold in the idle path). Mineral spirits was chosen as the working fluid because it has similar density to gasoline and its lower volatility presents less of a fire hazard. Fluid properties for gasoline (also known as isooctane) and mineral spirits (also known as Stoddard Solvent) are presented in Table 4.1.

Table 4.1: Fluid property comparison for Gasoline and Mineral Spirits

	Mineral Spirits	Gasoline
σ [N/m]	0.024	0.021
SG [-]	0.78	0.696
μ [kg/m-s]	0.001195	0.0005821

The pressure loss across the discharge orifice was measured. The experimental setup used to make this measurement is shown schematically in Figure 4.1.

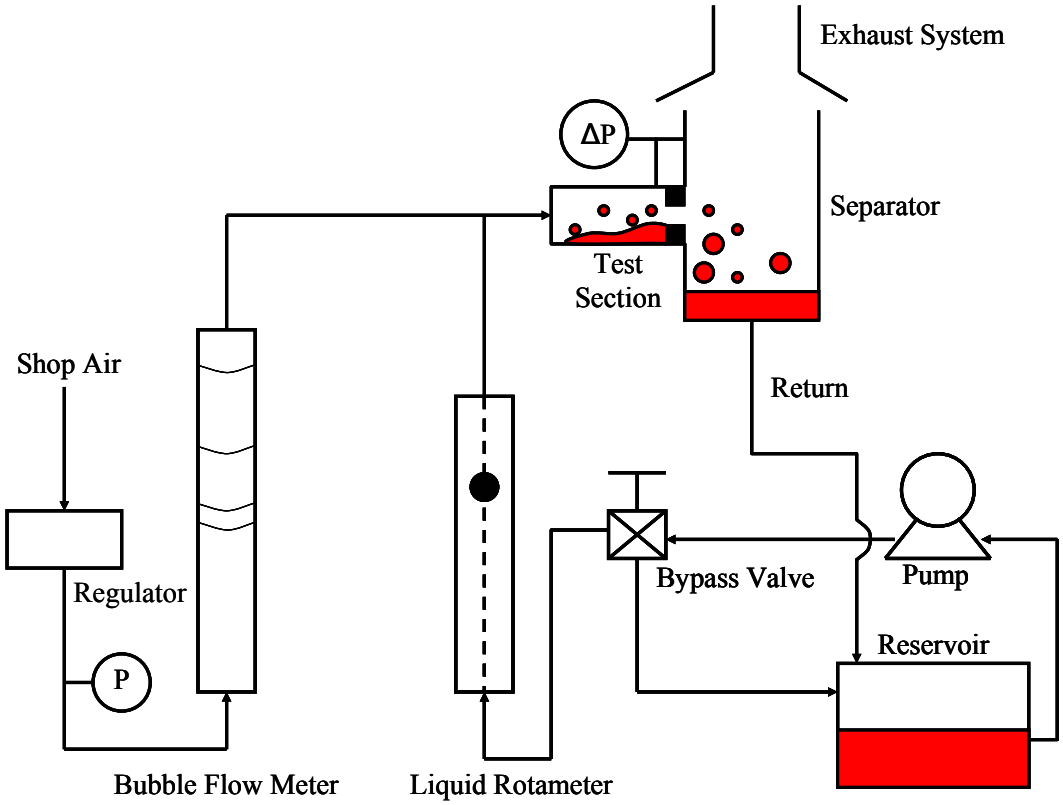

Figure 4.1: Schematic of experimental setup for characterization of orifice loss measurement

4.1.1 Description of Mineral Spirits Loop

Mineral spirits are pumped from a reservoir across a 3-way valve. At the valve, unneeded fluid is returned to the fluid reservoir. The valve is also used to control backpressure on the fluid system and helps dampen oscillations that are otherwise observed in the system. After the valve, the fluid is fed to a Cole-Plamer rotameter (model # PMRI – 010292) in order to measure the flow rate of liquid provided to the test section. The rotameter is a variable area volumetric measurement device that operates on a force balance between the viscous drag force exerted on the float ball and the force of gravity acting in the opposite direction. A correlation for flow rate is provided by the manufacturer with an estimated uncertainty of +/- 2% of full scale.

4.1.2 Description of Air Flow Loop and Bubble Flow Meter

Compressed shop air is brought into the loop, filtered and regulated to the working pressure of the system. The air pressure is measured downstream of the regulator by a Wallace and Tiernan differential pressure gauge (model # FA145) in order to obtain the density of the air. The nominal uncertainty of the air pressure measurement is taken as +/- 338.6 Pa. The pressure measurement is also useful in order to examine fluctuations in the air supply which occur because the building compressed air system is dynamically responding to multiple loads in the building. If a large change in inlet air pressure occurs during a test then the measurement point must be thrown out and then repeated after the fluctuations have damped out. The temperature of both the air and

liquid in the system is assumed to be at room temperature which is measured with a handheld thermocouple meter. The regulated air next enters the bubble flow meter where the volumetric flow rate of air is measured.

The bubble flow meter uses a soap and water mixture to introduce a soap bubble at the bottom of the flow meter which is introduced to the flow through a mixing tee (see Figure 4.2).

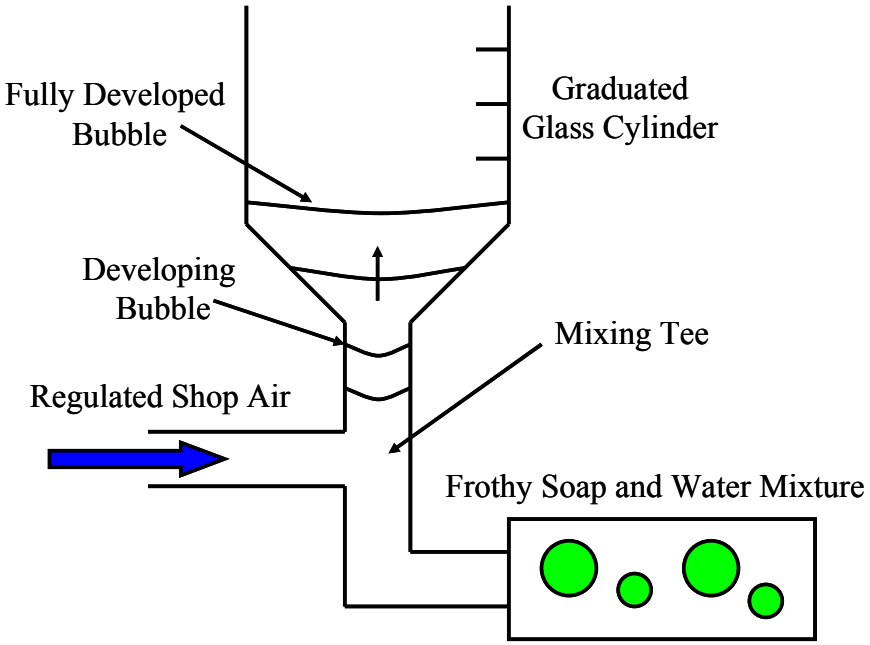

Figure 4.2: Close-up of components used in air flow measurement. Note the mixing tee and the soap and water container are not depicted in the general loop schematic in Figure 4.1.

The bubble that forms across the flow meter segregates different volumes of air in the cylinder. The bubbles develop as they move into the straight portion of the graduated glass cylinder. After the diverging section, the bubbles are fully developed and form nearly straight lines across the cylinder. Upon entering the straight portion of the glass tube the bubble encounters timing marks that are etched into the glass of the cylinder. At this point a time measurement is initiated. When the bubble reaches the end of the

cylinder, the time measurement is stopped and the total time required for the bubble to traverse the cylinder is manually recorded. The cylinder possesses a 500 mL volume with graduations every 5 mL. At the top of the cylinder a sharpened pin penetrates the bubble in order to prevent the soap and water mixture from entering the test section.

The known volume of the glass cylinder together with the time measurement provides a direct measurement of air displacement over a given amount of time provides the average volumetric flow rate of air at a given condition. The method requires no calibration (besides measuring the volume of the cylinder) and the technique tends to increase in accuracy as the flow rate decreases (because the measured time becomes larger). The uncertainty associated with the experimental setup will discussed more thoroughly in Section 4.4.

4.1.3 Two-Phase Test Section and Exhaust System

The air exiting the bubble flow meter is mixed with the liquid exiting the rotameter and the two-phase mixture is fed to the test section. The test section is modular in construction, meaning an orifice plate can be changed without complete disassembly or remanufacturing of the entire test section. The test section also includes optical access for two-phase flow visualization studies. The test section is illustrated schematically in Figure 4.3.

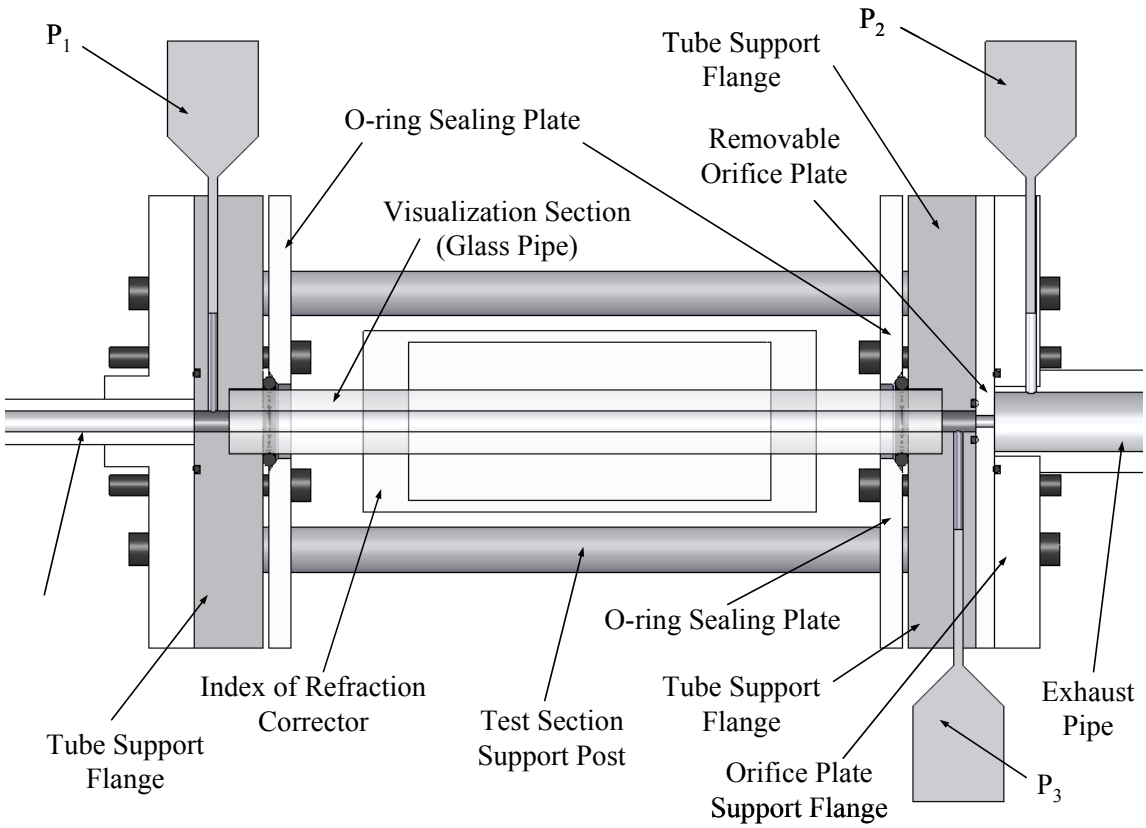

Figure 4.3: Cross section of modular two-phase test section with flow visualization capabilities used in orifice pressure loss characterization

The developing two-phase mixture enters the test section at the mixture inlet shown in Figure 4.3. Before entering the optical section, the mixture is allowed to fully develop in a long pipe (not shown) that is approximately 3 mm in diameter and 100 diameters in length. The mixture then enters the tube support.

The inlet tube support flange includes a radial hole drilled towards the centerline axis that is used to mount a pressure tap (P_1). P_1, and a measurement downstream provided by a second tap (P_2), measure the pressure drop across the flow visualization section which can be used to calculate the frictional pressure gradient along the length of the straight tube. In the experiment described in this thesis, P_1 is not utilized.

Downstream of the inlet tube support flange, the two-phase mixture enters the optical section. A Plexiglas box is mounted around the glass tube; this box can be filled

with a fluid (e.g., vegetable oil) in order to match the index of refraction of the glass. This technique is needed to avoid imaging problems related to the curvature of the glass tube surface. Optical flow visualizations studies were not conducted for this experiment although the optical section was used to make diagnostic observations about the flow conditions present.

At the end of the optical section, the two-phase mixture enters the exit tube support flange. The glass tube is sealed with O-rings that are clamped to the tube supports by the two O-ring sealing plates; this design enables the use of glass tubes without perfectly square ends because the O-rings form a seal around the outer surface of the glass tube rather than the ends of the glass tube. .The two-phase mixture passes through the orifice test plate and finally exits into the exhaust pipe. A third pressure tap (P_3) is mounted in the orifice plate support flange slightly downstream of the metering orifice in the exhaust pipe. Pressure taps P_2 and P_3 are connected to a differential pressure transducer to measure the pressure loss across the metering orifice.

In the exhaust pipe, the two-phase mixture quickly passes into the separator where the force of gravity separates liquid droplets from the air, returning the liquid to the reservoir, and discharging the air to the building exhaust system. Note that during initial testing, it was determined that the building exhaust system applied a time varying backpressure to the system which would affect both liquid and air flow through the test section in an unpredictable and therefore non-repeatable way. This problem was rectified by removing any rigid connection between the experiment and the exhaust system.

The ratio of orifice area to exhaust area is approximately 0.03 for the largest orifice size tested; therefore the test section closely simulates an abrupt expansion into a plenum or reservoir (according to Fox and McDonald [60]) and replicates the phenomenon associated with idle discharge mixture metering into the intake manifold of an engine.

The test section is held together by four support posts which clamp all the tube supports together. The assembly uses O-rings at every sealing surface which enables rapid disassembly to change various characteristics of the test section (for example, the orifice plate). The support posts, commonly known as standoffs, are standardized parts available in 1 inch increments and this allows the glass tube length to be adjusted in 1 inch increments. The orifice plates are simple round thin plates with square edge holes; therefore, tests with different orifice sizes and L/D ratios can be accomplished quickly.

4.2 Data Acquisition

The data acquisition system uses an electronic pressure transducer from Omega Engineering, Inc. (model # PX138-0.35V) to measure the pressure drop across the metering orifice. The measurements made by the pressure transducer are processed by a LabView data reduction program via a 14-Bit NiDAQ card. The program takes 1000 measurements in 10 seconds and then performs a statistical analysis of each data point in order to determine the average and the standard deviation of each voltage measurement. The average voltage is substituted into a calibration curve for the pressure sensor. The resulting pressure differential is then automatically written to a text file for further processing. At each test point, the flow rates of the liquid and air are manually recorded in the LabView program. These values are also written directly to the output text file.

4.3 Test Pieces and Flow Conditions

Five different orifice sizes were tested in this series of experiments. The orifice diameters are listed in Table 4.1.

Table 4.1: Orifice Diameters

Orifice Diameters Tested in mm +/- 0.025 [mm]				
0.5	0.9	1.2	1.4	1.6

The diameters were chosen to correspond to a representative range of idle discharge port hole sizes that can be found in commercial carburetors. The smallest diameter is about the same size as that found in the Briggs & Stratton Intek (BSI) carburetor (see Table 3.1) which is found on small lawn and garden lawnmowers that produce approximately 5 to 8 hp; this is probably close to the smallest metering orifice used for this type of engine. The largest diameter tested is 1.6 mm and this corresponds to the largest size that can be tested accurately in the experiment. An orifice larger than 1.6 [mm] requires highly sensitive pressure sensors to adequately measure pressure drop and due to cost concerns this was deemed unfeasible.

The experimental apparatus allowed a wide range of fluid flow rates and air flow rates to be investigated. For each orifice, air flow rate was varied from 0.1 to 2.75 L/min, while the liquid flow rate varied from 0.01 to 0.5 cm^3/min. The ranges considered were taken from the simulations performed on the BSI carburetor (which again corresponds to the smaller end of the expected conditions) and extended by a factor of 5 in order to generate conditions that are applicable to a wide range of engines. It should be noted that the range of data that was eventually taken for each orifice was limited due to two constraints. First, for smaller orifices, the larger flow rates would provide pressure drops that are larger than the pressure sensor could measure (the range of the differential

pressure sensor is approximately 0-2000 Pa). Secondly, with the larger orifices, the measurement range was limited by the fact that at very high liquid flow rates liquid would actually enter the pressure taps and disrupt the measurement (the pressure sensor is intended for dry applications only). The optical test section and translucent pressure tap bodies allowed inspection of the pressure tap lines to ensure this situation did not occur.

4.4 Experimental Uncertainty Analysis

The expansion loss coefficient for an orifice (k_{loss}) is defined by Equation 4.1 which expresses the pressure drop Δp as a function of the two-phase mixture density ρ_{mix}, the mixture velocity u_{mix}

$$\Delta p = k_{loss} \frac{\rho_{mix} u_{mix}^2}{2} \tag{4.1}$$

Note that the velocity and density in Equation (4.1) are computed assuming homogeneous flow.

Equation 4.1 can be rearranged to solve for the loss coefficient. The uncertainty is presented in terms of a loss coefficient, but the data will be correlated with a two-phase parameter that is a complex function of the liquid flow rate, air flow rate, vapor quality, and viscosities of the two phases. Therefore, the error analysis can be used to suggest an uncertainty associated with the correlation. Absolute uncertainty estimates for each variable in Equation 4.1 are used to solve for the total uncertainty associated with the loss coefficient, δk_{loss}

$$\delta k_{loss} = \sqrt{\left(\frac{\partial k_{loss}}{\partial \rho_{mix}} \delta \rho_{mix}\right)^2 + \left(\frac{\partial k_{loss}}{\partial u_{mix}} \delta u_{mix}\right)^2 + \left(\frac{\partial k_{loss}}{\partial \Delta p} \delta \Delta p\right)^2} \tag{4.2}$$

The absolute uncertainty associated with each variable listed in Equation 4.1 is described in the following sections.

4.4.1 Bubble Flow Meter Uncertainty

Measurements of air and liquid flow rates are needed to calculate the two-phase mixture velocity and the two-phase mixture density. Equation 4.3 describes the uncertainty inherent in the bubble flow meter measurement, which determines the air flow rate.

$$\delta \dot{V}_{air} = \sqrt{\left(\frac{\delta \dot{V}_{air}}{\delta t} \delta t \right)^2 + \left(\frac{\delta \dot{V}_{air}}{\delta V} \delta V \right)^2} \tag{4.3}$$

where δt is the uncertainty of the time measurement taken as +/- 0.1 s, and δV is the uncertainty of the bubble flow meter volume measurement, which is +/- 2.5 mL based on graduations etched into the glass of the bubble flow meter. The bubble flow meter relies on a measurement of the volume traversed in a given time and the time used to displace the aforementioned volume. These two measurements are combined to calculate the volumetric flow rate of air through the system.

4.4.2 Pressure Transducer Uncertainty

The uncertainty in the pressure loss measurement is a function of the method used to calibrate the differential pressure transducer. A calibration curve for the sensor was generated using an inclined manometer which has an uncertainty of approximately 0.01 inH_2O. The signal generated by the differential pressure transducer was collected by a 14-bit data acquisition card. Equation 4.4 and 4.5 represent the uncertainty of the voltage measurement and the uncertainty in the calibration curve for the pressure sensor, respectively.

$$\delta Volt = \frac{Range}{2^{14}} \tag{4.4}$$

$$\delta \Delta p = \sqrt{\left(\frac{\delta \Delta p}{\delta Volt}\delta Volt\right)^2 + \left(\frac{\delta \Delta p}{\delta h}\delta h\right)^2} \tag{4.5}$$

where $\delta Volt$ is the voltage sampling uncertainty, found to be +/- 0.0003 V, and δh is manometer pressure difference reading error, listed as +/- 0.01 inH_2O or +/- 2.5 Pa. These two measures of uncertainty determine the uncertainty of the differential pressure transducer measurement, $\delta \Delta p$, and lead to the total uncertainty of the pressure measurement of +/- 2.5 Pa which shows that all of the uncertainty associated with the pressure measurement is due to the calibration equipment.

Note, two pressure sensors were actually used in the experiment. An Omega Engineering, Inc. differential pressure sensor, model # PX154-001DI, was used to measure pressure at the low end of the experimental range, which is approximately 0 through 241 Pa. The two sensors were calibrated with the same manometer, but the PX154-001DI has better resolution over its measurement range. Therefore, the uncertainty associated with the pressure measurement using the PX138-0.35V sensor is larger, and this value of uncertainty is propagated and used to determine the uncertainty of the entire pressure measurement.

4.4.3 Liquid Flow Rate Uncertainty

The rotameter used to measure the liquid flow rate was initially calibrated for use with water. The uncertainty of this measurement is based on reading the correlated graduations marked on the rotameter body and is estimated as +/- 0.5 one correlated unit. The uncertainty was further modified by a constant to account for the difference in the density of the test fluid and water. For mineral spirits, the correction factor is the square

root of the ratio of fluid densities is equal to 1.13. The equation governing the uncertainty of the liquid volumetric flow rate measurement is given in equation 4.6.

$$\delta \dot{V}_{\min} = 1.19 \sqrt{\left(\frac{\delta \dot{V}_{\min}}{\delta read} \delta read \right)^2} \tag{4.6}$$

where $\delta \dot{V}_{\min}$ is the measurement uncertainty associated with the volumetric flow rate of mineral spirits, and $\delta read$ is the error based on determining the position of the float with respect to the rotameter markings. The total uncertainty associated with the mineral spirits flow rate is +/- 0.0061 cm^3/min, calculated using the highest flow rate.

4.4.4 Orifice Plate Diameter Uncertainty

The orifice plates used in this study were fabricated by a laser cutting machine. The thin steel plates used were burr free and the diameter tolerance was less than +/- 0.001 inch or +/- 2.5e-05 m. An extremely tight tolerance is required on this component because the uncertainty of this dimension is used in a calculation of the orifice area given in equation 4.7.

$$A_o = \frac{\pi D^2}{4} \tag{4.7}$$

where A_o is the orifice area and D_o is the diameter of the orifice. The orifice area is then used to find the mixture average velocity and average mixture density presented in Equation 4.1. The average mixture velocity is calculated according to equation 4.8.

$$u_{mix} = \frac{\dot{V}_{\min} + \dot{V}_{air}}{A_o} \tag{4.8}$$

The uncertainty in the average mixture velocity is calculated with equation 4.9.

$$\delta u_{mix} = \sqrt{\left(\frac{\delta u_{mix}}{\delta \dot{V}_{air}}\delta \dot{V}_{air}\right)^2 + \left(\frac{\delta u_{mix}}{\delta \dot{V}_{\min}}\delta \dot{V}_{\min}\right)^2 + \left(\frac{\delta u_{mix}}{\delta A_o}\delta A_o\right)^2} \tag{4.9}$$

The uncertainty of the mixture velocity is +/- 2.6 m/s for the smallest orifice diameter and +/- 0.17 m/s for the largest orifice representing errors of 10% and 3% respectively.

A homogeneous void fraction can be calculated with Equation 4.10.

$$\alpha = \frac{\dot{V}_{air}}{\dot{V}_{air} + \dot{V}_{\min}} \tag{4.10}$$

The void fraction can then be used to calculate the homogeneous mixture density referenced in equation 4.1.

$$\rho_{mix} = \alpha \rho_{air} + (1-\alpha)\rho_{\min} \tag{4.11}$$

where $\rho_{\min}$ is the density of the mineral spirits, and ρ_{air} is the density of the air. The density of the air entering the two-phase test section is calculated with an assumption of isothermal conditions in the room, where the temperature is taken to be a constant of 300 K with an uncertainty of +/- 5 K and the pressure is measured with a mechanical gauge with an uncertainty of +/- 0.1 inHg which is equivalent to +/- 340 Pa.

The uncertainty associated with the average mixture density calculation is presented in equation 4.12.

$$\delta\rho_{mix} = \sqrt{\left(\frac{\delta\rho_{mix}}{\delta \dot{V}_{\min}}\delta_{\min}\right)^2 + \left(\frac{\delta\rho_{mix}}{\delta \dot{V}_{air}}\delta_{air}\right)^2 + \left(\frac{\delta\rho_{mix}}{\delta P_{inlet}}\delta P_{inlet}\right)^2 + \left(\frac{\delta\rho_{mix}}{\delta T_{room}}\delta T_{room}\right)^2} \tag{4.12}$$

The total uncertainty of the homogeneous mixture density calculations is +/- 0.04 kg/m^3 for the smallest orifice diameter and +/- 0.0064 kg/m^3 for the largest orifice diameter representing errors of 3% and 0.5% respectively.

Equations 4.5, 4.9, and 4.12 are combined to estimate the total uncertainty of the expansion loss coefficient. The uncertainty associated with the expansion loss coefficient calculation is around 6% of its absolute value. The calculated values of the loss coefficient based on the different models found in the literature can range from 2.0 to 20.0, as described in Section 4.4. Therefore, the experimental results will certainly be useful with regard to understanding the actual value of the discharge coefficient.

4.5 Experimental Results

Data was obtained for the range of liquid and air flow rates described in Section 4.3. The measure pressure drop, Δp, was compared to pressure drop data that was collected for single phase air flowing through the orifice plate. Figure 4.4 shows the pressure drop as a function of the volumetric flow rate of air for two-phase flow data (with various values of the liquid flow rate) as well as the single phase air flow date for the 1.19 mm orifice.

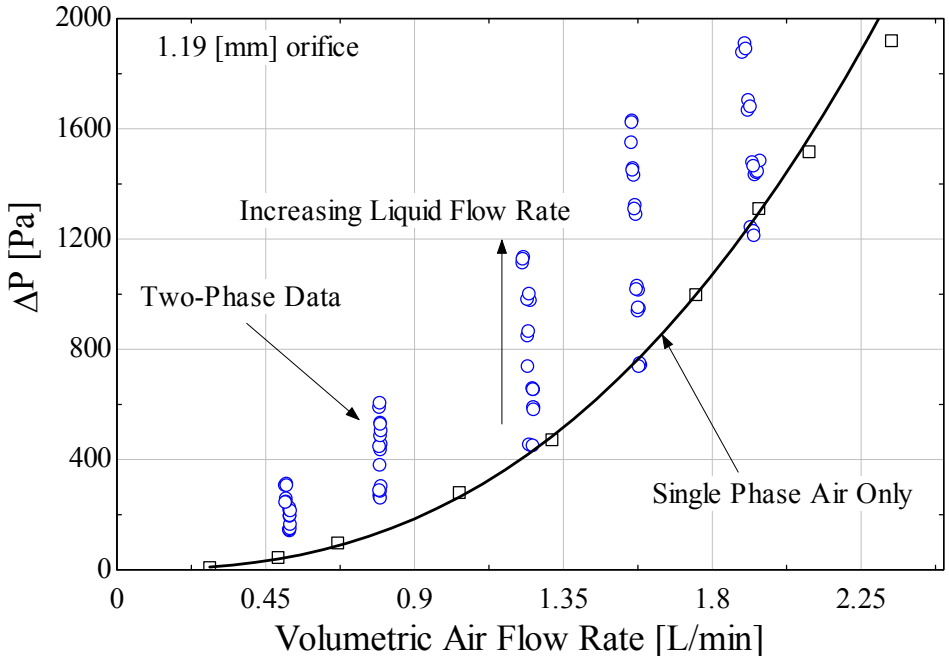

Figure 4.4: Test data for two-phase flow conditions compared with recorded pressure drop for single phase air flow only

Figure 4.4 shows the expected trend of increasing pressure drop when liquid flow rate increases over the entire range of airflow rates tested. The single-phase air flow curve was collected for each orifice plate tested. This data was used to ensure expected functioning of the experimental apparatus. Any data point that fell below the single phase air flow limit was discarded and this operating point was reproduced and collected again. Therefore, while Figure 4.4 was helpful for diagnosing problems with the test facility, it does not provide much insight into the physical processes occurring. Figure 4.5 presents two-phase pressure drop measurements for each of the orifice plates tested as a function of liquid flow rate and various values of the air flow rate.

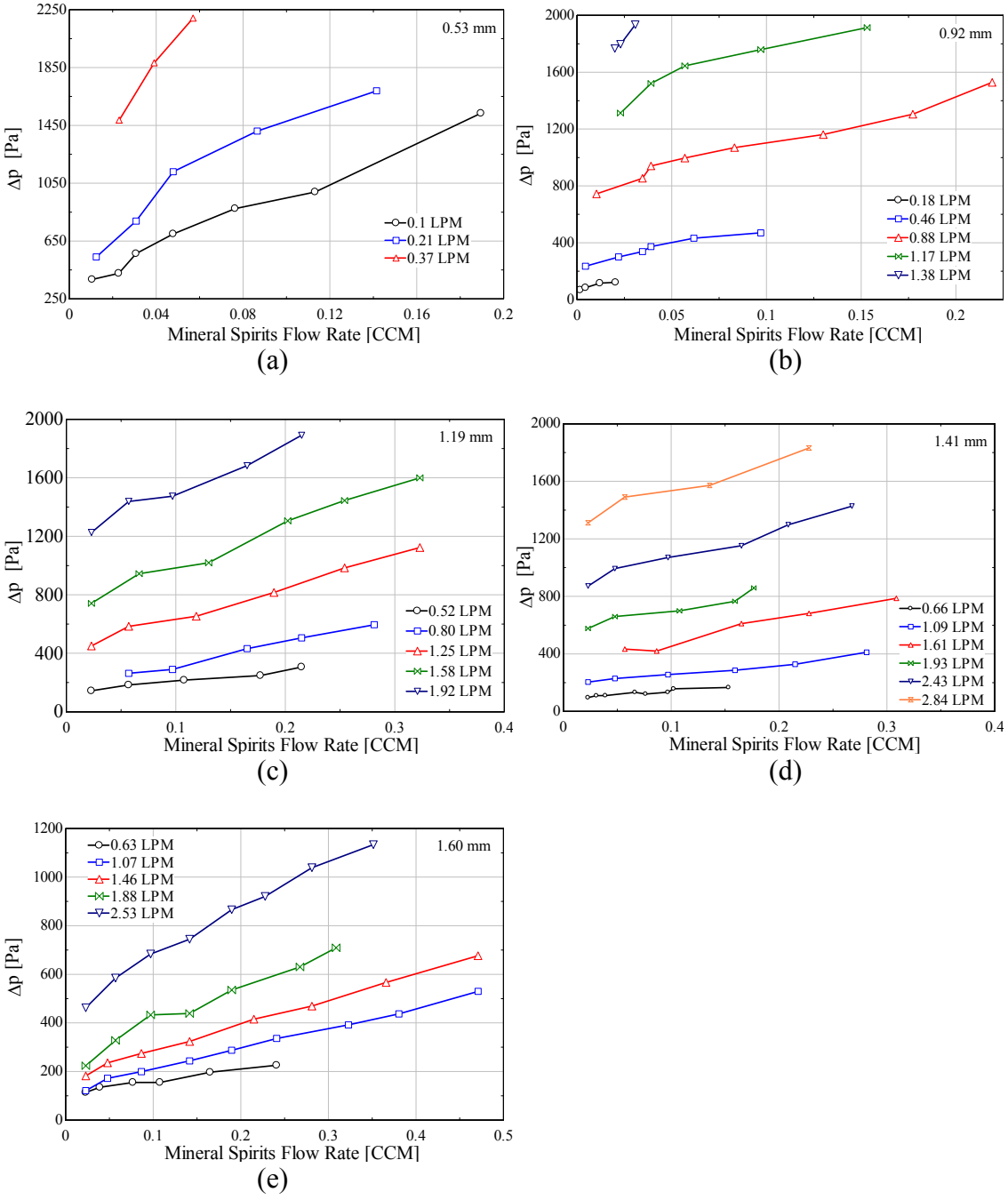

Figure 4.5: Measured pressure drop as a function of liquid flow rate for constant air flow rates with orifice sizes (a) 0.53 mm, (b) 0.92 mm, (c) 1.19 mm, (d) 1.41 mm, and (e) 1.60 mm. Orifice diameter is also identified in the upper right hand corner of each plot.

The plots shown in Figure 4.5 show some interesting trends:

1. At low air flow rates, the pressure drop is almost entirely a function of the air flow rate and not very sensitive to the liquid flow rate (the lines are very shallow).

That is, increases in liquid flow rate do not contribute to the pressure drop as much as increases in air flow. However with the smaller orifices tested (0.53mm and, to a lesser extent, 0.92 mm) even at the lowest air flow rate the pressure drop is very sensitive to the liquid flow rate (i.e., the lines are more vertical). In fact, for the smallest orifice at an air flow rate of only 0.37 LPM the pressure drop is almost completely dependent on the liquid flow rate.

2. For the three larger orifice plates tested (1.19 mm, 1.41 mm, and 1.60 mm), as air flow increases to its maximum rate, the flow regime changes and transitions to a case where the pressure drop is a function of both air and liquid flow rate; increases in either the liquid or air flow rate will yield a proportional increase in pressure drop.
3. The pressure drop for each air flow rate plotted can be described as a linear function of air flow rate above a liquid flow rate of 0.25 CCM.

The pressure drop is plotted as a function of the mixture kinetic energy in Figure 4.6; the assumption of a homogeneous void fraction was used to compute the kinetic energy

$$KE = \frac{\rho_{mix} u_{mix}^2}{2} \tag{4.13}$$

where the mean density and mean velocity of the two fluids are based on the homogeneous model. This implies the two-phases are well mixed and the velocities of the two phases are equal.

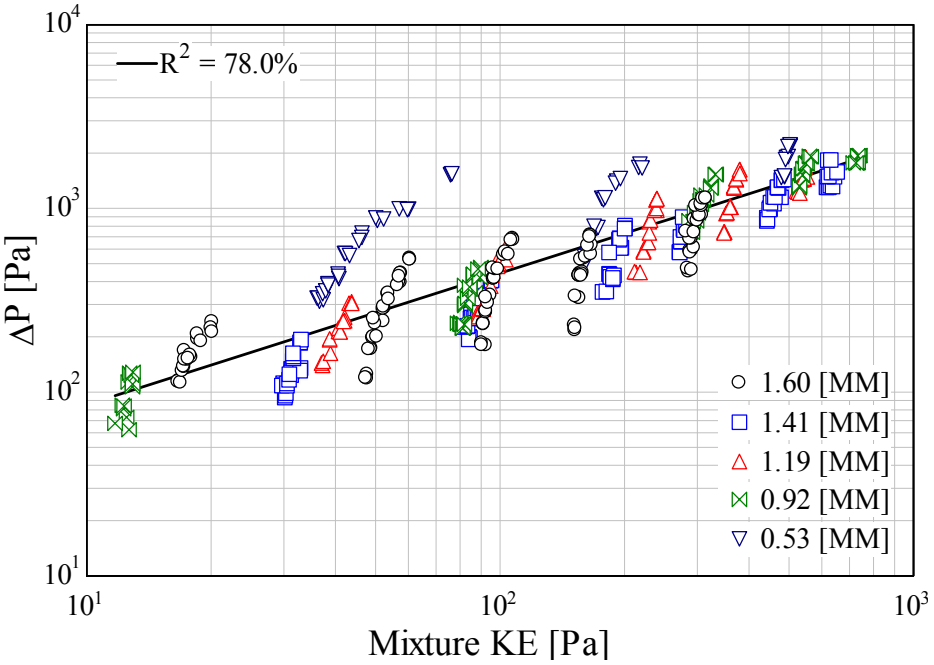

Figure 4.6: Kinetic energy of two-phase mixture for all orifice plates tested as a function of measured pressure drop

Figure 4.6 shows the collected data fit as a function of homogeneous mixture kinetic energy. The equation of the line used to fit the experimental data is

$$\Delta p = 16.8\left(KE\right)^{0.7} \tag{4.14}$$

Figure 4.6 presents all data collected for each orifice plate. However, the figure also indicates that the homogeneous assumption may not be the most appropriate model for the 0.53 mm diameter orifice because the data significantly deviates from Equation 4.14 until higher flow rates are achieved. Secondly, the curve fit fails to fully collapse the data onto a single trend line indicating the need for a better correlation of the void fraction.

It appears that the pressure drop is controlled primarily by air flow rate under most conditions; therefore, it is logical to develop a correlation that describes the single phase air flow pressure drop curve of Figure 4.4 and applies a correction factor for two-

phase phenomena which has the added effect of collapsing the experimental data onto a single trend line. Section 4.6 will discuss the correlation of the experimental data with a two-phase model based on the Lockhart-Martinelli correlating group.

4.6 Data Correlation and Analysis

Ould Didi [61] describes the Lockhart-Martinelli correlation as a two-phase frictional pressure drop model based on a two-phase multiplier for the liquid phase or gas phase. The two phase pressure drop predicted can be described by Equation 4.15.

$$\Delta p_{corr} = \Phi_{LM}^2 \Delta p_{KE} \tag{4.15}$$

where Δp_{KE} is the homogeneous pressure drop based on kinetic energy, Δp_{corr} is the two-phase pressure drop predicted by the correlation, and Φ_{LM} is the two-phase multiplier. The two-phase multiplier is obtained from

$$\Phi_{LM}^2 = 1 + CX_{tt} + X_{tt}^2 \tag{4.16}$$

$$X_{tt} = \left(\frac{1-\chi}{\chi}\right)^{0.9} \left(\frac{\rho_g}{\rho_l}\right)^{0.5} \left(\frac{\mu_l}{\mu_g}\right)^{0.1} \tag{4.17}$$

$$\chi = \frac{\dot{m}_g}{\dot{m}_g + \dot{m}_l} \tag{4.18}$$

where X_{tt} is the Martinelli parameter, χ is the vapor quality, μ_g and μ_l are the dynamic viscosities of the air and liquid, respectively, and C is an empirical constant given as 20 by the authors. Attempts were made to improve the fit of the data by adjusting this constant, and it was found that changing the constant to a value of 30 improved the correlation of the data.

The Lockhart-Martinelli correlation improves the fit of the experimental data to the homogeneous model, as shown in Figure 4.7 for all data sets.

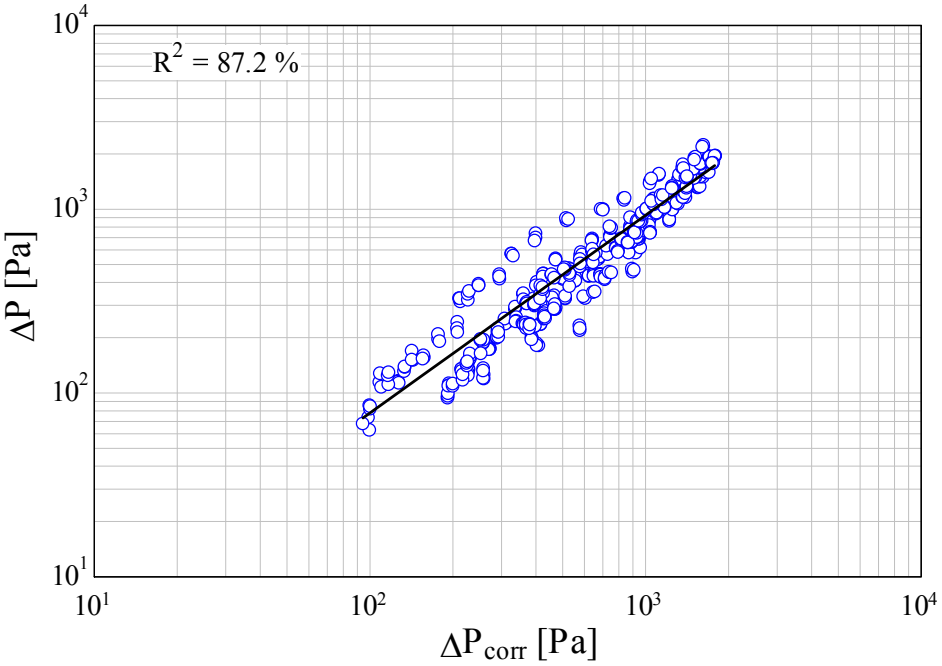

Figure 4.7: Plot of measured pressure drop versus pressure drop predicted by homogeneous mixture kinetic energy combined with a form of the Lockhart-Martinelli two-phase multiplier (Δp_{corr})

The addition of the two-phase multiplier improves the coefficient of determination (R^2) by 9.7%, and the data set further collapses onto the trend line shown in Figure 4.7

The performance of the correlation can also be examined by plotting the experimental data versus the pressure predicted by the correlation on a linear scale (see Figure 4.8). This provides an indication of the correlations applicability to all data sets. The dashed lines indicate % error difference of the pressure predicted by the correlation with respect to the experimental data.

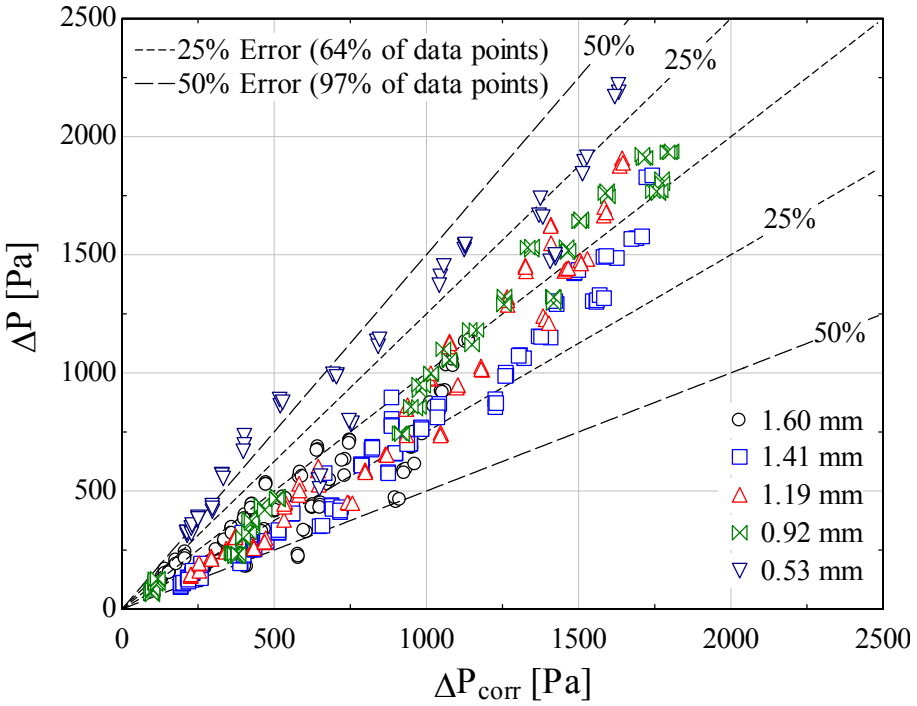

Figure 4.8: Pressure drop predicted by two-phase correlation versus experimental data for small two-phase metering orifices.

The correlation proves adequate to characterize the pressure loss across the metering orifice for orifice diameters of 0.92-1.60 mm. The data for the smallest orifice, 0.53 mm suggests that a homogeneous model of the void fraction and mixture mean velocity is not appropriate. A possible explanation for the breakdown of the homogeneous assumption is provided by Figure 4.5 for the smallest orifice size. For the data taken, the pressure drop appears to be a much larger function of the fluid flow rate as compared to the other cases. The larger orifices seem much less sensitive to fluid flow rate. Therefore, an ideal correlation would be able to differentiate when fluid flow rate effects start to dominate the pressure loss.

In an attempt to better understand the physical phenomena captured by the experiment, the data was broken up into two sets, the first set contained all data from the 0.53 mm and 0.92 mm orifice plates, while the other set contained the rest of the

experimental data. Individual correlations were determined for these data sets and the accuracy of the correlations with respect to the experimental data improved remarkably. This indicated that the length scale associated with the orifice diameter plays a large role in determining the flow regime and therefore the pressure drop. Future work in this area would concentrate on producing not only a better model for the void fraction, but also a correlation that includes diameter effects.

4.7 Correlation Application to Idle Path Model

The Lockhart-Martinelli correlation explained in Section 4.6 was used to model frictional pressure loss in the two-phase region in Section 3.4.8. It is now extended to model the expansion loss at the idle discharge orifice with the correlation developed in Section 4.6. Figure 4.9 displays the resulting fuel flow curve of the idle path with and without the correlation applied.

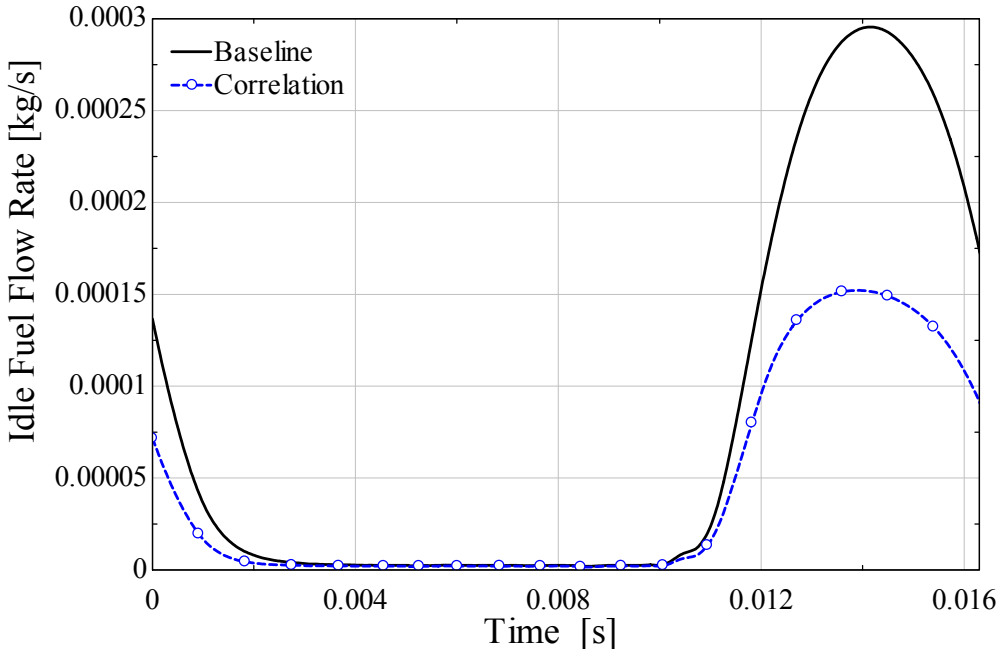

Figure 4.9: Comparison of fuel flow rates predicted with experimentally derived correlation and the baseline configuration tested. The throttle angle was set at 5^{o} and the engine speed was simulated at 900 RPM.

The plot of fuel flow rates in Figure 4.9 indicates a very lean fuel flow rate for the simulation performed with the implemented correlation. The integrated *AFR* for the case ran with the correlation is 14.1 and 7.6 for the baseline case (which assumed a constant loss coefficient at the discharge orifice). The plot also suggests that large errors will result when assuming constant loss coefficients for rapidly changing flow rates.

A comparison can be made between the performance using the new correlation versus the baseline configuration of the model for varying throttle angles. The plot is shown in Figure 4.10 and indicates that the correlation leans the delivered mixture proportionally across the entire range of throttle angles simulated.

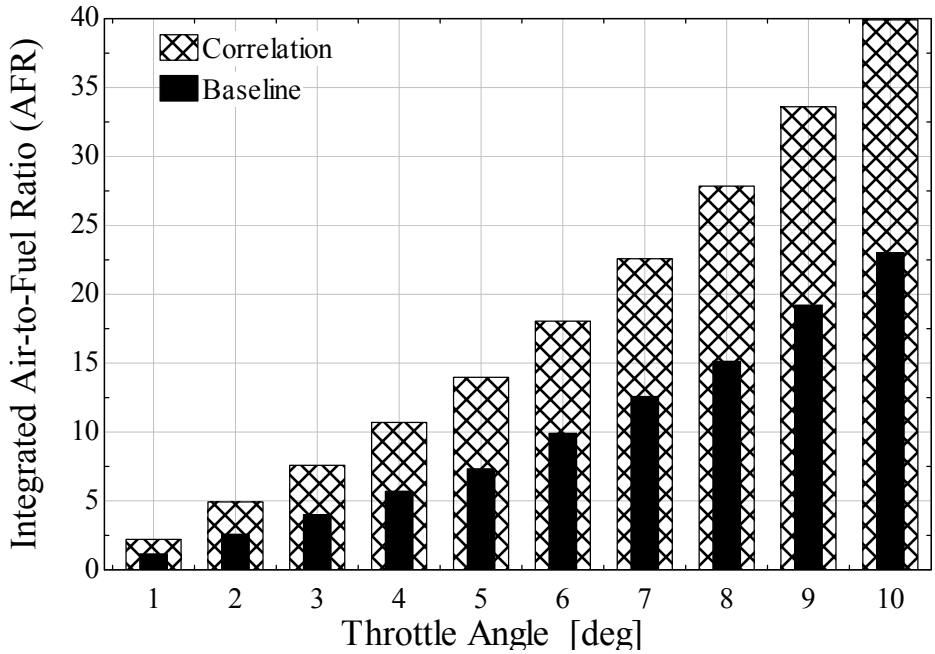

Figure 4.10: Comparison of implemented correlation with baseline configuration for varying throttle angle. Note combustion quality will degrade significantly for *AFR* over approximately 20; this indicates that the idle path system has effectively turned off.

Figure 4.10 shows that the baseline configuration will turn off around a throttle angle of approximately 9^{o}, while an idle path using the developed correlation will turn off around 6.5^{o}. This trend shows that the correct form of the discharge coefficient must be

utilized to realize more precise control of the *AFR*. Lastly, the two figures suggest a transition system needs to be utilized to take control of mixture metering after the idle path has turned off before the main path system turns on as was suggested in Section 2.4.3.

Chapter 5

Conclusions and Suggestions for Future Research

This chapter presents a summary of the research conducted on small engine carburetors with special attention given to metering at idle conditions. The literature review identified several opportunities where research could be conducted that would contribute to the overall understanding of the carburetion process. The closing section also identifies area where future work could be conducted.

5.1 Idle Path Model

The literature review examined the models and experiments currently used to simulate and predict fuel flow in small engine carburetors. Traditional models usually approach the fuel metering problem by establishing steady or quasi-steady engine operating parameters. An unsteady model was produced by Arias [41] incorporating single phase fuel flow effects in the main circuit of the carburetor and wave dynamics in the engine intake system through the use of GT-Power. This model provided an opportunity to study accessory circuits such as the idle and transition system traditionally found in carburetors.

An electrical analogy of the idle path with dimensions similar to current production small engines, incorporating a low speed air-bleed system, was created in MATLAB and used to simulate fuel flow during idle conditions (small throttle angles). Boundary conditions were modeled using input data from GT-Power and other models created in MATLAB. A Runge-Kutta 4^{th} Order integration routine was used to integrate the change in fuel flow over time and LU decomposition was utilized to solve the

resulting stiff set of equations. The baseline results report the intuitive result that the air-to-fuel ratio delivered to the engine becomes progressively leaner as the throttle angle is increased and the driving pressure potential decreases.

The dynamic idle path model captured high speed enrichment effects observed by Moss [33] and numerically simulated in the main path circuit by Arias [41]. A parametric study and sensitivity analysis identified the discharge orifice diameter and loss coefficient used to characterize expansion into the intake manifold as parameters primarily responsible for the control of the fuel delivered under idle conditions. Numerous correlations were tested to simulate expansions losses and these studies produced a wide variation in the air-to-fuel ratio delivered to the engine. This result identified the need for a characterization of the physical phenomena governing the pressure drop across the idle discharge metering orifice.

5.1.1 Transition System Fundamentals

A preliminary investigation was conducted into the process of controlling the air-to-fuel ratio during transition from the idle circuit to the main path metering system. An electrical analogy of the transition system was created by altering the basic layout of the idle path. An additional boundary condition needs to be determined during the transition stage to solve the electrical network and this boundary condition was identified as the pressure at the throat of the nozzle formed by the throttle plate and venturi wall. The pressure constraint at the throttle plate was solved using an optimization routine with the assumption of one-dimensional flow around the throttle plate. Using this methodology it is possible to create a model capable of examining the air-to-fuel ratio delivered to the engine over the entire operating range of a given small engine.

5.1.2 Main Path Model

In order to calculate the pressure following the main jet, a model was created in MATLAB to simulate the main path circuit. The model incorporates fuel flow inertial effects and mathematically simplifies the events occurring in the fuel well and emulsion tube through the use of pressure constraints imposed on the emulsion tube. The pressure constraints control the admission of bleed air into the emulsion tube by adjusting the emulsion tube hole metering area. The new model, named the SIMPLE model, generated fuel flow response curves similar to results produced by the Arias (DYN) model. Confident the SIMPLE model was capturing all relevant fuel flow inertial effects, the pressure after the main jet was utilized to specify the fuel side pressure boundary condition in the idle path model.

5.2 Experimental Characterization of Two-Phase Metering Orifices

The idle discharge metering orifice was identified in the sensitivity analysis of the idle path as an element primarily responsible for the air-to-fuel ratio delivered to the engine. An experiment was designed to simulate the two-phase discharge process using mineral spirits and compressed air. The flow rates of the two fluids were measured along with the differential pressure change across the orifice. The experimental data was reduced and correlated. The correlation was implemented into the idle path model and leaned out the delivered air-to-fuel ratio across the throttle angle range associated with idle path operation. However, the correlation also showed that the data is not well

correlated when a homogeneous assumption is used to model the void fraction of the two-phase flow and orifice diameter is not directly accounted for in the correlation.

5.3 Recommendations for Future Work

A main focus of this study was creating a model that simulated the fuel delivery process in the idle path. The methodology and basic results generated by this work could be extended to incorporate the idle path model into the GT-Power environment. This model, coupled with the main path model produced by Arias [41], would produce a more complete map of the air-to-fuel ratio delivered to the engine under all engine operating conditions.

Secondly, the main path model and the idle path were simulated during this study as discreet, uncoupled systems. In reality, the idle path and main path interact and a more advanced model that combines the two systems would provide a clearer picture of the fuel delivery process.

A more advanced model of the idle path would also include a complete transition system. The methodology described in this work provides a simple way to incorporate the features of a generic transition system into a future model. A fundamental study of the system response and the role of the transition air-bleed system could then be undertaken.

The SIMPLE main path model, originally created to model the pressure boundary after the main jet, demonstrated an adequate ability to predict main path fuel flow and effectively captures the inertial effects of the single phase fuel system at WOT. Further development of the SIMPLE model would first examine part load operation to ensure correct prediction of fuel flow over the entire cycle. Secondly, a more complete study of

the air-bleed prediction given by the SIMPLE model needs to be undertaken to address the effects of the approximations made in the model implementation.

Lastly, the experiment conducted was used to characterize the pressure loss across the idle discharge metering orifice, which effectively simulates expansion into the engine manifold. However the resulting trends showed competing effects that could not be effectively correlated by a simple homogeneous model. Future work would examine different correlations that could be used to model the void fraction and account for the diameter effects seen in the data.

Appendix A

Idle Path Carburetor Model

A.1 MATLAB Code: BSI_Geometry.m

```
%This script sets up the vector geometry that characterizes the details of BSI Engine Carburetor

geometry(1)=1;                  %specifies geometric configuration (-)
geometry(2)=2;                  %number of holes at two-phase discharge, ntpo (-)
geometry(3)=0.00053;            %diameter of holes at two-phase discharge, Dtpo (m)
geometry(4)=0.8;                 %discharge coefficient of two-phase discharge holes, Cdtpo (-)
geometry(5)=0.0016;             %diameter of two-phase section, Dtp1 (m)
geometry(6)=0.023;               %length of two-phase section, Ltp1 (m)
geometry(7)=0.00001;            %roughness in two-phase section, ktp1 (m)
geometry(8)=0.5;                 %discharge coefficient of entrance to air section, Cdap (-)
geometry(9)=0.00001;             %roughness of air section, kap (m)
geometry(10)=0.0127;            %length of air section, Lap (m)
geometry(11)=0.0023;            %diameter of air section, Dap (m)
geometry(12)=0.8;               %discharge coefficient of idle air bleed orifice , Cdapo (-)
geometry(13)=0.000838;          %diameter of orifice connecting air to mixing zone, Dao (m)
geometry(14)=0.000889;          %diameter of 1st fuel section, Df1 (m)
geometry(15)=0.0215;             %length of 1st fuel section, Lf1 (m)
geometry(16)=0.00001;           %roughness of 1st fuel section, kf1 (m)
geometry(17)=pi*0.00739^2/4;     %area of fuel metering valve, Afv (m^2)
geometry(18)=0.7;               %discharge coefficient of fuel section valve, Cdfv (-)
geometry(19)=0.00149;            %diameter of 2nd fuel section, Df2 (m)
geometry(20)=0.0114;             %length of 2nd fuel section, Lf2 (m)
geometry(21)=0.00001;            %roughness of 2nd fuel section, kf2 (m)
```

A.2 MATLAB Code: GtoR.m

```
function[R_fi,In_fi,R_ap,R_tp1]=GtoR1(geometry,mdot_fi,mdot_ap)

% [R_fi,In_fi,R_ap,R_tp1]=GtoR1(geometry,mdot_fi,mdot_ap)

%This function determines the characteristic resistance and inertial values for idle path
%configuration #1 given details of the geometry and the instantaneous mass flow rates

%Idle path configuration #1 consists of a single-phase fuel section, a single-phase air section, and
%a two-phase section.

%The single-phase fuel section is fed from the fuel well pressure (P_mj in Pa) and
%is characterized by a resistance (R_fi in Pa-s/kg) and inertial term (In_fi in Pa-s^2/kg).
%The single-phase air section is fed from the upstream venturi pressure (Pupv in Pa) and is
%characterized by a resistance (R_ap in Pa-s/kg).
%The two-phase section empties through a single hole to the manifold pressure (Pman in Pa)
%and is characterized by a resistance (R_tp1 in Pa-skg)

%The inputs to the function are:
```

```
% geometry - a vector of geometric information.  The protocol for this vector depends on the
% specific geometric configuration.  Geometric configuration is the first element of the
% vector geometry.
% mdot_fi - instantaneous mass flow rate of fuel (kg/s)
% mdot_ap - instantaneous mass flow rate of air (kg/s)

%The outputs to the function are:
% R_fi - resistance of fuel section (Pa-s/kg)
% In_fi - inertia of fuel section (Pa-s^2/kg)
% R_ap - resistance of air section (Pa-s/kg)
% R_tp1 - resistance of two-phase section (Pa-s/kg)

%fluid properties
rhoa=1.1;          %nominal air density (kg/m^3)
mua=0.000019;   %nominal air viscosity (Pa-s)
rhof=769;          %nominal fuel density (kg/m^3)
muf=0.00058;     %nominal fuel viscosity (Pa-s)

%case statement to detect the geometric configuration
switch (geometry(1))
   case(1)
      %geometry #1 - consistent with Briggs & Stratton Intek Engine Carburetor

      %this configuration includes two fuel sections separated by a valve, a single air
      %section with an entrance loss and an orifice, and a single two-phase section emptying
      %to the same throttle pressure through multiple holes
      ntpo=geometry(2);              %number of holes at two-phase discharge, ntpo (-)
      Dtpo=geometry(3);              %diameter of holes at two-phase discharge, Dtpo (m)
      Cdtpo=geometry(4);             %discharge coefficient of two-phase discharge holes, Cdtpo (-)
      Dtp1=geometry(5);              %diameter of two-phase section, Dtp1 (m)
      Ltp1=geometry(6);              %length of two-phase section, Ltp1 (m)
      ktp1=geometry(7);              %roughness in two-phase section, ktp1 (m)
      Cdap=geometry(8);              %discharge coefficient of entrance to air section, Cdap (-)
      kap=geometry(9);               %roughness of air section, kap (m)
      Lap=geometry(10);               %length of air section, Lap (m)
      Dap=geometry(11);              %diameter of air section, Dap (m)
      Cdapo=geometry(12);             %discharge coefficient of idle air bleed orifice, Cdapo (-)
      Dapo=geometry(13);             %diameter of orifice connecting air to mixing zone, Dapo (m)
      Df1=geometry(14);              %diameter of 1st fuel section, Df1 (m)
      Lf1=geometry(15);              %length of 1st fuel section, Lf1 (m)
      kf1=geometry(16);              %roughness of 1st fuel section, kf1 (m)
      Afv=geometry(17);              %area of fuel section valve, Afv (m^2)
      Cdfv=geometry(18);             %discharge coefficient of fuel section valve, Cdfv (-)
      Df2=geometry(19);              %diameter of 2nd fuel section, Df2 (m)
      Lf2=geometry(20);              %length of 2nd fuel section, Lf2 (m)
      kf2=geometry(21);              %roughness of 2nd fuel section, kf2 (m)

      mdot_a_min=1e-4;               %minimum allowable air mass flow rate (kg/s)
      mdot_f_min=1e-4;               %minimum allowable fuel mass flow rate (kg/s)
      if(mdot_ap<mdot_a_min)
         mdot_ap=mdot_a_min;         %set a lower bound on mdot_ap to prevent singularities
      end
      if(mdot_fi<mdot_f_min)
         mdot_fi=mdot_f_min;         %set a lower bound on mdot_fi to prevent singularities
      end
```

```
%air section resistance
Aa=pi*Dap^2/4;              %area of air section (m^2)
va=mdot_ap/(rhoa*Aa);       %velocity in air section (m/s)
Rea=va*Dap*rhoa/mua;        %Reynolds number in air section
if(Rea<100)
   fa=0.64;                 %set f to a constant if Reynolds number drops towards zero
else
   if(Rea<3000)
      fa=64/Rea;            %assume laminar flow
   else
      fa=(0.790*log(Rea)-1.64)^(-2);     %turbulent flow, smooth tube
   end
end
Aao=pi*Dapo^2/4;            %area of orifice connecting air section to mixing zone (m^2)
vao=mdot_ap/(rhoa*Aao);      %velocity of air in orifice (m/s)
DPa=(rhoa*va^2)*(fa*Lap/Dap+Cdap)/2+rhoa*vao^2*Cdapo/2;   %pressure drop across air section
R_ap=DPa/mdot_ap;           %resistance of air section (Pa-s/kg)

%fuel section resistance
Af1=pi*Df1^2/4;             %area of 1st fuel section (m^2)
vf1=mdot_fi/(rhof*Af1);     %velocity in 1st fuel section (m/s)
Ref1=vf1*Df1*rhof/muf;      %Reynolds number in 1st fuel section
if(Ref1<100)
   ff1=0.64;                %set f to a constant if Reynolds number drops towards zero
else
   if(Ref1<3000)
      ff1=64/Ref1;          %assume laminar flow
   else
      ff1=(0.790*log(Ref1)-1.64)^(-2);  %turbulent flow, smooth tube
   end
end
vfv=mdot_fi/(rhof*Afv);     %velocity of fuel in valve (m/s)
Af2=pi*Df2^2/4;             %area of 2nd fuel section (m^2)
vf2=mdot_fi/(rhof*Af2);     %velocity in 2nd fuel section (m/s)
Ref2=vf2*Df2*rhof/muf;      %Reynolds number in 2nd fuel section
if(Ref2<100)
   ff2=0.64;                %set f to a constant if Reynolds number drops towards zero
else
   if(Ref2<3000)
      ff2=64/Ref2;          %assume laminar flow
   else
      ff2=(0.790*log(Ref2)-1.64)^(-2);   %turbulent flow, smooth tube
   end
end
DPf=(rhof*vf1^2)*(ff1*Lf1/Df1)/2+rhof*vfv^2*Cdfv/2+(rhof*vf2^2)*(ff2*Lf2/Df2)/2; %pressure
drop across fuel section (Pa)
R_fi=DPf/mdot_fi;           %resistance of fuel section (Pa-s/kg)

%two-phase section
alpha=abs(mdot_ap/rhoa)/(abs(mdot_fi/rhof)+abs(mdot_ap/rhoa)); %void fraction
rhotp=alpha*rhoa+(1-alpha)*rhof;      %mean density  based on void fraction
mutp=alpha*mua+(1-alpha)*muf;         %mean viscosity based on void fraction
Atp=pi*Dtp1^2/4;            %area of two-phase section (m^2)
vtp=abs(mdot_fi+mdot_ap)/(rhotp*Atp);          %velocity of two-phase mixture (m/s)
Retp=vtp*Dtp1*rhotp/mutp;   %Reynolds number in two-phase section
if(Retp<100)
```

```
        ftp=0.64;                    %set f to a constant if Reynolds number drops towards zero
    else
        if(Retp<3000)
            ftp=64/Retp;             %assume laminar flow
        else
            ftp=(0.790*log(Retp)-1.64)^(-2);   %turbulent flow, smooth tube
        end
    end
    Atpo=ntpo*pi*Dtpo^2/4;       %area of discharge holes from two-phase section (m^2)
    vtpo=abs(mdot_ap+mdot_fi)/(Atpo*rhotp); %velocity of two-phase mixture in discharge holes (m/s)
    DPtp=Cdtpo*rhotp*vtpo^2/2+rhotp*vtp^2*(ftp*Ltp1/Dtp1)/2;      %pressure drop across two-phase
    section (Pa)
    R_tp1=DPtp/(abs(mdot_fi)+abs(mdot_ap));       %resistance of two-phase section (Pa-s/kg)

    %inertia of fuel section
    In_fi=(Lf1/Af1+Lf2/Af2); %inertia of fuel (Pa-s^2/kg)

  otherwise
    'Error - geometry configuration is not recognized'
end
```

A.3 MATLAB Code: Stder.m

```
function[dmdotfidt,mdot_ap]=stder1(Pupv,Pmj,Pman,mdot_fi,R_fi,In_fi,R_ap,R_tp1)

%[dmdotfidt,mdot_ap]=stder1(Pupv,Pmj,Pman,mdot_fi,R_fi,In_fi,R_ap,R_tp1)

%This function computes the rate of change of the fuel flow rate through idle path configuration #1
%Idle path configuration #1 consists of a single-phase fuel section, a single-phase air section, and
%a two-phase section.

%The single-phase fuel section is fed from the fuel well pressure (Pmj in Pa) and
%is characterized by a resistance (R_fi in Pa-s/kg) and inertia (In_fi in Pa-s^2/kg).
%The single-phase air section is fed from the venturi pressure (Pupv in Pa) and is
%characterized by a resistance (R_ap in Pa-s/kg).
%The two-phase section empties through a single hole to the throttle pressure (Pman in Pa)
%and is characterized by a resistance (R_th in Pa-skg)

%The inputs to the function are:
% Pupv - venturi pressure (Pa)
% Pmj - fuel well pressure (Pa)
% Pman - throttle pressure (Pa)
% mdot_fi - fuel mass flow rate (kg/s)
% R_fi - resistance of fuel section (Pa-s/kg)
% In_fi - inertance of fuel section (Pa-s^2/kg)
% R_ap - resistance of air section (Pa-s/kg)
% R_tp1 - resistance of two-phase section (Pa-s/kg)
%
%The outputs from the function are:
% dmdotfidt - the rate of change of the fuel flow rate (kg/s^2)
% mdot_ap - the air flow rate (kg/s)

% Setup the constitutive and constraint equations in matrix form A*X=b
% where X=[P_i1, P_i2, mdot_ap, mdot_tp1, dmdotfidt]
% Eq. 1: constitutive equation for fuel resistance (P_i1-P_i2)=mdot_fi*R_fi
```

```
A(1,1)=1;
A(1,2)=-1;
b(1,1)=mdot_fi*R_fi;
% Eq. 2: constitutive equation for air resistance (Pupv-P_i2)=mdot_ap*R_ap
A(2,2)=1;
A(2,3)=R_ap;
b(2,1)=Pupv;
% Eq. 3: constitutive equation for two-phase resistance (P_i2-Pman)=mdot_tp1*R_tp1
A(3,2)=1;
A(3,4)=-R_tp1;
b(3,1)=Pman;
% Eq. 4: constraint equation for mixing zone mdot_fi+mdot_ap=mdot_tp1
A(4,3)=1;
A(4,4)=-1;
b(4,1)=-mdot_fi;
% Eq. 5: constitutive equation for the inertia Pmj-P_i1=In_fi*dmdotfidt
A(5,1)=1/In_fi;
A(5,5)=1;
b(5,1)=Pmj/In_fi;
%Decompose matrix
[L,U]=lu(A);
Y=inv(L)*b;
dmdotfidt=Y(5)/U(5,5);
mdot_tp1=(Y(4)-U(4,5)*Y(5)/U(5,5))/U(4,4);
mdot_ap=mdot_tp1-mdot_fi;
```

A.4 MATLAB Code: Idlepath.m

```
function[mdot_fi,mdot_ap]=idlepath1(mdot_fiold,Pupv,Pmj,Pman,Dt,mdot_apold,geometry)

%[mdot_fi,mdot_ap]=idlepath1(mdot_fiold,Pmj,Pman,Pupv,Dt,mdot_apold,geometry)

%This function computes the fuel flow rate and air flow rate through idle path configuration #1 at
%the end of a timestep of specified duration.
%Idle path configuration #1 consists of a single-phase fuel section, a single-phase air section, and
%a two-phase section.

%The single-phase fuel section is fed from the fuel well pressure (Pmj in Pa) and
%is characterized by a resistance and inertia
%The single-phase air section is fed from the venturi pressure and is
%characterized by a resistance.
%The two-phase section empties through a single hole to the throttle pressure (Pman in Pa)
%and is characterized by a resistance.

%The specific resistance and inheritance values depend on the details of the geometry
%This function can deal with a number of geometries provided the overall configuration
%is consistent with idle path configuration #1 described above

%The inputs to the function are:
% mdot_fiold - mass flow rate of fuel at the beginning of the timestep (kg/s)
% Pupv - static pressure upstream of venturi(Pa)
% Pmj - fuel well pressure (Pa)
% Pman - throttle pressure (Pa)
% mdot_apold - air mass flow rate at the beginning of the timestep (kg/s)
% geometry - vector containing the details associated with the geometry
```

```
%The outputs from the function are:
% mdot_fi - the fuel flow rate at the end of the timestep (kg/s^2)
% mdot_ap - the air flow rate at the end of the timestep (kg/s)

%use geometry and current conditions to predict the resistance and inertia values of the circuit
[R_fi,In_fi,R_ap,R_tp1]=GtoR1(geometry,mdot_fiold,mdot_apold);

N=5;                %number of timesteps to divide Dt into
Dtl=Dt/N;           %timesteps for integration process (s)
for i=1:N
  [dmdotfdt1,mdot_ap]=stder1(Pupv,Pmj,Pman,mdot_fiold,R_fi,In_fi,R_ap,R_tp1);
  [dmdotfdt2,mdot_ap]=stder1(Pupv,Pmj,Pman,mdot_fiold+dmdotfdt1*Dtl/2,R_fi,In_fi,R_ap,R_tp1);
  [dmdotfdt3,mdot_ap]=stder1(Pupv,Pmj,Pman,mdot_fiold+dmdotfdt2*Dtl/2,R_fi,In_fi,R_ap,R_tp1);
  [dmdotfdt4,mdot_ap]=stder1(Pupv,Pmj,Pman,mdot_fiold+dmdotfdt3*Dtl,R_fi,In_fi,R_ap,R_tp1);
  mdot_fiold=mdot_fiold+Dtl*(dmdotfdt1+2*dmdotfdt2+2*dmdotfdt3+dmdotfdt4)/6;
end
mdot_fi=mdot_fiold;
```

A.5 MATLAB Code: Runidlepath.m

```
[N,g]=size(timev);
clear mdot_fi;
clear mdot_ap;
mdot_fi(1,1)=0.001;
mdot_ap(1,1)=0.0001;
tol=0.000001;
done=0;
BS_Intek_Engine;
while(done==0)
  for i=1:(N-1)
        [mdot_fi(i+1,1),mdot_ap(i+1,1)]=idlepath1(mdot_fi(i,1),Pupv(i),Pmj(i),Pman(i),(timev(i+1)-
timev(i)),mdot_ap(i,1),geometry);
  end
  err=abs(mdot_fi(N)-mdot_fi(1))
  if(err<tol)
    done=1;
  else
    mdot_fi(1)=mdot_fi(N);
    mdot_ap(1)=mdot_ap(N);
  end
end
```

Appendix B

Nominal Engine Specifications Needed to Run GT-Power

B.1 BSI Engine Characteristics

Description	Value
displacement	190 [cm^3]
bore	0.068 [m]
stroke	0.0518 [m]
intake runner length	0.0254 [m]
intake runner diameter	0.0254 [m]
intake port length	0.0254 [m]
intake port diameter	0.0254 [m]
inlet valve diameter	0.0254 [m]
diameter of air section	0.0023 [m]
intake valve closing angle	-86 [deg]
venturi throat diameter	0.0127 [m]
venturi inlet diameter	0.0254 [m]
throttle body Diameter	0.019 [m]

Appendix C

SIMPLE Main Path Model

C.1 MATLAB Code: Nikki_Geometry.m

```
%This script sets up the geometry vector that characterizes the main path
%of the Nikki Carburetor

geometry(1)=1;          %specifies geometric configuration
geometry(2)=0.025;      %venturi throat diameter, Dvt (m)
geometry(3)=0.038;      %venturi inlet diameter, Dvin (m)
geometry(4)=0.02175;    %venturi throttle bore diameter, Dvt (m)
geometry(5)=0.95;       %discharge coefficent for venturi,Cdv (-)
geometry(6)=0.00001;    %wall roughness in venturi, Kv (-)
geometry(7)=0.002;      %main jet size, Dmj (m)
geometry(8)=0.7;        %discharge coefficient of main jet, Cdmj (-)
geometry(9)=0.006;      %diameter of single phase fuel path, Dsp (m)
geometry(10)=0.03;      %distance from beginning of emulsion tube to first air bleed hole, Lsp (m)
geometry(11)=0.00001;   %wall roughness of emulsion tube, Ksp (m)
geometry(12)=0.01;      %distance from first emulsion tube hole to second hole, Let1 (m)
geometry(13)=0.01;      %distance from second emulsion tube hole to third hole, Let2 (m)
geometry(14)=0.01;      %distance from third emulsion tube hole to nozzle discharge, Let3 (m)
geometry(15)=0.006;     %diameter of emulsion tube (if different from single phase fuel tube, Det (m)
geometry(16)=0.001;     %diameter of first set of emulsion tube holes, Det1 (m)
geometry(17)=0.001;     %diameter of second set of emulsion tube holes, Det2 (m)
geometry(18)=0.001;     %diameter of third set of emulsion tube holes, Det3 (m)
geometry(19)=0.2;       %discharge coefficient for emulsion tube holes, Cdet
geometry(20)=1;         %number of holes for each level of emulsion tube holes, nem (-)
geometry(21)=0.003;     %diameter of main air bleed, Dap (m)
geometry(22)=0.5;       %loss coefficient of main air path (expansion loss), kap (-)
geometry(23)=0.00001;   %wall roughness in single phase air path, Kap (m)
geometry(24)=0.050;     %length of main air bleed path, Lap (m)
geometry(25)=0.001;     %diameter of air bleed orifice, Daj (m)
geometry(26)=0.7;       %discharge coefficient of air bleed orifice, Cdaj (-)
geometry(27)=0.04;      %height of fuel level in bowl, hbowl(m)
```

C.2 MATLAB Code: GtoRmain.m

```
%Calculation of the resistance and inertia and of the main fuel delivery system

function[Rmj,In_fm,Rsp,In_ap,Rap,Rtp,Pvt]=GtoR1main(geometry,mdot_fm,mdot_ap,mdot_tp,Pmj,Psp,P
et,Paj,CA,Pupv,Pfbb,Po,To,mdot_engine,Pvt)

%The inputs to this function are :
%geometry - geometry vector
%mdot_fm - mass flow rate of fuel
%mdot_ap - mass flow rate of bleed air
%mdot_tp - mass flow rate of two-phase flow
%Pmj - Pressure after the main jet
```

```
%Psp - Pressure after the single phase fuel section
%Pet - Pressure at the two-phase mixing zone (i.e. expandable orifice)
%Paj - Pressure after the air jet
%CA - crank angle
%Pupv - pressure upstream of the venturi
%Pfbb - pressure at the bottom of the float bowl
%Po - stagnation pressure
%To - stagnation temperature
%mdot_engine - engine mass air flow rate
%Pvt - pressure at the throat of the venturi (used for comparison with fzero routine result)

%The outputs to the function are:
%Rmj - resistance of main jet
%Rsp - resistance of single phase fuel section (Pa-s/kg)
%In_fm - inertial term of single phase fuel flow region (Pa-s^2/kg)
%In_ap - inertial term of single phase air flow region (Pa-s^2/kg)
%Rap - resistance of air side before entrance into fuel well (Pa-s/kg)
%Rtp - approximation for entire emulsion tube resistance (Pa-s/kg)
%Pupv - pressure upstream of the Venturi (Pa)
%Pfbb - calculated pressure on the bottom of the float bowl (Pa)
%Pvt - pressure at the throat of the Venturi (Pa)

%fluid properties
rhoa=1.0;             %nominal air density (kg/m^3)
mua=0.00001825;       %nominal air viscosity (Pa-s)
rhof=769;             %nominal fuel density (kg/m^3)
muf=0.000476;         %nominal fuel viscosity
sigmaf=0.02269;       %nominal surface tension (N/m)
gamma=1.4;
g=9.81;               %gravity (m/s^2)
mdot_a_min=1e-7;

switch (geometry(1))
   case(1)
      %geometry #1 consistent with Nikki Carburetor, this call
      %continues the first call to the main path

      %This configuration contains a single phase fuel section after an
      %orifice, a single phase air section with an entrance loss and an
      %orifice, and a two-phase region fed by a single hole with a
      %variable area orifice.  The two-phase region empties to the venturi throat
      %pressure through a single hole.

      Dvt=geometry(2);          %venturi throat diameter    (m)
      Dvin=geometry(3);         %venturi inlet diameter (m)
      Dvth=geometry(4);         %venturi throttle bore diameter (m)
      Cdv=geometry(5);          %discharge coefficient for venturi (-)
      Kv=geometry(6);           %wall roughness of venturi surface (m)
      Dmj=geometry(7);          %main jet diameter (m)
      Cdmj=geometry(8);         %discharge coefficient for main jet (-)
      Dsp=geometry(9);          %diameter of single phase fuel section (m)
      Lsp=geometry(10);         %length of single phase fuel section (m)
      Ksp=geometry(11);         %roughness of single phase fuel region and emulsion tube
      Let1=geometry(12);        %length from 1st air bleed hole to 2nd in emulsion tube (m)
      Let2=geometry(13);        %length from 2nd air bleed hole to 3rd in emulsion tube (m)
      Let3=geometry(14);        %length from 3rd air bleed hole to emulsion tube discharge nozzle (m)
```

```
Det=geometry(15);          %diameter of emulsion tube (m)
Det1=geometry(16);         %diameter of first set of emulsion tube holes (m)
Det2=geometry(17);         %diameter of second set of emulsion tube holes (m)
Det3=geometry(18);         %diameter of third set of emulsion tube holes (m)
Cdet=geometry(19);         %discharge coefficient of emulsion tube holes (-)
nem=geometry(20);          %number of holes per level (-)
Dap=geometry(21);          %diameter of main air path (m)
kap=geometry(22);          %minor loss factor of or main air path (-)
Kap=geometry(23);          %wall roughness in single phase air section (m)
Lap=geometry(24);          %length of main air bleed path tp fuel well (m)
Daj=geometry(25);          %diameter of sir bleed orifice (m)
Cdaj=geometry(26);         %discharge coefficient of air bleed orifice (-)
hbowl=geometry(27);        %height of fuel level in fuel bowl (m)

%venturi throat pressure calculation
avt=pi*geometry(2)^2/4;
[rhoa]=density_calc(Po,To);
Pvt_guess=Po-((mdot_engine^2)/(2*rhoa*((Cdv*avt)^2)));  %guess pressure for venturi throat,
assumes zero compressibility

[Pvt,fval,exitflag,output]=fzero(@(Pvt)Comp_Press(Pvt,Po,mdot_engine,Cdv,avt,rhoa,gamma),Pvt_guess);
crit_p_ratio=((2/(gamma+1))^(gamma/(gamma-1)));

if ((Pvt/Po)<=crit_p_ratio)
   Pvt=crit_p_ratio*Po;  %area ratio at throat is never small enough to go sonic (choke)
end

%air section resistance including emulsion tube hole flow pressure loss
aaj=pi*Daj^2/4;   %area of air inlet orifice
vaj=mdot_ap/(rhoa*aaj);    %velocity of air in orifice region
DPaj=(rhoa*vaj^2/2)*(1/(Cdaj^2)); %pressure drop in air section due to resistance and orifice losses

aap=pi*Dap^2/4; %area of air section (m^2)
vap=mdot_ap/(rhoa*aap); %velocity in air section
Reap=vap*Dap*rhoa/mua;  %Reynolds number in air section
[fap]=Reynolds_Fric(Reap,Kap,Dap);  %Re# function to determine f
kmap=0.5;   %loss coefficient associated with expansion losses in air path
DPap=(1+fap*(Lap/Dap)+kap)*rhoa*vap^2/2+kmap*rhoa*vaj^2/2-rhoa*vaj^2/2;    %Pressure drop
along main air bleed path

aet1=nem*pi*Det1^2/4;    %flow area of first level of emulsion tube holes
aet2=nem*pi*Det2^2/4;    %flow area of second level of emulsion tube holes
aet3=nem*pi*Det3^2/4;    %flow area of third level of emulsion tube holes
vet1=mdot_ap/(rhoa*aet1);   %air velocity through one set of emulsion tube holes
vet2=mdot_ap/(rhoa*(aet1+aet2));    %air velocity through two sets of emulsion tube holes
vet3=mdot_ap/(rhoa*(aet1+aet2+aet3));   %air velocity through three sets of emulsion tube holes
DPet1=1*nem*rhoa*vet1^2/2*(1/(Cdet^2))+nem*(4*sigmaf/Det1);    %pressure loss due to two-
phase entry for 1 set of holes

DPet2=2*nem*rhoa*vet2^2/2*(1/(Cdet^2))+nem*(4*sigmaf/Det1)+nem*(4*sigmaf/Det2);   %pressure
loss due to two-phase entry for 2 sets of holes

DPet3=3*nem*rhoa*vet3^2/2*(1/(Cdet^2))+nem*(4*sigmaf/Det1)+nem*(4*sigmaf/Det2)+nem*(4*sigmaf
/Det3);   %pressure loss due to two-phase entry for 3 sets of holes
```

```
%calculation of required pressure differential required to drive air bleed flows
      DPvt=abs(Po-Pvt); %driving pressure difference between upstream air bleed and venturi throat
      L_tube=Let1+Let2+Let3+Lsp;  %total length of emulsion tube
      DP_fuel_flow_min=rhof*g*(L_tube-hbowl); %minimum pressure differential to start fuel flow
      DP_fuel_air1=rhof*g*(L_tube-hbowl+Let3);    %start of air flow
      DP_fuel_air12=rhof*g*(L_tube-hbowl+Let3+Let2);   %second set of emulsion tube holes uncovered
      DP_fuel_air123=rhof*g*(L_tube-hbowl+Let3+Let2+Let1); %third set of emulsion tube holes
uncovered

      %conditional if-else loop to determine airflow pressure loss due to simulated action of fuel well
      if (DPvt>DP_fuel_air1)&(DPvt<DP_fuel_air12)
         Rap=(DPap+DPaj+DPet1)/mdot_ap;    %air bleed resistance, one set of uncovered air bleed holes
         Ltp_DP=Let3;    %length of emulsion tube under two-phase flow conditions
         Ltp_sp_DP=Let2+Let1;    %length of emulsion tube under single phase conditions
      else
         if (DPvt>DP_fuel_air12)&(DPvt<DP_fuel_air123)
            Rap=(DPap+DPaj+DPet2)/mdot_ap;    %air bleed resistance, two sets of uncovered bleed holes
            Ltp_DP=Let3+Let2;   %length of emulsion tube under two-phase flow conditions
            Ltp_sp_DP=Let1;     %length of emulsion tube under single phase conditions
         else
            if (DPvt>DP_fuel_air123)
               Rap=(DPap+DPaj+DPet3)/mdot_ap;    %air bleed resistance, three sets of air bleed holes
               Ltp_DP=Let3+Let2+Let1;  %length of emulsion tube under two-phase flow conditions
               Ltp_sp_DP=0;   %length of emulsion tube under single phase conditions
            else
               Rap=(DPaj)/mdot_a_min;  %if pressure difference is less than required to drive flow, decrease
orifice area to initial condition with min. air flow
               Ltp_DP=0;;    %length of emulsion tube used when two-phase flow is not occurring
               Ltp_sp_DP=Let3+Let2+Let1;   %length of emulsion tube under single phase conditions
            end
         end
      end

      %fuel section resistance through main jet
      LD_ratio=1; %Nikki main jet L/D ratio, (Keihin L/D=10)
      Lmj=Dmj*LD_ratio;   %calculation of orifice length
      amj=pi*Dmj^2/4;  %area of main jet (m^2)
      vmj=mdot_fm/(rhof*amj);  %velocity of fuel in main jet (m/s) based on main jet mass flow rate
      Remj=vmj*Dmj*rhof/muf;    %Reynolds # of fuel flow in main jet
      DPmj=(rhof*vmj^2/2)*(1/(Cdmj^2));   %pressure loss through main jet
      Rmj=DPmj/mdot_fm;   %resistance of main jet

      %fuel section resistance through single phase fuel section
      asp=pi*Dsp^2/4; %area of single phase fuel path (m^2)
      vsp=mdot_fm/(rhof*asp); %fuel velocity in single phase fuel section
      Resp=vsp*Dsp*rhof/muf;  %Reynolds # of fuel flow in single phase section
      [fsp]=Reynolds_Fric(Resp,Ksp,Dsp);  %friction factor call
      kmj=1.0;   %loss factor accunting for drastic cross-sectional area change
      DPsp=(1+fsp*(Lsp/Dsp))*rhof*vsp^2/2+rhof*g*Lsp-kmj*rhof*vmj^2/2; %pressure loss in single
phase fuel section
      Rsp=DPsp/mdot_fm;   %resistance of single phase fuel section

      %inertia of fuel section
      In_fm=(Lsp/asp);       %inertia of single phase fuel inertia (Pa-s^2/kg)
```

```
        %inertia of air section
        In_ap=Lap/aap;    %inertia of air (Pa-s^2/kg)

        %two-phase resistance(s) in emulsion tube
        aet=pi*Det^2/4;
        alpha=(mdot_ap/rhoa)/(((mdot_fm/rhof)+(mdot_ap/rhoa))); %void fraction at emulsion tube holes
        rhotp=alpha*rhoa+(1-alpha)*rhof;  %mean density within 2-phase region at first set of holes
        mutp=alpha*mua+(1-alpha)*muf; %mean viscosity within 2-phase region at first set of holes
        vtp=abs(mdot_tp)/(rhotp*aet);    %velocity of two-phase mixture at first set
        Retp=vtp*Det*rhotp/mutp;    %Reynolds # of two-phase mixture
        [ftp]=Reynolds_Fric(Retp,Ksp,Det);
        %calculate homogeneous pressure loss or use Arias correlation
        %(conditional statement used to prevent solution divergence)
        DPtp_homo=(rhotp*vtp^2)/2*(1+ftp*(Ltp_DP/Det))+rhotp*g*(Let1+Let2+Let3);
        DPtp_sp=(rhof*vsp^2)/2*(1+fsp*(Ltp_sp_DP/Det))+rhof*g*(Ltp_sp_DP)-rhof*g*Lsp;    %pressure
loss due to friction and gravity head in 2-phase section
        if (DPtp_sp<0)
           DPtp_sp=0;
        end
        DPtp_corr=(5.665E+03+ 3.702E+06*mdot_fm - 1.514E+09*mdot_fm^2 - 1.336E+09*mdot_ap +
8.307E+13*(mdot_ap^2))*(Ltp_DP);
        if (DPtp_corr<=0.01*DPtp_homo)        %use homogeneous pressure drop to steer solution if
necessary
           DPtp_corr=0.01*DPtp_homo;
        end
        if (DPtp_corr>=10*DPtp_homo)
           DPtp_corr=10*DPtp_homo;
        end
        Rtp=(DPtp_corr+DPtp_sp)/mdot_tp;    %resistance of two-phase section using a correction for
different densities and bleed rates
        %two-phase resistance calculation using homogeneous model (for comparisons only)
        %Rtp=DPtp_homo/mdot_tp;  %resistance of two-phase section using an approximation that assumes a
homogeneous density throughout the entire tube length

    otherwise
        'Error- geometric configuration not recognized'
end
```

C.3 MATLAB Code: Stder_main.m

```
function[dmdot_fmdt,dmdot_apdt,mdot_tp,Paj,Pmj,Psp,Pet]=stder1_main(Po,Pupv,Pfbb,Pvt,mdot_fm,mdo
t_ap,Rmj,In_fm,Rsp,In_ap,Rap,Rtp)
%The inputs to the function are:
%Po - upstream stagnation pressure
%Pupv - static pressure upstream of the Venturi (Pa)
%Pfbb - pressure at the bottom of the float bowl at the entrance of the main jet (Pa)
%Pvt - Venturi throat pressure (Pa)
%mdot_fm - fuel mass flow rate minus fuel flow diverted to main well(kg/s)
%Rmj - resistance of the main jet fuel section (Pa-s/kg)
%Rsp - resistance of the single phase fuel section after the main jet  (Pa-s/kg)
%Rap - resistance of the air bleed section (Pa-s/kg)
%Rtp - resistance of two phase section (Pa-s/kg)
%In_fm - inertial element of single phase fuel section (Pa-s^2/kg)
%In_ap - inertial element of single phase air section (Pa-s^2/kg)
```

```
%The outputs from the function are:
%dmdot_fm/dt - the rate of change of fuel flow rate (kg/s^2)
%dmdot_ap/dt - the rate of change of air flow rate (kg/s^2)
%mdot_tp - two-phase flow rate (kg/s)
%Pet - pressure at the expandable orifice (Pa)
%Psp - pressure at the imaginary junction between the single phase resistor and the single phase inertial
element (Pa)
%Pmj - pressure after the main jet (input for the idle path) (Pa)
%Paj - pressure after the main air bleed orifice (Pa)

rhof=769;
g=9.81;

%Setup the constitutive and constraint equations in matrix form A*X=b
%where X=[dmdot_fmdt,dmdot_apdt,mdot_tp,Paj,Pet,Psp,Pmj]
%Eq. 1: constitutive equation for main jet resistance(Pfbb-Pmj)=mdot_fm*Rmj)
A(1,1)=-1;
b(1,1)=mdot_fm*Rmj-Pfbb;
%Eq. 2: constitutive equation for single phase fuel inertia (Pmj-Psp)*(1/In_fm)=dmdot_fm\dt
A(2,1)=1;
A(2,2)=-1;
A(2,7)=-In_fm;
%Eq. 3: constitutive equation for single phase fuel resistance (Psp-Pet)=mdot_fm*Rsp
A(3,2)=1;
A(3,3)=-1;
b(3,1)=mdot_fm*Rsp;
%Eq. 4: constitutive equation for single phase air inertia (Po-Paj)*(1/In_ap)=dmdot_ap\dt
A(4,4)=-1;
A(4,6)=-In_ap;
b(4,1)=-Po;
%Eq. 5: constitutive equation single phase air resistance (Paj-Pet)=mdot_ap*Rap
A(5,3)=-1;
A(5,4)=1;
b(5,1)=mdot_ap*Rap;
%Eq. 6: constitutive equation for 2-phase resistance (Pet-Pvt)=mdot_tp*Rtp
A(6,3)=1;
A(6,5)=-Rtp;
b(6,1)=Pvt;
%Eq. 7: constraint equation to balance mass (mdot_fm+mdot_ap=mdot_tp)
A(7,5)=1;
b(7,1)=mdot_fm+mdot_ap;

%LU decomposition
Nv=length(b); %length of b matrix
[L,U]=lu(A);    %broken up into upper and lower triangular elements
Y=inv(L)*b; %inverting the lower triangle
X(Nv)=Y(Nv)/U(Nv,Nv);   %solving for the first output

%back substitution
for i=(Nv-1):-1:1
   X(i)=(Y(i)-sum(X(i+1:Nv).*U((i),i+1:Nv)))/U(i,i);   %multiply and sum each result by the previous
end

dmdot_fmdt=X(7);   %change in fuel flow over time
```

```
dmdot_apdt=X(6);   %total air flow
mdot_tp=X(5);      %2-phase flow
Paj=X(4);          %pressure after air bleed
Pet=X(3);          %pressure at expandable orifice
Psp=X(2);          %pressure after main jet
Pmj=X(1);          %pressure after main air bleed

mdot_a_min=1e-7;   %minimum flow rate to prevent singularities
mdot_f_min=1e-6;   %minimum flow rate to prevent singularities


if (mdot_ap<mdot_a_min)
   mdot_ap=mdot_a_min;
end

if (mdot_tp<mdot_f_min)
   mdot_tp=mdot_f_min;
end

BS_Intek_Engine_main;   %call geometry vector
Lsp=geometry(10);
Let1=geometry(12);
Let2=geometry(13);
Let3=geometry(14);
hbowl=geometry(27);

DPvt=abs(Po-Pvt);
DP_flow_min=rhof*g*(Let3+Let2+Let1+Lsp-hbowl);  %min dp to initialize flow

if (DPvt<DP_flow_min)   %if driving potential is less than dp min, set flow to min
   mdot_fm=mdot_f_min;
end
```

C.4 **MATLAB Code:** Mainpath.m

```
function[mdot_fm,mdot_ap,mdot_tp,Paj,Pmj,Psp,Pet]=mainpath1(geometry,mdot_fmold,mdot_apold,mdot
_tpold,Pajold,Pmjold,Pspold,Petold,CA,Pupv,Pfbb,Po,To,mdot_engine,Pvt,dt)

%This function computes the fuel flow rate through the timestep

%call GtoR1main for to calculate resistances, venturi throat pressure, and inertial terms using flow
%rates and old values from last time step
[Rmj,In_fm,Rsp,In_ap,Rap,Rtp,Pvt]=GtoR1main(geometry,mdot_fmold,mdot_apold,mdot_tpold,Pmjold,P
spold,Petold,Pajold,CA,Pupv,Pfbb,Po,To,mdot_engine,Pvt);
N=5;
dtl=dt/N;

for i=1:N  %integrate change in flow rates over time using RK4 procedure

[dmdot_fmdt1,dmdot_apdt1,mdot_tp,Paj,Pmj,Psp,Pet]=stder1_main(Po,Pupv,Pfbb,Pvt,mdot_fmold,mdot_
apold,Rmj,In_fm,Rsp,In_ap,Rap,Rtp);
```

```
[dmdot_fmdt2,dmdot_apdt2,mdot_tp,Paj,Pmj,Psp,Pet]=stder1_main(Po,Pupv,Pfbb,Pvt,mdot_fmold+dmdot
_fmdt1*dtl/2,mdot_apold+dmdot_apdt1*dtl/2,Rmj,In_fm,Rsp,In_ap,Rap,Rtp);

[dmdot_fmdt3,dmdot_apdt3,mdot_tp,Paj,Pmj,Psp,Pet]=stder1_main(Po,Pupv,Pfbb,Pvt,mdot_fmold+dmdot
_fmdt2*dtl/2,mdot_apold+dmdot_apdt2*dtl/2,Rmj,In_fm,Rsp,In_ap,Rap,Rtp);

[dmdot_fmdt4,dmdot_apdt4,mdot_tp,Paj,Pmj,Psp,Pet]=stder1_main(Po,Pupv,Pfbb,Pvt,mdot_fmold+dmdot
_fmdt3*dtl,mdot_apold+dmdot_apdt3*dtl,Rmj,In_fm,Rsp,In_ap,Rap,Rtp);

   mdot_fmold=mdot_fmold+dtl*(dmdot_fmdt1+2*dmdot_fmdt2+2*dmdot_fmdt3+dmdot_fmdt4)/6;
   mdot_apold=mdot_apold+dtl*(dmdot_apdt1+2*dmdot_apdt2+2*dmdot_apdt3+dmdot_apdt4)/6;

end
mdot_fm=mdot_fmold;
mdot_ap=mdot_apold;
```

C.5 MATLAB Code: Runmainpath.m

```
[N,g]=size(dt); %creates a group of steps equally sized in number to the number of timesteps produced by
GT Power
clear mdot_fm;
clear mdot_ap;
clear mdot_tp;

%intial guess values for unknown variables
mdot_fm(1,1)=0.0001;
mdot_ap(1,1)=0.00001;
mdot_tp(1,1)=mdot_ap(1,1)+mdot_fm(1,1);
Psp(1,1)=100000;
Paj(1,1)=99500;
Pmj(1,1)=99000;
Pet(1,1)=98500;
time(1,1)=0.00;

BS_Intek_Engine_main;

%obtain pressure at bottom of float bowl
hbowl=geometry(27); %calls height of float bowl
rhof=769;   %fuel density
rhoa=1;
g=9.81; %gravity
Pfbb(1,1)=Pupv(1,1)+rhof*g*hbowl; %calculates pressure at bottom of float bowl

done=0;
tol=1e-10;  %allowable error
while(done==0)
   for i=1:(N-1)

[mdot_fm(i+1,1),mdot_ap(i+1,1),mdot_tp(i+1,1),Paj(i+1,1),Pmj(i+1,1),Psp(i+1,1),Pet(i+1,1)]=mainpath1(
geometry,mdot_fm(i,1),mdot_ap(i,1),mdot_tp(i,1),Paj(i,1),Pmj(i,1),Psp(i,1),Pet(i,1),CA(i,1),Pupv(i),Pfbb(i)
,Po(i),To(i),mdot_engine(i),Pvt(i),dt(i));
      time(i+1)=time(i)+dt(i);
      Pfbb(i+1)=Pupv(i)+rhof*g*hbowl;    %calculation of pressure at bottom of float bowl at entrance to
network
   end
```

```
   err=((abs(mdot_fm(N)-mdot_fm(1)))+(abs(mdot_ap(N)-mdot_ap(1))))/2

   if (err<tol)
      done=1;
   else
      mdot_fm(1)=mdot_fm(N);
      mdot_ap(1)=mdot_ap(N);
      mdot_tp(1)=mdot_tp(N);
      Pmj(1)=Pmj(N);
      Psp(1)=Psp(N);
      Paj(1)=Paj(N);
      Pet(1)=Pet(N);
   end
end

%integration for AFR
m_a=trapz(time,mdot_engine)
m_fm=trapz(time,mdot_fm)
```

C.6→C.9 Accessory Functions

C.6 MATLAB Code: Reynolds_Fric.m

```
function[ff]=Reynolds_Fric(Re,K,D)
%This is a generic function that calculates the friction factor based off of Re#
if (Re<10)
   ff=0.064;   %constant f if Reynolds # falls towards zero and fuel well is full of fuel
else
   if (Re<3000)
      ff=64/Re; %assume laminar flow
   else
      ff=1/((-1.8*log10((6.9/Re)+((K/D)/3.7)^1.11))^2); %turbulent flow in a rough tube
   end
end
```

C.7 MATLAB Code: Throttle_Area.m

```
function[athr]=throttle_area(theta,theta_o,Dthr,Dsh)
a=Dsh/Dthr;  %intermediate variable
radian=theta*pi/180;  %convert throttle angle from degrees to radians
radian_o=theta_o*pi/180;  %convert non-zero throttle stop angle from degrees to radians

athr=(pi*Dthr^2/4)*((1-(cos(radian)/cos(radian_o)))+(2/pi)*((a/cos(radian))*((cos(radian)^2)-
(a^2*cos(radian_o)^2))^(1/2)-((cos(radian)/cos(radian_o))*asin(a*cos(radian_o)/cos(radian)))-a*(1-
a^2)^(1/2)+asin(a)));

theta_crit=2*acos(a);   %calculates segment angle
a_segment=0.5*((Dthr/2)^2)*(theta_crit-sin(theta_crit));   %1/2 area of throttle bore minus half the area of
the projected throttle shaft area
a_max=2*a_segment;  %twice the segment area calculates effective throttle flow area

radian_max=acos(a);
```

```
theta_max=radian_max*180/pi;

if (theta>=theta_max)
   athr=a_max;
end

%minimum throttle area
a_min=(pi*Dthr^2/4)*((1-(cos(radian_o)/cos(radian_o)))+(2/pi)*((a/cos(radian_o))*((cos(radian_o)^2)-
(a^2*cos(radian_o)^2))^(1/2)-((cos(radian_o)/cos(radian_o))*asin(a*cos(radian_o)/cos(radian_o)))-a*(1-
a^2)^(1/2)+asin(a)));

if (athr<=a_min)
   athr=a_min;
end
```

C.8 MATLAB Code: Comp_Press.m

```
function [y] = Comp_Press(P,Po,mdot_engine,Cd,area,rhoa,gamma)

%standard equation for compressible mass flow through a restriction/contraction, includes a term for
compressibility

y=(Cd*area)^2*(2*rhoa*(Po-P))*((gamma/(gamma-1))*((P/Po)^(2/gamma)-
(P/Po)^((gamma+1)/gamma))/(1-(P/Po)))-mdot_engine^2;
```

C.9 MATLAB Code: Discharge_Coeff.m

```
function [cd_fit]=discharge_coeff(theta)
theta_test=[0,3.5,5,7.5,10,15,22.5,30,37.5,45,52.5,60,67.5,75,82.5,85];
cd_test=[0.6,0.62,0.63,0.7,0.76,0.825,0.86,0.885,0.9,0.915,0.925,0.935,0.9375,0.94,0.94,0.94];
cd_fit=interp1(theta_test,cd_test,theta);
```

[1]. US-EPA. Final Phase 2 Standards for Small Spark-Ignition Handheld Engines. Regulatory Announcement EPA420-F-00-007, United States Environmental Protection Agency, March 2000.

[2]. Arias, D.A. Numerical and Experimental Study of Air and Fuel Flow in Small Engine Carburetors. PhD. thesis. University of Wisconsin- Madison, 2005.

[3]. US-EPA. Average Annual Emissions, all criteria pollutants. http://www.epa.gov/ttn/chief/trends. Last accessed 4 April, 2007.

[4]. US-EPA. Phase 2: Emission Standards for New Non-road Spark-Ignition Engines at or Below 19 Kilowatts. Regulatory Support Document: Technologies and Standards, ANR-443, United States Environmental Protection Agency, December 1997.

[5]. Heywood, J.B. *Internal Combustion Engine Fundamentals*. McGraw-Hill Book Company, New York, 1988.

[6] Arias, D.A. Shedd, T.A. CFD Analysis of Flow Field and Pressure Losses in Carburetor Venturi. *SAE Technical Report*, (2006-32-0113), 2006.

[7] White, F.M. *Viscous Fluid Flow. 2nd Edition*, McGraw-Hill Book Company, New York, 1991.

[8] Alsemgeest, R. Shaw, C.T. Richardson, S.H. and Pierson, S. Modeling the time-dependent flow through a throttle valve. *SAE Technical Report,* (2000-01-0659), 2000.

[9] Woods, W.A. and Goh, G.K. Compressible Flow Through a Butterfly Valve in a Pipe. *Proc. Institution of Mechanical Engineers*, 193:237-244, 1979.

[10] Pursifull, R. Kotwicki A.J. and Hong, S. Throttle flow characterization. *SAE Technical Report,* (2000-01-0571), 2000.

[11] Harrington, D.L. and Bolt, J.A. Analysis and digital simulation of carburetor metering. *SAE Technical Report,* (700082), 1970.

[12] Takizawa, M. Uno. T. Oue, T. and Yura, T. A Study of Gas Exchange Process Simulation of an Automotive Multi-Cylinder Internal Combustion Engine. *SAE Technical Report*, (820410), 1982.

[13] Ohata, A. and Ishida, Y. Dynamic Inlet Pressure and Volumetric Efficiency of Four Cycle Four Cylinder Engine. *SAE Technical Report,* (820407), 1982.

[14] Chapman, M. Novak, J.M. and Stein, R.A. Numerical Modeling of Inlet and Exhaust Flows in Multi-Cylinder Internal Combustion Engines. In *Flows in Internal Combustion Engines,* Winter Annual Meeting, ASME, New York, 1982.

[15] *SuperFlow Flowbench 600 Instructions.*

[16] Bicen, A.F. and Whitelaw, J.H. Steady and Unsteady Air Flow through an Intake Valve of a Reciprocating Engine. In *Flows in Internal Combustion Engines-II*, FED-vol. 20, Winter Annual Meeting, ASME, 1984.

[17] Heisler, H. *Advanced Engine Technology*. SAE International, 1995.

[18] Horlock, J.H. and Winterbone, D.E. The Thermodynamics and Gas Dynamics of Ineternal Combustion Engines: Volume II. Oxford University Press, New York, 1982.

[19] Chung, N. Kim, S. and Sunwoo, M. Nonlinear Dynamic Model of a Turbocharged Diesel Engine. *SAE Technical Report*, (2005-01-0017), 2005.

[20] Stone, R. *Introduction to Internal Combustion Engine, 3rd Edition*. Society of Automotive Engineers, Inc. Warrendale, PA, 1999.

[21] Nowakowski, J. and Sobieszczanski, M. Inlet System Choice of Spark Ignition Engine Based on Numerical Analysis of Filling a Cylinder. *SAE Technical Report*, (1999-01-0217), 1999.

[22] Benson, R.S. and Whitehouse, N.D. *Internal Combustion Engines, vol. 2*. Pergamon Press, 1979.

[23] Winterbone, D.E. and Pearson R.J. *Design Techniques for Engine Manifolds*. SAE International, 1999.

[24] Zhu, Y. and Reitz, R.D. A 1-d gas dynamics code for subsonic and supersonic flows applied to predict EGR levels in a heavy-duty diesel engine. *International Journal of Vehicle Design,* 22(3):227-252, 1999.

[25] AVL, *Boost.* http://www.avl.com. Last accessed 3 May, 2007.

[26] Ricardo Software. *Wave*. http://www.ricardo.com/wave. Last accessed 3 May, 2007.

[27] Gamma Technologies. *GT-Power: User's manual and tutorial, Version 5.2*. Gamma Technologies, 2001.

[28] Shinoda, K. Koide, H. and Yii, A. Analysis and Experiments on Carburetor Metering at the Transition Region to the Main System. *SAE Technical Report*, (710206), 1971.

[29] Furuyama, M. Fuel Supply Characterisitics in the Transition Region of Fixed-Venturi Type Carburetors. *Bulletin of JSME*, 21(191):8442-848, 1981.

[30] Furuyama, M. Fuel Supply Characteristics of Idle-System of Carburetor under Steady-State Conditions, *Bulletin of JSME*, 21(154):722-729, 1978.

[31] Sendyka, B. and Heydel, W. The Analysis of a Constant Depression Carburettor with a Fuel Feeder. *SAE Technical Report*, (940212), 1994.

[32] Hosho, Y. Flow Quantities of Air Introduced Through Air Bleeds into Carburetors and Pulsating Fuel Jet Phenomena. *Hitachi Review,* vol. 16, no. 4, 1967.

[33] Moss, P.J. Pulsation Enrichment in Carburetters. *Automotive Engineer,* August/September, 53-56, 1980.

[34] Tanaka, M. and Durbin, J. Transient Response of a Carburetor Engine. *SAE Technical Report*, (770046), 1977.

[35] Furuyama, M. and Ohgane, H. A Comparison of Pulsating and Steady Flows in Terms of Carburetor Characteristics. *JSAE Review*, 8(3):18-23, 1987.

[36] Derezinski, S.J. Digital Computer Simulation of Oscillatory Flow in Carburetor Fuel Metering Channels. PhD thesis, University of Michigan, 1972.

[37] Hubbard, M. Dynamic computer simulation of an engine intake and carburetion system. In *Winter Computer Simulation Conference*, pages 477-480, 1980.

[38] Szczecinski, J. and Rychter, T.J. Theoretical Analysis of Mixture Stoichiometry in Engine Carburetor. *SAE Technical Report*, (910078), 1978.

[39] Sendyka, B. and Filipczyk, J. Simulation of the Characteristic of a Carburettor of an Internal Combustion Engine. *SAE Technical Report*, (950987), 1995.

[40] Tanaka, M. Sato, T. and Watanabe, K. Pulsation Effects in the Air Fuel Ratio of Carburetor Engines. *SAE Technical Report*, (861241), 1986.

[41] Arias, D.A. and Shedd, T.A. Numerical and Experimental Study of Fuel and Air Flow in Carburetors for Small Engines, *SAE Technical Report*, (2004-32-0053), 2004.

[42] Klein, S.A. Engineering Equation Solver (EES. http://www.fchart.com. F-Chart Software © 1992-2004.

[43] Arias, D.A. and Shedd, T.A. Implementation of a Theoretical Carburetor Model in One-Dimensional Engine Simulation Software. *SAE Technical Report*, (2006-01-1543), 2006.

[44] Oya, T. Upward Liquid Flow in Small Tube into which Air Streams (1st Report, Experimental Apparatus and Flow Patterns). *Bulletin of JSME*, 14(78):1320-1329, 1971.

[45] Oya, T. Upward Liquid Flow in Small Tube into which Air Streams (2nd Report, Pressure Drop at the Confluence). *Bulletin of JSME*, 14(78):1330-1339, 1971.

[46] Chisholm, D. Flow of Incompressible Two-Phase Mixtures Through Sharp-Edged Orifices. *The Journal of Mechanical Engineering Science*, vol. 9, no.1, 72-80, 1967.

[47] Chisholm, D. Flow of Compressible Two-Phase Mixtures Through Sharp-Edged Orifices. *The Journal of Mechanical Engineering Science*, vol. 23, no. 1, 45-48, 1981.

[48] Lockhart, R.W. and Martinelli, R.C. Proposed Correlation of Data for Isothermal Two-Phase Two-Component Flow in Pipes. *Chemical Engineering Progress*, 45:39-45, 1949.

[49] Lenz, H. P. *Mixture Formation in Spark-Ignition Engines*. SAE International, 1990.

[50] Ehara, M. Kinabara, Y. Shinoda, K. and Ishihara, T. A Study of Carburetor Design. *SAE Technical Report*, (805142), 1980.

[51] Jehlik, F.A. and Ghandhi, J.B. Investigation of Intake Port Fuel Films in a Small Utility Air-Cooled Engine. *SAE Technical Report*, (2001-01-1788), 2001.

[52] Chen, C. Johns, R. and Zeng, Y. Detailed Modeling of Liquid Fuel Sprays in One-Dimensional Gas Flow Simulation. *SAE Technical Report*, (2004-01-3000), 2004.

[53] Cengel, Y. and Cimbala, J. *Fluid Mechanics: Fundamentals and Applications*, McGraw-Hill, New York, 2006.

[54] Shah, R.K. and London, A.L. Laminar Flow Forced Convection in Ducts, Academic Press, 1978.

[55] Rohsenow, W. Hartnett, J. and Cho, Y. *Handbook of Heat Transfer*, *3rd Edition*, McGraw-Hill, New York, 1998.

[56] Press, W.H., S.A. Teukolsky, W.T. Vetterling, and B.P. Flannery, *Numerical Recipes in C: The Art of Scientific Computing, 2nd Edition*, Cambridge University Press, Oakleigh, Victoria, Australia (1992).

[57] Mathworks. *Matlab.* http://www.mathworks.com. Last accessed 4 Mat, 2007.

[58] Asano, Y. Chuma, T. and Haga, H. Effects of Air-Bleed Systems on Carburettor Performance. *Bulletin of JSME*, 11(46):691-698, 1968.

[59] Collier, J.G. and Thome J.R. *Convective Boiling and Condensation*. Claredon Press, Oxford, 1996.

[60] Fox, R.F. and McDonald, A.T. *Introduction to Fluid Mechanics, 5th Edition*, Wiley, 2000.

[61] Ould Didi, M.B. Kattan, N. and Thome, J.R. Prediction of Two-Phase Pressure Gradients of Refrigerants in Horizontal Tubes. *International Journal of Refrigeration*, 25(2002) 935-947.

Approved: _____ (Professor T.A. Shedd) 05/14/2007